Development of n-type and p-type Mg2Si1-xSnx alloys for thermoelectrical applications in the temperature range 300-600 °C

Radivoje Vracar

UNIVERSITE DE GRENOBLE

THÈSE

Pour obtenir le grade de

DOCTEUR DE L'UNIVERSITÉ DE GRENOBLE

Spécialité : Matériaux, Mécanique, Génie Civil, Electrochimie Arrêté ministériel : 7 août 2006

Présentée par

Radivoje VRACAR

Thèse dirigée par **Guillaume Bernard-Granger**

préparée au sein du **Laboratoire de Thermoélectricité du CEA-Grenoble**

dans **l'École Doctorale Ingénierie-Matériaux Mécanique Energétique Environnement Procédés Production (I-MEP2)**

Développement de matériaux Mg2Si1-xSnx de type n et p pour applications thermoélectriques dans la gamme de température 300-600 °C

Thèse soutenue publiquement le 22 Octobre, 2014, devant le jury composé de :

M, **Jérôme CHEVALIER**

Professeur, INSA Lyon, Rapporteur

M, **Stéphane GORSSE**

Maître de Conférences, Université de Bordeaux, Rapporteur

M, **Jean-Marc CHAIX**

Directeur de Recherches CNRS, Grenoble INP, Examinateur

M, **Bertrand LENOIR** Professeur, Ecole des Mines de Nancy, Président

M, **Guillaume BERNARD-GRANGER**

Directeur de Recherche CEA, Directeur de Thèse

Acknowledgment

All my thanks go to my girlfriend Tamara, my parents Radmila and Aleksandar, and friends for their support. They sustained me throughout my thesis and enabled me to pursue and finish this dissertation.

I am indebted to my supervisor, Dr. Guillaume Bernard-Granger, on his guidance, inexhaustible patience and trust. My thanks go to Dr. Julia Simon for constant encouragement during my work on the thesis. I thank Dr. Natalio Mingo for his support and great theoretical insight on any problem I have encountered.

I would like to thank all those individuals who helped me during my thesis, like Dr. Christelle Navone who was willing to quickly solve any problem that presented itself. My special thanks go to Mathieu Soulier and Jean Leforestier on their help and for being there to provide technical expertise. Last, but not least, I would like to thank Mathieu Boidot and his willingness to provide technical support on spark plasma sintering and encouragement which helped me greatly in writing and finishing this thesis.

Chapter 1: Thermoelectricity, thermoelectric materials and objectives of the Thesis

Chapter 2: Phase diagrams and structure of Mg-Si-Sn and Mn-Si alloys – Experimental methods

I. Introduction générale

Les préoccupations d'ordre énergétique n'ont jamais autant été d'actualité. Les problèmes concernant l'environnement, tels que les émissions de gaz à effet de serre ainsi que l'envolée des prix des matières fossiles, nous amènent à nous intéresser à de nouvelles sources d'énergies renouvelables. L'énergie solaire, l'énergie éolienne, l'énergie hydroélectrique, l'énergie géothermique ou encore la thermoélectricité peuvent jouer un rôle primordial dans la sécurité énergétique et dans la limitation du réchauffement climatique. Ces énergies produisent moins d'émissions de gaz à effet de serre que les carburants fossiles et sont de plus inépuisables. La récupération d'énergie occupe ainsi une place essentielle dans la stratégie mondiale actuelle. La Commission Européenne a proposé de fixer dans son projet "énergie et changement climatique" de janvier 2007 la part des énergies renouvelables à 20 % de la consommation globale d'ici 2020 à l'échelle européenne.

La thermoélectricité, conversion directe et réciproque entre énergie électrique et énergie thermique, a déjà fait ses preuves. Les modules thermoélectriques sont déjà utilisés pour la production d'énergie électrique pour les sondes spatiales de la NASA notamment. Ces modules sont nommés RTG (Générateur Thermoélectrique à Radioisotope). Ce sont des générateurs électriques nucléaires produisant de l'électricité à partir de la chaleur résultant de la désintégration radioactive de matériaux riches en un ou plusieurs radioisotopes. La chaleur est convertie en électricité par effet Seebeck à travers des couples thermoélectriques. Ces systèmes fonctionnent depuis de nombreuses années dans l'espace, bien au-delà de leur temps de vie initialement prévu.

De nombreuses recherches dans l'industrie automobile s'orientent vers la thermoélectricité. Seuls 30 % de l'énergie libérée par la combustion du carburant servent à produire un travail mécanique, l'énergie restante est perdue sous forme de chaleur. Une partie pourrait être récupérée par un générateur thermoélectrique afin d'alimenter les consommateurs électriques et ainsi réduire la consommation de carburant.

De nos jours, la majorité des dispositifs thermoélectriques existants concernent des modules réalisés à partir de matériaux à base de Bi_2Te_3, ou PbTe, solide et de leurs dérivés. Ces matériaux sont cependant toxiques, et contiennent des éléments relativement onéreux et peu abondant (le tellure). Dans un souci d'industrialisation, ces deux points sont critiques. Il est donc nécessaire de développer des matériaux à base d'éléments abondants sur terre et biocompatibles. A basses températures (150 °C maximum), des matériaux thermoélectriques organiques sont actuellement développés pour pallier au manque de matériau inorganique non toxique et peu onéreux dans cette gamme de température. A haute température, seul l'alliage Si-Ge est performant. C'est alors un bon candidat pour le secteur automobile pour les véhicules équipés de moteurs à essence. Cependant, le germanium est un des éléments les plus onéreux,

il est donc nécessaire de limiter sa teneur dans l'alliage, tout en conservant de bonnes propriétés thermoélectriques. A moyenne température, des études sur les alliages Mg-Si/Mg-Si-Sn et Mn-Si, pour les types n et p respectivement, sont effectuées pour remplacer les modules à base de PbTe. Deux autres familles de matériaux se développent dans cette gamme de température : les skutterudites et les clathrates qui ont aussi l'inconvénient d'incorporer des éléments rares et onéreux (baryum et ytterbium en particulier).

Au cours de ce travail de Thèse, nous nous sommes donc intéressés aux siliciures des familles Mg-Si-Sn et Mn-Si pour le développement de matériaux thermoélectriques efficaces dans la plage 20-500 °C. Par rapport aux études déjà réalisées sur ce type de matériaux nous avons essayé de nous démarquer en jouant sur l'aspect simplicité/gain de temps du procédé de fabrication de compacts massifs polycristallins denses. Pour cette raison, la mécano-synthèse a été utilisée pour la fabrication des poudres mères. Même si les quantités manipulées lors de nos travaux ont été au maximum de 25g, cette méthode peut être assez facilement upgradée pour permettre la réalisation de lots de quelques kilogrammes. Dans un deuxième temps, le frittage SPS (spark plasma sintering) a été retenu pour la fabrication des matériaux denses. Cette méthode particulière de frittage se distingue des autres par des durées de cycle froid à froid de quelques minutes à quelques dizaines de minutes maximum.

Dans cette optique, le premier chapitre de ce manuscrit proposera une présentation générale de la thermoélectricité. Les effets thermoélectriques et les principes de base seront rappelés. Les matériaux thermoélectriques développés selon les domaines d'applications seront décrits ainsi que les pistes permettant leur optimisation. L'approche adoptée dans le cadre de nos travaux sera également présentée.

Après un bref rappel sur les diagrammes de phase et les structures des alliages Mg-Si-Sn et Mn-Si qui nous intéressent, le deuxième chapitre sera consacré aux techniques expérimentales. Cette partie présentera les méthodes de mécano-synthèse et de frittage SPS. Les différentes techniques de caractérisation thermoélectriques et microstructurales seront également abordées.

Le troisième chapitre expose et discute les premiers résultats obtenus sur la formulation Mg-Si-Sn de type n retenue pour notre étude. Un lien fort est fait entre l'observation de la microstructure post-frittage et les propriétés thermoélectriques mesurées.

Le quatrième chapitre s'intéressera à l'optimisation des propriétés thermoélectriques du matériau Mg-Si-Sn de type n, toujours en lien direct avec sa microstructure. Il sera montré que l'optimisation des conditions de frittage et l'éventuelle incorporation d'une faible quantité d'une seconde phase nanostructurée permet d'augmenter significativement les performances thermoélectriques du matériau dans la gamme de température 20-500 °C.

Au cours du cinquième chapitre, nous aborderons le matériau de type p. Après quelques essais sur un matériau de la famille Mg-Si-Sn, notre choix s'est finalement porté sur un matériau de la famille Mn-Si. Faute de temps, les résultats présentés et discutés dans ce manuscrit ne sont, hélas,que préliminaires.

Enfin, la dernière partie est une conclusion générale. Elle évoque également des voies possibles quant à la poursuite des travaux sur les deux types de matériaux que nous avons investigués pendant notre Thèse.

Il est à noter que le reste de la Thèse sera rédigé en anglais.

CHAPTER 1

Thermoelectricity, thermoelectric materials and objectives of the Thesis

1.1 General introduction to chapter 1

First chapter represents an introduction to thermoelectricity. Its goal is to explain the primary objective of the dissertation and necessary elements to understand physical principles of thermoelectricity.

First part explains the thermoelectric effects. Afterwards, following the definition of the figure of merit, different parameters explaining the thermoelectric efficiency of a given material will be presented.

In the second part of the chapter, thermoelectric materials will be presented and categorized according to temperature range where they have the highest efficiency. Finally, the third part will briefly explain the goal of the dissertation as well as the reasons behind the choice of the materials we have chosen to investigate.

1.1.1 Introduction to thermoelectricity

When a temperature gradient is imposed on a thermoelectrical material, an electric field is formed, and electrons flow from hot to the cold side. This is called the Seebeck effect. The Peltier effect is the opposite of the Seebeck one. It occurs when an electrical current is imposed across a thermoelectrical material resulting in the creation of a temperature gradient across the thermoelectric material. Both effects are called thermoelectric effects and they were discovered in the middle of the 19th century. Their significance and potential have been recognized much later. Physical principles that explain these effects will be briefly exposed here after.

1.2 Thermoelectricity

1.2.1 Thermoelectric effects

1.2.1.1 Seebeck Effect

The first thermoelectric effect was discovered in 1821 by Seebeck using two connected conductors. The Seebeck effect in any single isolated material implies that if a material is subjected to a temperature gradient, it will generate a voltage known as Seebeck voltage (as illustrated in Figure 1.1). Seebeck discovered this on two joined dissimilar materials, but it is a property that any individual bulk material possesses. Ratio of the Seebeck voltage to the temperature difference is called the Seebeck coefficient *S* and can be mathematically written as:

$$S = -\frac{dV}{dT} \qquad 1.1$$

The sign of the Seebeck coefficient will be positive if the main carriers travelling through the material are holes or negative if they are electrons.

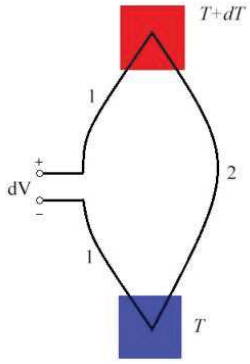

Figure 1.1: *Two connected conductors with temperature differences at junctions.*

As there are hot and cold ends of the junctions, the Seebeck voltage is generated due to the difference in carrier energy. Energy of carriers and carrier density is always higher at the hot end and above the Fermi level [1]. A diffusion of carriers occurs from hot to cold junction until a sufficiently large field is generated to prevent further diffusion. In Figure 1.2, energy of carriers and the density of states at the hot and cold end of the thermoelectrical material are presented.

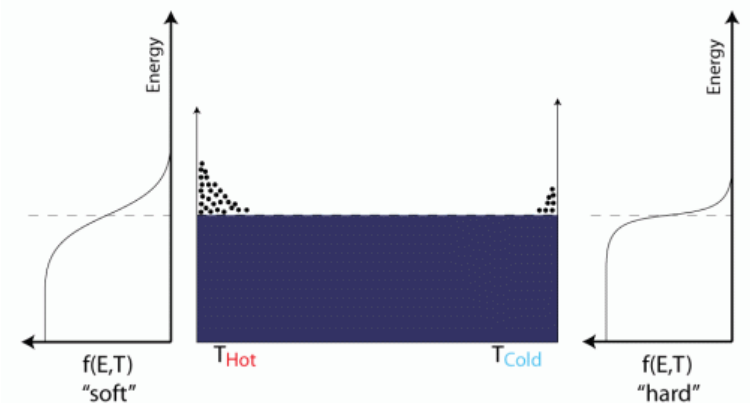

Figure 1.2: *Density of states showing carriers at hot and cold junctions*

The other name for the Seebeck coefficient is thermo power, because it is a basic principle of power generators, and it represents the maximum electrical energy that can be obtained from a temperature difference. Thermo power is an important parameter, and a lot of researchers aimed to improve it [2]. For a real thermoelectric device, there are other parameters that need to be optimized for the sake of better performances.

1.2.1.2 Peltier Effect

Reverse from the Seebeck effect is called the Peltier effect, which was discovered by Jean Charles Athanase Peltier in 1834. If an electric current flows through a junction consisting of two dissimilar materials, junction A (in comparison to B) is either heated or cooled depending on the direction of the current. On Figure 1.3, a simple sketch of Peltier effect is given.

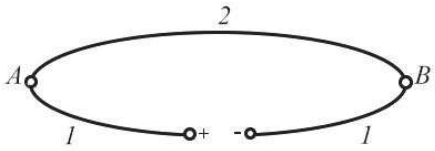

Figure 1.3: *Presentation of a circuit, current flowing through junctions A and B through materials 1 and 2.*

The rate of heat exchange at the junctions per unit time, $\dot{Q}$, due to passage of current I is described as:

$$\dot{Q} = \frac{dQ}{dT} = (\Pi_{12}(T))I = (\Pi_1(T) - \Pi_2(T))I \qquad 1.2$$

where Π_1 and Π_2 are Peltier coefficients generated in materials 1 and 2 respectively, Π_{12} is the Peltier coefficient generated at the junction A (figure 1.3). Peltier coefficient is explained as the amount of heat that is carried per unit charge in a given material. With the continuous charge current across a junction, the associated heat flow will develop discontinuity if Π_1 and Π_2 are different. Due to this, a non-zero difference will be created at the junctions who accumulate or deplete heat (depending on the direction of the current). The heat current is always followed by electric current, and different materials have different drift velocities for the same current. The high energy carriers transport energy in the opposite direction of the current, because drift velocities depend on the energy of carriers located above the Fermi level. The heat transfer mechanism at the junction is sketched in Figure 1.4 [3].

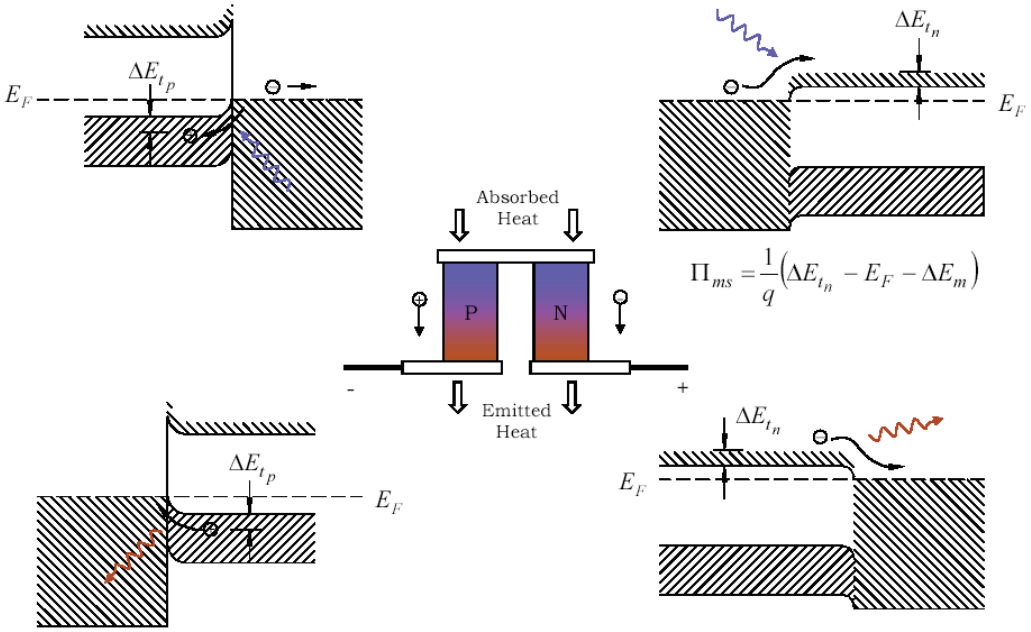

Figure 1.4: *Heat transfer across the junctions (adopted from T. Hogan MSU* [3]*)*

Figure 1.4 shows that heat is absorbed at one junction and emitted from the other one. Hence, the Peltier effect can be used to transfer heat from one junction to another, which is the principle of thermoelectric cooling. However, making Peltier cooling devices efficient by using typical conductors is a difficult task due to dominant Joule effect.

1.2.1.3 Thomson Effect

Thomson effect is the last of thermoelectric effects [4]. When a current flows and when a temperature gradient is present, there is also heat generation or adsorption because *S* is temperature dependent. The gradient of the heat flux is given by

$$\frac{dQ}{dx} = \tau I \frac{dT}{dx} \qquad 1.3$$

Where x is a spatial coordinate, τ is the Thomson coefficient, T temperature, I is the imposed current.

1.2.1.4 Kelvin relations

It is useful that both Thomson coefficient, τ and Peltier coefficient, Π, can be obtained from *S,* which is easily measured. Experiments confirmed the relationships derived by Kelvin:

$$\tau = T\frac{dS}{dT} \tag{1.4}$$

and the relation between Peltier and Seebeck coefficients is given by:

$$\Pi = ST \tag{1.5}$$

The last equation provides a fundamental link between thermoelectric cooling (Π) and thermoelectric power generation (*S*).

1.2.2 Electrical Conductivity

When conditions such as isotropy, a parabolic energy band and a Fermi distribution function are met, a general expression for electrical conductivity of a given material can be calculated from Boltzmann's transport equation as:

$$\overleftrightarrow{\sigma} = \frac{e^2}{4\pi^3}\int \xi\vec{v}(\vec{k})\,\vec{v}(\vec{k})\frac{\partial f_0}{\partial E}d3k \tag{1.6}$$

where $\overleftrightarrow{\sigma}$ is a symmetric second rank conductivity tensor, E is the energy level, ξ is relaxation time, $\vec{v}(\vec{k})$ is velocity of carriers, and f_0 is a dispersion function. Integral represented in equation 1.6 over all momentum space depends on the relation of $E(\vec{k})$ and $\vec{v}\vec{v}$ terms, and the temperature dependence of electrical conductivity comes from the $\frac{\partial f_0}{\partial E}$ term. Coming from 1.6, electrical conductivity can be simply written as:

$$\sigma = ne\mu = ne^2\frac{\tau}{m^*} \tag{1.7}$$

where *n* is the concentration of charge carriers, *e* is the electron charge, μ is the carriers mobility. Equation 1.7 explains that electrical conductivity mostly depends on effective mass m^* and relaxation time τ. Conductivity is also proportional to the concentration of dopants. Dopant is a trace impurity element that is inserted into a structure (in very low concentrations) in order to modify the electrical properties of the substance. In the case of crystalline substances, the atoms of the dopant very commonly take the place of elements that were in the crystal lattice of the base material. Dopants bring additional electrons in the valence band, which increases the chance for them to cross the band gap into the conduction band. The effective mass, m^*, is the second derivative of dispersion function of the carrier concentration around the Fermi level,

which is related to the materials intrinsic properties. These include electronic structure, crystalline structure, atomic mass, and structures such as nano-dots, superlattices, and quantum wells. Relaxation time, τ, is influenced by different scattering mechanisms, as it will discussed hereafter.

1.2.3 Seebeck Coefficient

General expression for the Seebeck coefficient can be written from the Boltzmann's equation as:

$$S = \frac{1}{eT}\frac{\int \sigma(E)(E - E_F)dE}{\int \sigma\,(E)\frac{\partial f_0}{\partial E}dE} \qquad 1.8$$

where $\sigma(E)$ is the electrical conductivity which metal would have, at absolute zero, if the Fermi level, E_F, came at the energy *E* [5], and f_0 is an equilibrium value of the distribution function when a conductor (or metal) is in equilibrium at a constant temperature *T* and with no electric or magnetic field acting on it. From Kelvin's relation (Equation 1.5), the right-hand side of Eq 1.8 represents the "isothermal energy flow" per unit current. Thus, Eq. 1.8 might be called the "Peltier definition" of thermoelectric power. Equation 1.8 says that the expected value of the energy difference of the carriers and Fermi energy are proportional to the Seebeck coefficient. In theory, if the low energy carriers are cut off, Seebeck coefficient can be vastly improved for a given material [6,7]. This is called energy filter phenomenon.

1.2.4 Thermal conductivity

While electrical conductivity explains the conduction of electricity, thermal conductivity describes the heat transport in solids. Electrical energy is transported as well as thermal energy when electrical carriers pass through a material. Thermal energy can also be transferred by phonons. From this point of view, the total thermal conductivity, κ_{total}, consists of two types of contributions:

1) Electronic contribution from carriers, $\kappa_{carrier}$;

2) Lattice contribution from lattice vibrations (phonons), $\kappa_{lattice}$.

Total thermal conductivity can be written as:

$$\kappa_{total} = \kappa_{carrier} + \kappa_{lattice} \qquad 1.9$$

According to the Wiedemann-Franz law [8], electronic thermal conductivity for metals and highly doped semiconductors (degenerated semiconductors) is proportional to electrical conductivity, and mathematically it is written as

$$\kappa_{carrier} = ne\mu \frac{\pi^2}{3}\left(\frac{k_B}{e}\right)^2 T \qquad 1.10$$

Equation 1.10 contains the Lorenz number (L) with $\frac{Kcarrier}{\sigma T}$ ratio. Its value, while roughly constant, is not exactly the same for all materials. Charles Kittel [9] gives some values for L ranging from $L = 2.23 \times 10^{-8}$ V^2/K^2 for copper at 0°C to $L = 3.2 \times 10^{-8}$ V^2/K^2 for tungsten at 100°C.

Expressions 1.7 and 1.10 are viable for metals or degenerated semiconductors.

Second contribution to thermal conductivity is lattice contribution. Lattice contribution exists due to lattice vibrations (phonons) that carry the heat. The lattice thermal conductivity for solids, by using classical kinetic theory, can be written as:

$$\kappa_{lattice} = \frac{C_v v_s l}{3} \qquad 1.11$$

where C_v stands for specific heat at constant volume, v_s is average sound velocity, and l is phonon's mean free path.

Phonon scattering is negligible at very low temperatures, so lattice thermal conductivity is dominated by Debye T^3 thermodynamics law for C_v. Specific heat has a classic constant value (3R) above the Debye temperature. As phonon velocity is independent of temperature, $\kappa_{lattice}$ is influenced primarily by the mean free path of a phonon (l).

Lattice thermal conductivity is a dominant heat transport mechanism even for higher temperatures. There are two ways to decrease $\kappa_{lattice}$ looking at equation 1.11:

1. Nanostructuration of the materials of interest because low group phonon velocities are encouraged due to a small first Brillouin zone;
2. Reduction of the phonon mean free path (l) by forming artificial boundaries in the material.

If scattering of phonons does not occur in a perfect and infinite crystal, the thermal conductivity will be infinite. For real crystals this is not the case, due to different types of scattering processes.

1.2.4.1 Scattering mechanisms

The mean free path of phonons is limited by several scattering mechanisms. At room temperature, thermal conductivity for semiconductors mostly exists due to acoustic phonons. Phonon-boundaries, phonon-defect, and phonon-phonon interactions are the major scattering mechanisms in thermoelectric materials.

1.2.4.1.a Scattering mechanism for carriers

Carriers are considered to be either electrons or holes, or both. For them, there are different types of carrier scattering such as carrier-phonon, carrier-defect, carrier-carrier, and carrier-impurity interactions [10]. Electron-phonon scattering is the most important one. In metals, most of the Brillouin zone is occupied by electrons, whereas in semiconductors, it is mostly unoccupied. In metals, scattering takes place from one point to another on the Fermi surface with large momentum changes, while in semiconductors, the change in momentum wave vector occurs only at a small angle. Thus, for semiconductors, the small angle scattering is important.

Number of scattering mechanisms can limit the mean-free path of carriers. They are all added on each other, and total relaxation time τ_{total} is represented as a sum of all scattering times from each scattering source. It is written as:

$$\frac{1}{\tau_{total}} = \frac{1}{\tau_1} + \frac{1}{\tau_2} + \cdots \frac{1}{\tau_i} \qquad 1.12$$

In the carrier-phonon scattering process in semiconductors, the probability that a carrier will change a state from initial to final position is proportional to the availability of states, to the probability of absorbing or emitting a phonon, and to the strength of the carrier-phonon interaction. Other carrier scattering processes are acoustic phonon scattering, optical phonon scattering, impurity scattering, scattering by dislocations, boundary scattering, inter valley scattering from one equivalent conduction band minima to another and carrier-carrier scattering. The two most common phenomenons are described hereafter.

1.2.4.1.b Phonon-phonon scattering

Phonon-phonon scattering is achieved through alloying as explained by Abeles et. al [11]. If all components of the alloy have similar crystal structure, the alloying effect will be greater resulting in a reduction of lattice thermal conductivity of the alloy. Phonon-phonon scattering satisfies both energy and momentum conservation laws and it is an important scattering mechanism.

In pure crystals at high temperatures, phonons are predominantly scattered by other phonons and the most important scattering process involves three phonons. The scattering of phonons satisfy both momentum and energy conservation laws. In normal processes (figure 1.5a), three phonons scatter with wave vector conservation equation:

$$\overrightarrow{k_1} + \overrightarrow{k_2} = \overrightarrow{k_3} \qquad 1.13$$

which implies simply a redistribution of phonons without any thermal resistance to first order, but in Umklapp process, the wave vector conservation follows:

$$\overrightarrow{k_1} + \overrightarrow{k_2} = \overrightarrow{k_3} + \vec{G} \qquad 1.14$$

where $\vec{G}$ (figure 1.5b) is the reciprocal lattice wave vector which makes all phonons lie in the allowed zone. This type of scattering with $\vec{G} \neq \vec{0}$ contributes to thermal resistance. This clearly shows that the Umklapp scattering process directly controls high temperature thermal conductivity.

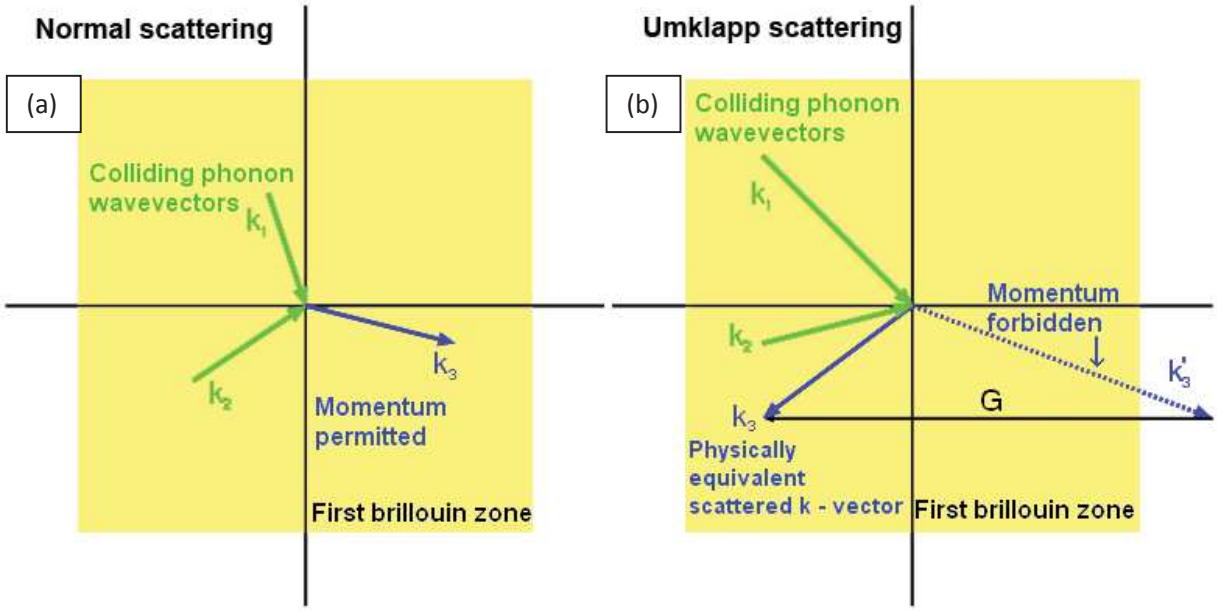

Figure 1.5: *(a) Normal scattering of three phonons; (b) Umklapp scattering.*

The relaxation time for the three-phonon Umklapp process at temperatures above the room temperature is given by:

$$\frac{1}{\tau_U} = 2\gamma^2 \frac{k_B T}{\mu V_0} \frac{\omega^2}{\omega_D} \quad 1.15$$

where μ is the shear modulus, γ represents the Gruneisen parameter which determines anharmonicity of the crystal lattice, V_0 is the volume per atom of the crystal lattice where phonon with the wave vector $\vec{k}_1$ can be located, and ω_D is the Debye frequency.

1.2.4.1.c Boundary scattering

Phonon scattering can happen at crystal boundaries, especially at low temperatures, for long wavelength phonons. This mechanism is important, as it is influenced by the grain size in a polycrystalline material. Boundaries can also scatter carriers (electrons), thusly lowering electrical conductivity (due to loss of carrier's mobility). However the reduction of thermal conductivity is greater when caused by phonon scattering compared to the reduction in mobility caused by carrier scattering. Expression of boundary scattering relaxation time is:

$$\frac{1}{\tau_B} = \frac{v}{D}(1-p) \quad 1.16$$

Here D is the grain diameter (the grain size in a polycrystal), *v* is the velocity of the phonon, and 1-*p* is the probability of scattering.

1.2.5 Thermoelectric Figure of Merit

Dimensionless figure of merit, ZT, represents the main parameter that describes the performance of thermoelectric materials. It is defined as:

$$ZT = \frac{S^2\sigma}{\kappa} \quad 1.17$$

where *S* is the Seebeck coefficient, σ is the electrical conductivity, and κ is the thermal conductivity. Numerator $S^2\sigma$ represents the power factor. Observing equation 1.17, it is obvious that a good thermoelectric material should have a power factor value as high as possible and a thermal conductivity as low as possible.

Values of *S*, σ, and κ are influenced directly by the carrier concentration (figure 1.6). With the increase of the carrier concentration, there is an increase of electrical conduction. As a disadvantage, thermal conductivity increases and Seebeck coefficient decreases with the increase of carrier concentration which lowers the thermoelectric figure of merit. According to

the same figure 1.6, the highest value of ZT is exactly in the semiconductor region with carrier concentration values range being $10^{19} – 10^{20}$ cm^{-3}.

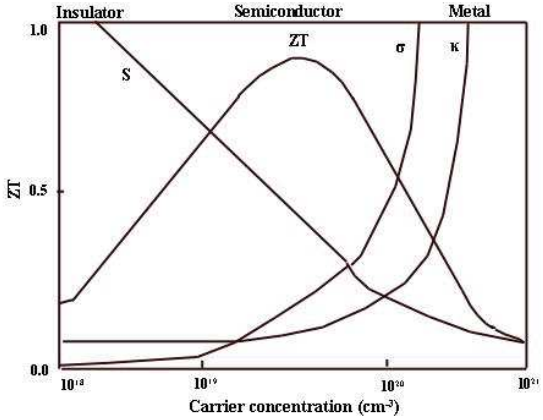

Figure 1.6: *S, σ, and κ in relation to carrier concentration.*

Intrinsic semiconductor or i-type semiconductor is a pure semiconductor without any significant dopant species present. In intrinsic semiconductors the number of excited electrons and the number of holes are equal. Introducing a doping agent to an intrinsic semiconductor gives an extrinsic semiconductor. During doping, impurity atoms of different elements act as either donors or acceptors, thus changing electrons and holes concentration of the intrinsic semiconductor. Donor impurity atoms have more valence electrons than the atoms they replace in the intrinsic semiconductor lattice giving them higher amount of electrons to pass to valence band and increase the electrical conductivity. There are two different types of extrinsic semiconductors: n- and p-type.

Extrinsic semiconductor which has larger electron concentration than holes concentration is called an n-type semiconductor. In an n-type semiconductor, the Fermi level is greater than that of the intrinsic semiconductor and lies closer to the conduction band than the valence band (Figure 1.7). As opposed to n-type semiconductors, p-type semiconductors have a larger holes concentration than electron concentration. Holes are the main carriers, and electrons are the minor carriers. P-type semiconductors are created by doping an intrinsic semiconductor with acceptor impurities. For p-type semiconductors the Fermi level is below the intrinsic Fermi level and lies closer to the valence band than the conduction band (figure 1.7).

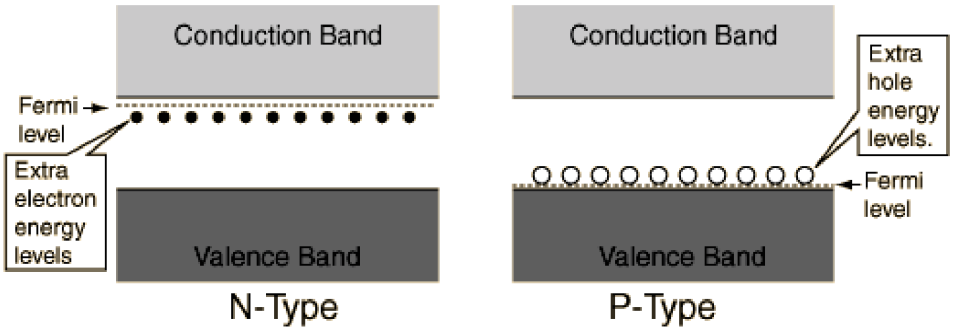

Figure 1.7: *Fermi levels for two different extrinsic semiconductor types.*

1.2.6 Thermoelectric device efficiency

Thermoelectric devices are used either for power generation or for thermoelectric cooling. These devices are built out of thermocouples made by assembling p and n-type thermoelements (electrically in series and thermally in parallel). Ratio of the electrical power that is brought to the load to the heat absorbed at the hot junction represents the efficiency of a thermoelectric generator. In 1957, A.F. Ioffe defined the efficiency as:

$$\eta = \frac{(T_H - T_C)}{T_H} \frac{(1+\overline{ZT})^{1/2} - 1}{\frac{T_c}{T_H} + (1+\overline{ZT})^{1/2}} \qquad 1.18$$

The $\frac{(T_H - T_C)}{T_H}$ represents the maximum value of a thermal device and it is called the Carnot efficiency. Modified dimensionless figure of merit $\overline{ZT}$, takes into consideration the thermoelectric capacity of both thermoelectric materials (n- and p-type) used in the device, and is defined as:

$$\overline{ZT} = \frac{\left(S_p - S_n\right)^2 \bar{T}}{\left[(\rho_n \kappa_n)^{1/2} + \left(\rho_p \kappa_p\right)^{1/2}\right]^2} \qquad 1.19$$

where ρ is the electrical resistivity, S is the Seebeck coefficient, κ is the thermal conductivity, $\bar{T}$ is the average temperature between the hot and cold surfaces, and n and p denote n- and p-type semiconducting thermoelectric materials respectively. The thermoelectric devices are heat engines, and their efficiency is limited by the Carnot limit.

Carnot limit is an absolute limit for the efficiency with which heat energy can be turned into useful work. Depending on the value of ZT, the efficiency of the device can be calculated based on the temperature of the hot surface (Figure 1.8).

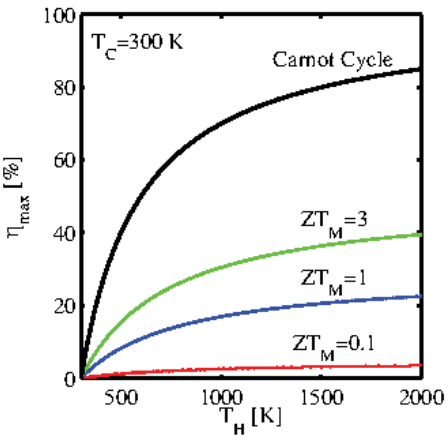

Figure 1.8: *Efficiencies of a device with different figure of merits (ZT).*

It is necessary to develop materials with ZT>2-3 to be competitive compared to current engines and refrigerators (efficiency 25-40 percent of Carnot limit). Higher ZT scores are a way to rank thermoelectric materials. The higher the score the closer the material is to Carnot's limit (ultimate efficiency for heat engines).

1.2.7 Influence of the microstructure on thermoelectric properties

Research towards maximizing ZT for well-known thermoelectric materials (Bi-Te) was completed in 1960s. The fundamental understand of ZT optimization was done via doping and in the next few years the figure of merit was increased by slight amount.

As we mentioned, there are two major parts to the figure of merit: power factor (PF) and thermal conductivity. We strive to increase the value of the PF while reducing thermal conductivity.

Increase in the electrical properties (and power factor) can be achieved by low dimension effects. This was reported in 1991 by Iijima for carbon nanotubes [12]. These new morphologies opened a new theoretical framework for using low-dimensional structures to enhance the figure of merit even in materials whose parameters have already reached near optimization via conventional techniques [13]. Thusly, a materials fabricated into an effectively 2D "superlattice," can have a figure of merit as high as 14. This could happen only due to the morphology of the sample. The potential for this approach lies in the increase of the power factor instead of the reduction of the thermal conductivity for a system comprised of multiple quantum wells, when the well width is greater than ~1nm [14]. Enhancement of the figure of merit is seen primarily due to quantum confinement effects in the thermopower and in the electronic density of states. Subsequent work in an epitaxially grown PbTe/$Pb_{1-x}Eu_xTe$

superlattice with ~2nm PbTe layer widths but very thick $Pb_{1-x}Eu_x$ barrier widths (on the order of 35 nm) confirmed the predicted thermopower/density of states enhancement in an effectively 2D system, where electronic conduction was constrained to the PbTe layers of the superlattice. Here, PF achieved a maximum of ~50x the value seen in bulk PbTe [15]. A little bit later [16] Bi_2Te_3/Sb_2Te_3 superlattice was shown to achieve a ZT value of ~2.4 due to phonon scattering between the layers. Soon after, the similar effect was observed for $PbTe/PbSe_xTe_{1-x}$ superlattices. Additionally, the low-dimensional structures began to attract widespread interest in thermoelectric research.

Low dimensional approach was also observed in a 3D superlattice structure, one in which the alternating layers are all on the order of 2nm [17], in contrast to the precious power factor enhancement seen only when one layer is effectively isolated by a large buffer layer [15]. It is therefore in principle easy to conceive of a superlattice structure that employs both phonon blocking and quantum confinement effects, though research efforts have yet to produce such a material.

Superlattices can achieve high figures of merit, but they are best suited for thin-film application and not for bulk application. Alternative approach for bulk materials is to create a nanocomposite material. The idea is to incorporate some form of a nanostructure into a bulk material in such a way that the properties of the composite material benefit from both components, ideally with an overall improvement in the figure of merit. Further advantages such as ease of manufacture and greater potential of scalability may also be achieved. One of the earliest attempts at producing such composite relied on the incorporation of small diameter (9-15 nm) Bi nanowires into porous alumina or porous silica and showed an enhancement of the thermopower consistent with the prediction of quantum confinement. Due to the structure of the composite, the resistivity could not be measured, and therefore no figure of merit data could be calculated [7].

When we have a polycrystalline material, we can use inclusions or precipitates to influence the conductivity (electrical and thermal). Additionally, if the inclusions concentrate on the borders of the grains, then a limited grain growth is imposed [18]. These inclusions reduce the sizes of the grains and crystallites by inhibiting the growth during the thermal process of consolidation such as sintering. Electrical properties of the material are modified by the inclusions inside the material as it was reported by Alleno [18]. As the research of low dimensional materials showed great promise, the idea was transferred to bulk nanostructured materials formed of nanoparticles or nanocomposites in order to increase the number of interfaces. Consequently, the lattice thermal conductivity was reduced by phonon scattering at interfaces.

The electrical properties may be influenced by doping, thusly increasing the power factor (electrical conductivity). Incorporating inclusions in the nanocomposites can have a negative

effect upon the electronic properties. Although nanoparticles have been shown to have a positive effect especially upon the low temperature thermal conductivity, in many cases the detriment posed to the electronic properties outweigh any benefits to the thermal conductivity. One method to circumvent this difficulty could be to incorporate nanoparticles with excellent electronic conductivities directly into the matrix.

While their excellent electrical conductivity could possibly increase the electronic part of the thermal conductivity, if the particle size is kept small enough, the particles could possibly serve as sites of point defect scattering of phonons thereby decreasing the thermal conductivity. As phonon point defect scattering is an effect that comes into play at higher temperatures than boundary scattering of phonons, such an approach could potentially reduce the thermal conductivity for thermoelectric materials found above 300 °C.

To reduce the thermal conductivity, reduction can be obtained by introduction of inclusions or precipitations (to act as phonon diffusers) in a matrix. Reduction can be of several percent, depending on the size of the inclusions [18]. The extra reduction in the thermal conductivity for sintered materials can be attained by the increase of the phonon scattering at grain boundaries. The existence of an additive compound (or second phase) in sintered materials is effective in this case and can be found on the borders and inside the matrix.

It is the purpose of this thesis to create a nanocomposite and by adjusting the process of synthesis and sintering incorporate large amount of inclusions inside the grain and on its boundaries. The impact of these inclusions will influence the thermoelectric properties, especially if they are nanosized.

1.3 Thermoelectric materials

Different types of materials are investigated to test their thermoelectric properties and their potentional use in a thermoelectric device. Researchers focus on the connection and the influence that *band gap, carrier concentration, effective mass, relaxation time*, and *scattering parameters* have on the targeted Seebeck coefficient, electrical conductivity and thermal conductivity. A material with those desired thermoelectrical properties should have a high value of the materials parameter, β (introduced by Chasmar and Stratton [12]), mathematically written as:

$$\beta = \left(\frac{k}{e}\right)^2 \frac{\sigma_0 T}{\kappa_{lattice}} \qquad 1.20$$

And

$$\sigma_0 = 2e\mu\left(\frac{2\pi m^* k_b T}{h^2}\right)^{3/2} \qquad 1.21$$

where k_b is the Boltzman constant, h is the Planck constant and e is the electron charge. Equations 1.20 and 1.21 state that the best thermoelectric materials should have high mobility of carriers, μ, large effective mass, m^*, and low lattice thermal conductivity, $\kappa_{lattice}$. Creating alloys with complex structure enhances phonon scattering, thus improving the thermoelectric materials.

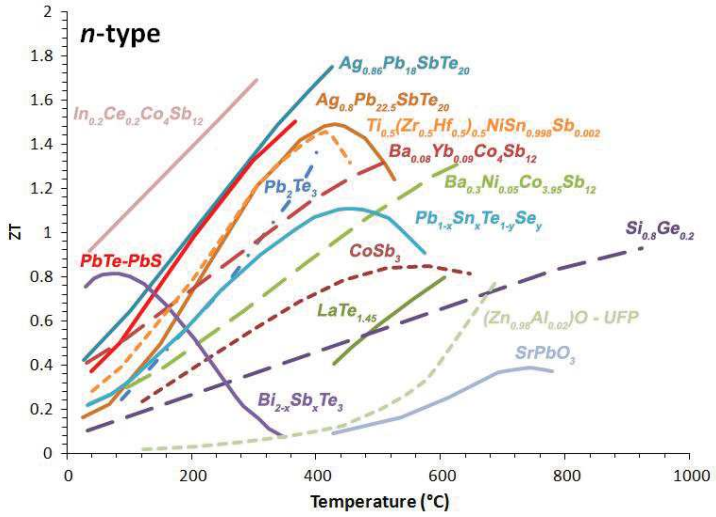

Figure 1.9: *ZT values in function of temperature for n-type thermoelectric materials* [13,14].

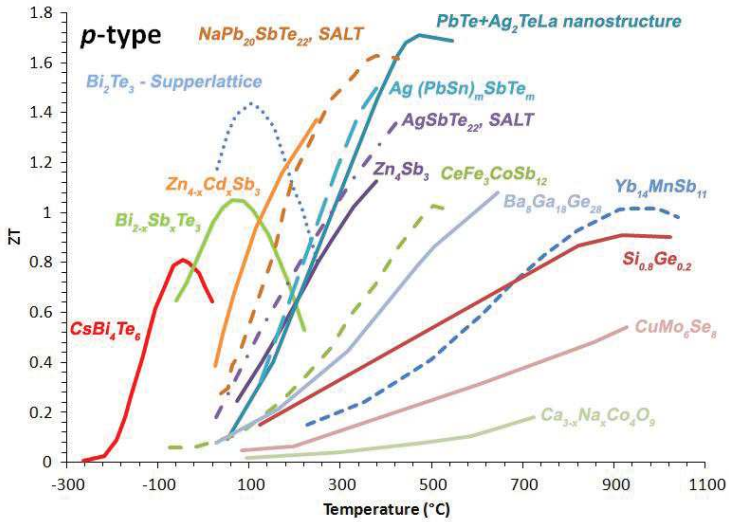

Figure 1.10: *ZT values in function of temperature for p-type thermoelectric materials* [13,14].

Thermoelectric materials are divided according to the temperature where they have the maximum value of ZT. In that manner, we can discuss about the temperature range of usage of thermoelectric materials. C. Godart [13] and J. R. Sootsman [14] have shown different ZT values in different temperature range for n-type (Figure 1.9) and p-type (Figure 1.10) thermoelectric materials. They stated that each material system has ZT maximized on a specific working temperature range.

Performances of different thermoelectric materials families will be exposed in next few sub-chapters.

1.3.1 Very low temperatures (T<-73°C)

Bismuth-antimony alloys ($Bi_{1-x}Sb_x$) used for very low temperatures (less than -73°C) applications, reported by [15,16,17], show that they have the best n-type characteristics. The maximum value of ZT is around 1.1 at 200 K. The ZT value increases considerably in a magnetic field [18]. In pure bismuth crystals and bismuth-antimony alloys, at least with small antimony proportions, the Seebeck coefficient can also change sign from negative to positive when the magnetic field becomes strong. There is no valid p-type material.

1.3.2 Low temperatures (RT<T<300°C)

Temperature ranging between the room temperature and 300°C is reserved for Bi_2Te_3 compounds that are doped with antimony and selenium, to create p- and n-type materials, respectively. They are considered to be the most efficient thermoelectric materials in this group with a ZT around 1 at room temperature. Bi_2Te_3 is a narrow-gap semiconductor with an indirect gap of approximately 0.15 eV. It crystallizes in the rhombohedral space group that consists of five atomic layers (Te1-Bi-Te2-Bi-Te1), stacked by van der Waals interactions along the c-axis in the unit cell. Bismuth atoms are coordinated with six tellurium atoms in octahedral geometry.

As the quantity of tellurium changes in the chemical composition of the Bi-Te alloy, Seebeck coefficient changes from negative (creating a n-type material) to positive (creating a p-type). Thusly, extrinsic n and p-type semiconductor based on Bi-Te alloy can be easily produced without additional doping. The Seebeck coefficient of this phase is directly connected to the chemical composition. Maximum value of ZT at room temperature for Bi-Te alloy synthesized this way was reported to be 0.86 for an n-type and 0.75 for a p-type material [19,20].

Alloying Bi_2Te_3 with Sb creates a p-type material where Seebeck coefficient can reach a value of 280 S/m at room temperature. Alloying reduces the lattice contribution to thermal

conductivity for p-type $Bi_{0.5}Sb_{1.5}Te_3$. This is also reported for n-type $Bi_2Te_{2.7}Se_{0.3}$ alloys. Figure of merit for these materials is around 1 at room temperature [21].

While the Bi-Te compounds are still investigated and introduced into thermoelectric devices, the toxicity, rarity and prices of its elements are still an important issue.

1.3.3 Medium temperatures (300°C<T<600°C)

Bi-Te alloys are not usable above 250-300°C. The most researched alloy in this temperature range is Lead-telluride (Pb-Te). Lead-telluride has been studied for thermoelectric application back in 1957 by Ioffe [22].

Lalonde described a normal manufacturing process of Pb-Te alloys [23]. Polycrystalline samples of Pb-Te alloys were prepared by melting the stoichiometric ratio of elemental Pb and Te in vacuum sealed quartz ampoules, at 1000 °C for 6 hours, followed by water quenching and then annealing at 700°C for 48 hours. The annealed ingots are then ground to powder and consolidated by hot pressing under 44MPa at the temperature of 550 °C. From there, the fabrication of polycrystalline samples of PbTe proves to be tedious, where every subsequent step increases the production time and price of the final thermoelectric material.

PbTe crystallizes in the NaCl crystal structure with Pb atoms occupying the cation sites and Te forming the anionic lattice. Doping is easily achievable because of a band gap of 0.32 eV. It was reported by Goldsmid [24] that an n-type Pb-Te alloy can be created by adding dopants such as Zn, Cd, In, Bi, and Cl, while for a p-type Pb-Te alloy Na, Au, Ti and O dopants were used.

Pb-Te performance can be improved by substituting Te with Se or Pb with Sn. Two enhanced alloys were created: a p-type $Pb_{1-x}Sn_xTe$ and an n-type $PbTe_{1-x}Se_x$. The highest value of figure of merit for p-type $Pb_{1-x}Sn_xTe$ and $Pb_{1-x}Te_x$ around 450°C is 1 and 0.8, respectively [25]. Adding In to $Pb_{1-x}Sn_xTe$ alloy (p-type material) did not improve its thermoelectric properties because the resonance level was not properly located in the valence band [26]. Doping with Tl created a p-type material, influenced electrons to be properly located in the valence band and ZT value was found to be 1.5 at 500°C [27]. Bisvas et al. [28] created nanoscaled PbTe-SrTe (4 mol%) and added 2% Na, then consolidated it with spark plasma sintering (SPS) to create a p-type thermoelectric material with the highest ZT value recorded in this material group of 2.2 at 623°C. Sodium was added to promote the formation of endotactic nanometer-sized inclusions that contribute to a strong decrease of the thermal conductivity.

Lead antimony silver telluride (LAST-m), an n-type material, is one of many derivates from the Pb-Te system. It was developed with a combination of PbTe and $AgSbTe_2$. Another derivate is sodium antimony lead telluride (SALT-m), a p-type material, with composition $NaPb_mSbTe_{2+m}$ that has a ZT of 1.6 at 400°C. This material has a really low thermal conductivity of 0.85 $Wm^{-1}K^{-1}$ of which approximately 0.5 $Wm^{-1}K^{-1}$ is the lattice contribution [29]. Additionally, a p-type $(Pb_{0.95}Sn_{0.05}Te)_{1-x}(PbS)_x$ composite was reported with a ZT of 1.5 at 400°C [30].

Two additional groups of materials used at medium temperatures are skutterudites and clathrates.

Clathrates are intermetallic compounds in which tetrahedrally bonded atoms form a framework of cages that enclose guest metal atoms. These materials have the $X_8Y_{16}Z_{30}$ (X=Ca, Sr, and Ba ; Y=Al, Ga, and In ; Z=Si, Ge, and Sn) generic formula. High figures of merit (ZT>1) were reported for n-type $Sr_8Ga_{16}Ge_{30}$, $Ba_8In_{16}Sn_{30}$ [31], and p-type $Ba_8Ga_{16}Ge_{30}$ [32]. Production of these materials is time consuming with low production yields.

Skutterudites have the MX_3 generic formulation where M is a metal such as Co, Rh, or Ir and X is P, As, or Sb. Improved thermoelectrical materials have a the general chemical formula LM_4X_{12}, where L is a rare earth metal, M a transition metal, and X is a metalloid. Most popular formulation are $CoAs_3$ and $CoSb_3$ [33] from which different compounds are created, including an n-type skutterudite $Ba_{0.08}La_{0.05}Yb_{0.04}Co_4Sb_{12}$ which has a ZT of 1.6 at 550°C [34], and a p-type $R_xM_yFe_3CoSb12$ (R,M =Ba, Ce, Nd, and Yb) with a ZT ~1.06 at 550°C [35].

Critical elements for clathrates are some rare-earth elements (Ce, Eu, Ba, Au, In) which increases the price of these materials. Safety hazards also exist due to use of Ce, Hg, Pb, and As. Skutterudites also use some of the rarest elements such as rhodium (Rh), Barium (Ba), Ytterbium (Yb) and iridium (Ir). Rarity of these materials may be seen on figure 1.11.

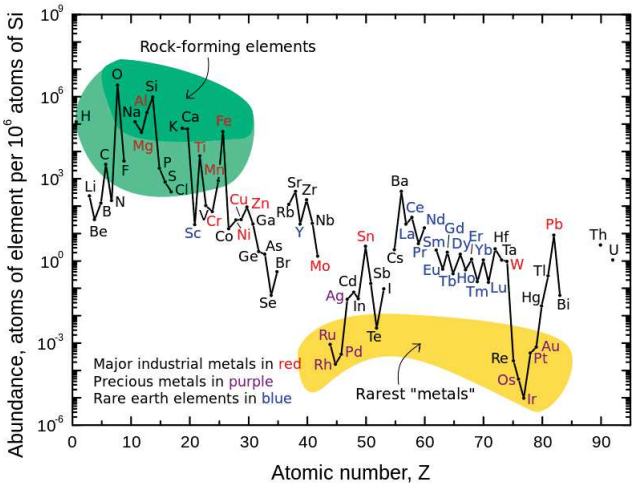

Figure 1.11: *Abundance of elements.*

Both n and p type Pb-Te alloys are commercialized but the problems of high toxicity as well as high costs of manufacturing processes and raw elements still remain. For that reason, research has been oriented towards Mg_2B^{IV} alloys (B=Si, Ge, or Sn). These materials have been

deeply investigated for thermoelectrical application in the 300-600°C temperature range [36,37,38,39,40,41,42,43,44].

Manufacturing of n-type $Mg_2Si_{1-x}Sn_x$ ($0.2<x<0.8$) alloys doped with antimony is described by Liu using a two-step solid state reaction method [35,37,42,43,44]. It is a cumbersome process where precursor powders were stoichiometrically mixed in an agate mortar in a glove box with argon. Afterwards, the mixed powders were pressed into cylinders at 20 MPa and then placed in boron-nitride crucible that were sealed in quartz tubes in vacuum for the solid state reaction at a temperature of 700°C. To increase the homogeneity of the products, the resulting pellets were ground to fine powders in a glove box filled with argon, cold-placed into cylinders at 10 MPa, and again placed in boron-nitride crucibles and sealed in quartz tubes in vacuum for a second-stage solid state reaction at the same temperature. Finally, the resulting pellets were ground again to fine powders in the glove box, and sintered using spark plasma sintering (SPS) at 715°C. This is a standard method for producing a homogeneous polycrystalline $Mg_2Si_{1-x}Sn_x$ material. Additional steps of annealing for prolonged time can be introduced after the second-stage solid state reaction to further increase the homogeneity.

Zaitsev manufactured polycrystalline ingots of $Mg_2Si_{1-x}Sn_x$ solid solution by direct melting of the components in boron nitride crucibles using high-frequency heating [39,38]. After this step a long-time annealing treatment was applied to the ingots for homogenization of the samples. Concentration of current carriers was controlled by antimony additions. In the temperature range of 430 to 530 °C the ZT achieved the maximum value around 1 for n-type $Mg_2Si_{0.4}Sn_{0.6}$ [38].

Gao et al. [45] published the highest ZT value of 1.5 at 445°C for an n-type $Mg_{2.08}Si_{0.364}Sn_{0.6}Sb_{0.036}$ polycrystalline composition made by B_2O_3 flux synthesis method in air, in a box furnace. Stoichiometric amounts of elemental powders were weighted in argon filled glove box and homogeneously mixed in Al_2O_3 crucibles. As always with melting techniques, an excess of Mg is required to compensate the loss of Mg during the synthesis process. The mixture was then compacted and covered by a graphite foil and gently pressed before the alumina crucible was placed in a box furnace which was preheated to 700°C. Mixed powders were annealed for 12h in air at 700°C. After the material had naturally cooled at room temperature, the alumina crucible was broken to separate B_2O_3 seal from the cast ingot. Ingot was then ground using an agate mortar and pestle, and then sieved. These powders were consolidated using SPS.

Liu et al. [42] obtained a ZT value of 1.3 for an n-type $Mg_{2.14}Si_{0.39}Sn_{0.6}Sb_{0.009}$ material in the temperature range between 465 and 510°C. Stoichiometric amounts of high purity powders were mixed with 8 mol% excess of Mg to compensate the evaporation of magnesium which occurs during high temperature treatment of the powder. Constituents were hand-ground in an agate mortar in a glove box, cold pressed and sealed in quartz tubes under vacuum for the first

step a solid state reaction at 600-700 °C. The reaction products from the first process were again ground into fine powders in the glove box, cold pressed into a bulk, sealed in a quartz tube under vacuum and annealed at 700 °C in order to promote the formation of solid solutions and increase the homogeneity of the elements. After this, the products were ground again into powder and consolidated into dense bulk materials by SPS.

Zhang used induction melting with ball milling and hot pressing to create a dense sample [40] of an n-type material with $Mg_2Si_{0.3925}Sn_{0.6}Sb_{0.0075}$ formulation and achieved a ZT value of 1.1-1.2 at 530°C. He melted molar ratios of three elements (with 8 wt% excess of Mg), crushed the products into powders in an argon filled glove box and sintered them by SPS in a furnace at 700-750°C.

Only few attempts have been made to develop a p-type $Mg_2Si_{1-x}Sn_x$ material. A first one was published by Isoda [46]. He said that stoichiometrical reduction of magnesium in Mg-Si-Sn alloys creates a p-type material. He double-doped the $Mg_{1.98}Si_{1-x}Sn_x$ alloy with Ag and Li and obtained a ZT of 0.32 at 500°C.

Additional way of creating a p-type material is by changing Sn atoms in $Mg_2Si_{1-x}Sn_x$ solid solutions with Ge to create $Mg_2Si_{1-x}Ge_x$ compounds. Mars [47] doped $Mg_2Si_{0.6}Ge_{0.4}$ with Bi_x (x=0.02) to create an n-type with a ZT∼1 at 600°C, or a p-type when doped with Ag_x (x=0.02) with a ZT∼0.28 at 600°C [47]. Mars placed the constituents in adequate proportions into a tantalum crucible inside a glove box to prevent oxidation. Subsequently the tantalum crucible was placed in a quartz tube. The synthesis was performed under a flowing He/H_2 gas mixture in vertical and horizontal furnaces. Desired Mg concentration is maintained by adding 1 mol % additional Mg in the mixture. The homogeneity of the products was then refined by two days of annealing at 500 °C. Hot pressing followed after grinding of collected ingots.

Ihou-Mouko also reported [48] that doping $Mg_2Si_{0.6}Ge_{0.4}$ with Ga_x (x=0.4 mol %, 0.8 mol %) produces a p-type thermoelectric material with a highest ZT value of 0.36 at 377°C. The constituents (Mg, Si, Ge, and Ga) were placed in a glassy carbon crucible and then placed in Ta cartridges which were sealed by arc-welding in a glove-box under argon. The Ta container was placed into silica containers under vacuum and annealed for 2 days at 750 °C for its first thermal treatment. Powder was then crushed mechanically, placed again in the two crucibles and annealed again for 2 days at 750 °C under vacuum. Afterwards, ingot was crushed and powders were hot pressed for 2 h in argon atmosphere under 50 MPa at 800°C.

Development of a p-type $Mg_2Si_{1-x}Sn_x$ material is still undergoing extensive research. Isoda [46] double-doped the $Mg_2Si_{0.25}Sn_{0.75}$ solid solution with Ag (20000 ppm) and Li (5000 ppm) and produced a ZT value of 0.32 at 500°C. Isoda produced lithium from lithium acetate using a thermal decomposition temperature of 250°C. 5 mol% of excess magnesium was added to compensate for Mg loss by evaporation. The alloy was synthesized by a liquid-solid reaction

method using graphite crucibles. Ingots were then crushed in an alumina mortar and sieved out to 38 µm to 75 µm. Powders were then hot pressed under pressure of 50 MPa at 660 °C for one hour.

In the temperature range of 300-600°C, higher manganese silicides (HMS, $MnSi_{1.72-1.77}$) are reported to have high figures of merit for a p-type material [49,50,51]. The lowest thermal conductivity was found for $MnSi_{1.75}$ [49], where the maximum value of ZT is 0.5 at 590°C. HMS can be an alternative to p-type $Mg_2Si_{1-x}Sn_x$ alloys in the 300-600 °C temperature range if developments are finally unsucessfull

The highest value of ZT (0.6-0.65 at 550°C) was reported by Aoyama [50]. He created single crystals of HMS, and doped them with Al. Constituents were synthesized into $MnSi_{1.74-y}Al_y$ solid solution. Mixture was loaded into a quartz ampoule which was placed in a modified Bridgman furnace. The starting ingot for growing a single crystal was obtained by melting the mixture at 1200 °C for 1 hour in Ar atmosphere. The ingot obtained was then crushed and loaded into another quartz ampoule, which was again placed in the modified Bridgman furnace. A starting temperature of 1150 °C, a feed speed of 30 mm/h and a temperature gradient of about 3K/mm were used for growing a single crystal. This was done just for the optimization of the Al content. Same procedure was then used to create a HMS with additions of Mo and Ge, creating the composition $(Mn_{0.98}Mo_{0.02})(Si_{0.9865}Al_{0.0035}Ge_{0.01})_{1.74}$, exhibiting, finally, the highest ZT values.

Luo [51] published his findings on $MnSi_{1.75}$ solid solution. He took the constituents of Mn, and Si, mixed them with an adequate composition, and pressed them to a disk. Under argon atmosphere, a disk was induction melted at 1450 °C for 5-10 minutes. Collected ingot was then placed in a quartz tube and induction melted to create ribbon-shaped objects that were supercooled (melt spinning) and pulverized into powder. The powder was then loaded into a graphite die and consolidated by SPS. Luo obtained a ZT value of 0.62 at 600°C.

HMS is a p-type material consisting of manganese and silicide which are abundant, cheap, eco-friendly and safe for manipulation (non-toxic). HMSs are used as a p-type material for creating thermoelectric generators and they are compatible with the n-type $Mg_2Si_{1-x}Sn_x$ solution [50].

1.3.4 High temperatures (above 600°C)

Silicon germanium alloys are most researched thermoelectric materials for the high temperature applications (above 600°C). Solid solution of $Si_{1-x}Ge_x$ has high thermal conductivity which is why ZT is below 1. Nanostructurization gives Si-Ge higher values of ZT around 1.3 at 900°C [52] for an n-type and 0.9 [53] for a p-type at the same temperature. These alloys are non toxic and they are already used for space applications.

To efficiently increase the ZT parameter of Si-Ge alloys, theoretical calculations have shown that incorporating an optimal volume fraction of metal or semiconductor silicides that are crystalline in nature, having structure and lattice parameters matching as much as possible with the crystalline surrounding matrix, is of prime interest. For example, dispersing homogeneously 3.4 vol.% of $MoSi_2$ nanoparticules (average diameter 10-20 nm) in a $Si_{0.5}Ge_{0.5}$ matrix decreases thermal conductivity at room temperature by a factor of 4-5 comparing to $Si_{0.5}Ge_{0.5}$ without addition. A ZT parameter value of ~1.7-1.9 is then calculated at a temperature of 630°C, and should exceed a value of 2 at temperatures above 850-900 °C [54].

Germanium-poor Si-Ge alloys are interesting due to the high cost of germanium. Joshi [3] has obtained a ZT value of ~0.5 at 700°C for $Si_{0.90}Ge_{0.10}B_{0.05}$ p-type composition and Wang [55] a ZT of ~0.9 at the same temperature for a $Si_{0.90}Ge_{0.10}P_{0.02}$ n-type alloy. Both of them observed polycrystalline sintered microstructures, where the average grain size is in the range 10-20 nm.

K. Favier [56] published that the ZT parameter can be improved by dispersing homogeneously a second phase in a germanium poor Si-Ge alloy. Matrix of $Si_{0.913}Ge_{0.08}P_{0.007}$ was mixed with 1.3 vol.% of $MoSi_2$ which were mechanically alloyed first separately, then together in a second time, in a planetary ball mill. The $MoSi_2$ inclusions lowered the thermal conductivity, thusly increasing ZT value to 1 at 700°C which is an improvement over the matrix itself which had a ZT value of only 0.7 at the same temperature.

1.4 Thermoelectric devices

The basic unit of a thermoelectric generator (TEG) or refrigerator (TEC) is a “thermocouple” that consists of n-type and a p-type thermoelements (Figure 1.12).These thermoelements are considered to be a basic unit (or a basic building-block) for construction of thermoelectric modules. Therefore, a thermoelectric module consists of a number of basic units connected electrically in series by a conducting strip (usually copper) but thermally in parallel and sandwiched between two ceramic plates. Thermoelectric modules can be prefabricated as general purpose products in different dimensions.

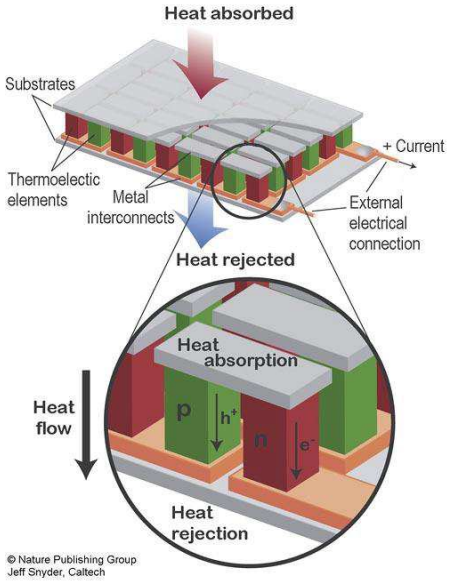

Figure 1.12: *Thermoelectric device with a zoomed in look on the thermocouple* [57].

The generating performance of a thermoelectric module is measured primarily by the conversion efficiency and power-per-unit area, while the cooling performance is measured by the coefficient of performance (COP) and heat-pumping capacity.

1.5 Optimization of thermoelectric performances

The last decade of the 20th century was an age of renaissance for thermoelectric materials. Dresselhaus [58] made a theoretical study about how the low structure dimensions of materials would be able to increase the figure of merit (ZT) up to 3.5. This echoed through the scientific community and the race for the best thermoelectric materials has begun.

Thermoelectric materials are also called “phonon-glass-electron-crystals” [59,3], because they should have low lattice thermal conductivity like glass, and increased electrical conductivity as in crystals. Two different approaches were created, where one aimed on reducing the thermal conductivity through boundary scattering, and the second one on improving the power factor by enhancing the density of states. First approach dealt with advanced bulk materials with complex crystal structures and nanostructurization (nanometer grain size, precipitation of nanometer-sized objects in a surrounding matrix…) [60,61], while the former dealt with low dimensional materials (superlattice structures of Bi_2Te_3 and PbTe, for example) [62,63].

1.6 Our approach

Both n-type magnesium-silicide-tin and p-type manganese-silicide alloys have a great potential for thermoelectric application in the mid-range temperatures (300°C-600°C). They have high ZT, while staying eco-friendly, cheap, and are available in abundanse. Also, working with them has no safety hazards when compared to other alloys (e.g. Pb-Te or Bi-Te alloys). We believe that $Mg_2Si_{0.4}Sn_{0.6}$ and $MnSi_{1.75}$ are pertinent choices for future thermoelectric devices. However, it will be also very interesting to be able to manufacture p-types Mg-Si-Sn alloys instead of using MnSi as a p-type solution. Only one material for both kinds of thermoelectric legs simplifies strongly the thermomechanical problems that could be encountered when legs are introduced in a real TEG. As it was published by Aoyama [50], the Mg-Si-Sn and Mn-Si alloys are compatible. A maximum efficiency of $\eta_{\max}\sim 8\%$ at 600 °C with a power output of $P_{\max}\sim 7$ W was monitored. Consequently, the PhD Thesis has focused on n and p-types $Mg_2Si_{1-x}Sn_x$ alloys, with p-type $MnSi_{1.75}$ being considered as a backup solution.

Experimental methods used by Zhang [40], Zaitsev [38], and Gao [45] to synthetize, up to now, $Mg_2Si_{1-x}Sn_x$ alloy are too complex (many different steps) and take too much time and effort to be commercialized and mass produced. This is also valid for Mn-Si alloys, as was published by Aoyama [50] and Luo [51]. One of this dissertation's goals is also to identify an easier way to create a fully dense materials using:

1) Mechanical alloying (MA) to elaborate the raw powders - we will show that mechanical alloying is a better way to synthesize $Mg_2Si_{1-x}Sn_x$ alloys, especially because it is a one step process. When an alloy is created by mechanical alloying, the homogenization and annealing treatments are obsolete as the produced alloyed powder is already homogeneous;

2) Spark Plasma Sintering (SPS) - Powder could be immediately loaded into a graphite die and consolidated into pellets after MA in only few tens of minutes. Additional treatments are not necessary, and high figure of merit is possibly achievable by tailoring the sintering parameters (maximum temperature, pressure, heating rate, soak time, cooling rate...).

Then, one of the goals of this PhD Thesis is to produce the targeted n/p-type Mg-Si-Sn and possibly p-type Mn-Si materials as simply as possible. Doing so, we will put an effort to improve the thermoelectric properties by optimization of the processing steps (MA and SPS).

Experimental methods used for production of the materials (mechanical alloying and spark plasma sintering - SPS), measurements of the thermoelectric properties and investigation of the sintered microstructure are detailed in the next chapter.

CHAPTER 2

Phase diagrams and structure of Mg-Si-Sn and Mn-Si alloys – Experimental methods

2.1 Introduction

Thermoelectric properties of a given material are influenced by its crystalline structure and microstructure. Homogeneous distributions of second phases/inclusions/precipitates into a given microstructure can enhance the figure of merit of a thermoelectrical material by reducing the thermal conductivity, as soon as a specific target size of these objects is respected. It is important to analyze the possible phases that could be found in an investigated material, recognize them, and explain their influence. The phase stability and the choice of an alloy is an important issue when dealing with reactions occurring at high temperatures (like during sintering or ageing in service conditions, for examples) [64,65]. This will be topic of the first part of this chapter, where we will discuss different phases and crystalline structures of Mg-Si-Sn and Mn-Si alloys.

Afterwards, synthesis of the raw powders by mechanical alloying, with a planetary ball mill, will be presented hereafter in parallel to a literature survey on the topic. We focused on explaining the method and its advantages. Then, experimental parameters we used to obtain stable Mg-Si-Sn and Mn-Si powders are exposed together with problems encountered and solutions we offered to solve them.

After successful manufacturing the powders by mechanical alloying, consolidation by spark plasma sintering (SPS) will be presented and coupled to a literature survey on the topic applied to thermoelectrical materials. We will explain the different steps of sintering and important experimental parameters to control which helped us in determining the best sintering conditions for creating dense and intact pellets.

Fully dense pellets obtained after sintering are then adequately cut for characterization. To calculate the ZT parameter of a given material in a temperature range, it is necessary to accurately measure its elemental thermoelectric properties at different temperatures [66]. We will explain how electrical conductivity, Seebeck coefficient and thermal conductivity were measured in function of temperature. This applies also for the carrier concentration and the carrier mobility measurements at room temperature.

For powdered or sintered materials, we used different tools to characterize the microstructure at a fine scale. We will present all the kinds of equipment used, how the samples were prepared for such analyses and the methods applied to obtain quantitative results for key parameters when needed (average grain size of the sintered materials, chemical compositions of different phases dispersed in the sintered microstructure, for example).

2.2 Phase diagrams and crystalline structures

2.2.1 Mg-Si-Sn system

2.2.1.1 Phase separation of $Mg_2Si_{1-x}Sn_x$

First binary phase diagram of the system magnesium-silicide/magnesium-stanide (Mg_2Si-Mg_2Sn) was given by Muntyanu et al. in 1966 [67]. Magnesium, silicon, and tin were mixed stoichiometrically and mixtures of $Mg_2Si_{1-x}Sn_x$ (x = 0.0, 0.1, …, 1.0) were heated in an alumina crucible in air up to the melting point of Mg_2Si (1102°C) and held at that temperature for 3 hours. Cooling rate was 10-15 °C/min, and in this step a peritectic reactions occurred at 860°C (figure 2.1). Muntyanu concluded that the system has solid solubility for x < 0.08 and x > 0.62 at room temperature which corresponds to $Mg_2Si_{0.92}Sn_{0.08}$ and $Mg_2Si_{0.38}Sn_{0.62}$ compositions, respectively. He also explained that the solid solubility is temperature dependent because the system shows solid solubility at x < 0.13 and x > 0.6 at 600°C.

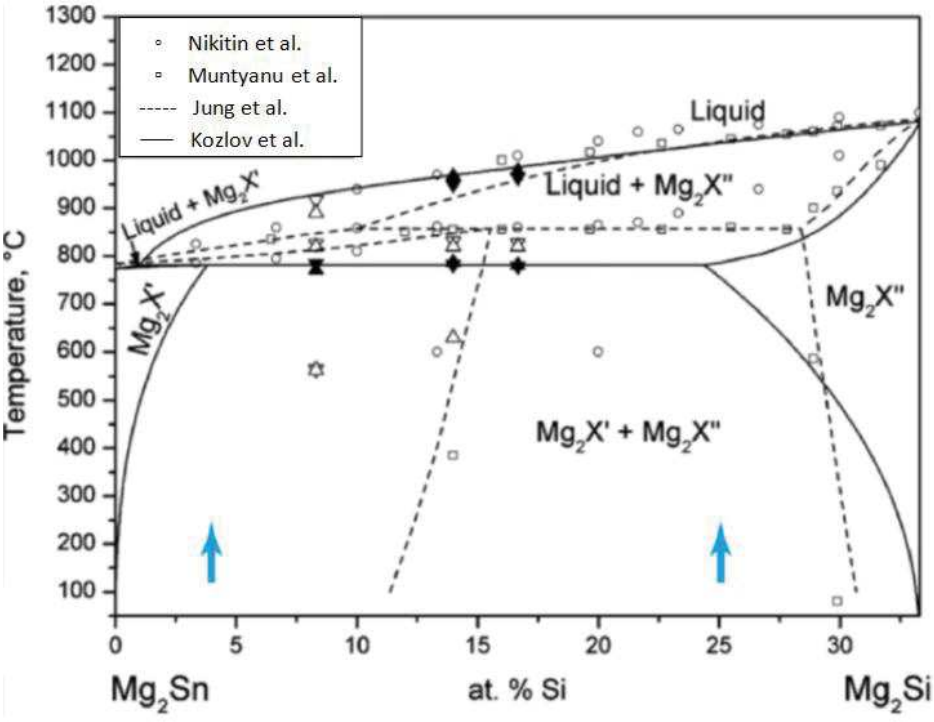

Figure 2.1: *Binary Mg_2Si-Mg_2Sn phase diagram as it was reported by Muntyanu et al.* [67]*, Nikitin et al.* [68]*, Jung et al.* [69]*, and Kozlov et al.* [70] *(figure adapted from* [70]*).*

Nikitin et al. [68] constructed a second phase diagram (figure 2.1) where they used the same stoichiometric amounts as Muntyanu [67]. The mixtures were melted in closed alumina crucibles in an argon atmosphere. To avoid the separation of phases due to different densities,

mixtures were kept in liquid state, vibrating for two hours. Cooling rate was 1.5 °C/min and mixture was annealed at a temperature of ~760°C (just below the solidus temperature) for 500h. Peritectic reaction occurred at 860 °C, as it was previously reported by Muntyanu [67]. The solid miscibility gap for $Mg_2Si_{1-x}Sn_x$ ranges from x=0.4 to x=0.6 at temperatures below 860°C. Results differ from the ones of Munyanu due to longer annealing times and slower cooling rate.

For calculation purposes, the most favorable phase diagram was given by Jung et al. [69] who used thermodynamic modeling. Jung et al. [69] showed a larger solid immiscibility range than it was previously reported by Nikitin and Muntyanu and explained that wider miscibility gap is closer to thermodynamic equilibrium (figure 2.1).

Another phase diagram of $Mg_2Si_{1-x}Sn_x$ was given by Kozlov et al. [70] (figure 2.1). They stoichiometrically mixed (x=0.5, 0.58, and 0.75) and pressed the elements into pellets and heated them in a tantalum tube under argon atmosphere. The heating rate was kept at 10°C/min, until 1300°C was reached, where the pellets were kept for 15 minutes on that temperature. Afterwards, pellets were cooled down with a cooling rate of 10°C/min. A large miscibility gap was discovered with a peritectic temperature of 781.5°C.

Then, according to the different results exposed above, it is concluded that the real Mg_2Si-Mg_2Sn phase diagram is not perfectly known at that time because the exact position of the miscibility gap is not kown, as it is also the case for the real peritectic temperature.

2.2.1.2 Structure of Mg-Si-Sn

$Mg_2Si_{1-x}Sn_x$ is an alloy that has an anti-fluorite structure as sketched on Figure 2.2. Crystal structure of $Mg_2Si_{1-x}Sn_x$ is a face centered cubic lattice (*fcc*) with a basis consisting of a $Si_{1-x}Sn_x$ atom on position 000, a Mg atom on ¼ ¼ ¼ and another Mg atom on -¼ -¼ -¼. The unit cell is a cube with Si or Sn atoms randomly distributed on the corners and faces, and Mg atoms in the tetrahedral interstices.

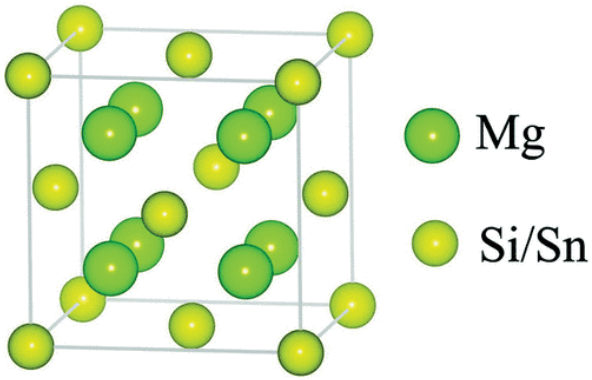

Figure 2.2: *Structure of a unit cell with anti-fluorite structure. Si and Sn atoms are randomly distributed on the corners and faces of the cube and all tetrahedral holes are filled with an Mg atom.*

As $Mg_2Si_{1-x}Sn_x$ is a system based on two phases (Mg_2Si and Mg_2Sn), the lattice parameter varies in between them linearly. The lattice parameter of Mg_2Si is 6.3512 Å (JCPDS reference file 00-035-0773), and of Mg_2Sn is 6.7630 Å (JCPDS reference file 00-007-0274).

There is a relation between the crystal lattice parameter of an alloy and the concentration of the constituent elements (phases). This relation is named Vegard's law (relation 2.1). For $Mg_2Si_{1-x}Sn_x$, we can calculate the lattice parameter with the expression:

$$a(x) = xa_{(Mg_2Sn)} + (1-x)a_{(Mg_2Si)} \qquad 2.1$$

where $a(x)$ is a lattice parameter of the alloy of interest, x is the mole fraction of Mg_2Sn, $a_{(Mg_2Sn)}$ is the lattice parameter of Mg_2Sn, and $a_{(Mg_2Si)}$is the lattice parameter of Mg_2Si. According to Nikitin et al. [68], there is no solid solution of $Mg_2Si_{1-x}Sn_x$ in the region 0.4<x<0.6, while Vegard's law is practically valid in all regions of the solid solution existence in the quasi-binary Mg_2Si-Mg_2Sn system (figure 2.3).

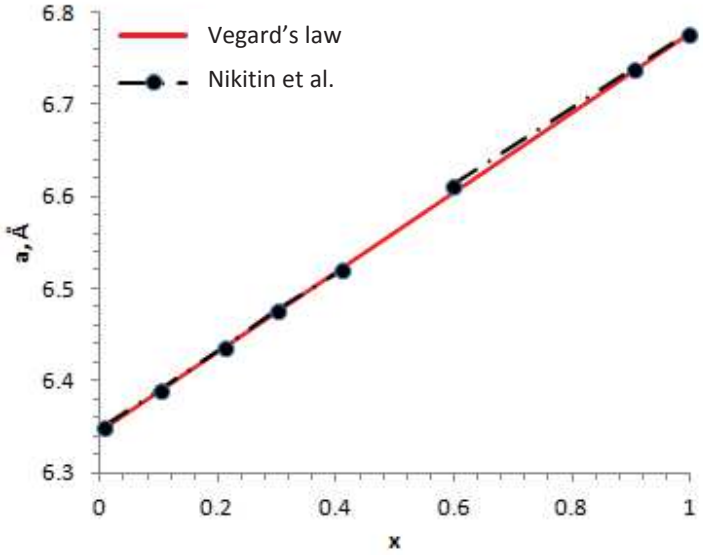

Figure 2.3: *Curve of lattice constant vs. the mole fraction x for $Mg_2Si_{1-x}Sn_x$ solid solution (adapted from Nikitin et al.* [68] *and Rowe* [71]*).*

2.2.2 Mn-Si system

2.2.2.1 Phase diagram of Mn-Si

Most complete literature review of the Mn-Si system before 1990 was reported by Gokhale and Abbaschian [72]. They established the stable phases on the Mn-Si equilibrium diagram (figure 2.4):

- Liquid: L,
- four terminal solid solutions of Mn allotropes: α-Mn, β-Mn, γ-Mn, and δ-Mn;
- intermediate phases: Mn_6Si, Mn_9Si_2, Mn_3Si, Mn_5Si_2, MnSi, Mn_5Si_3, and $MnSi_{1.75-x}$.

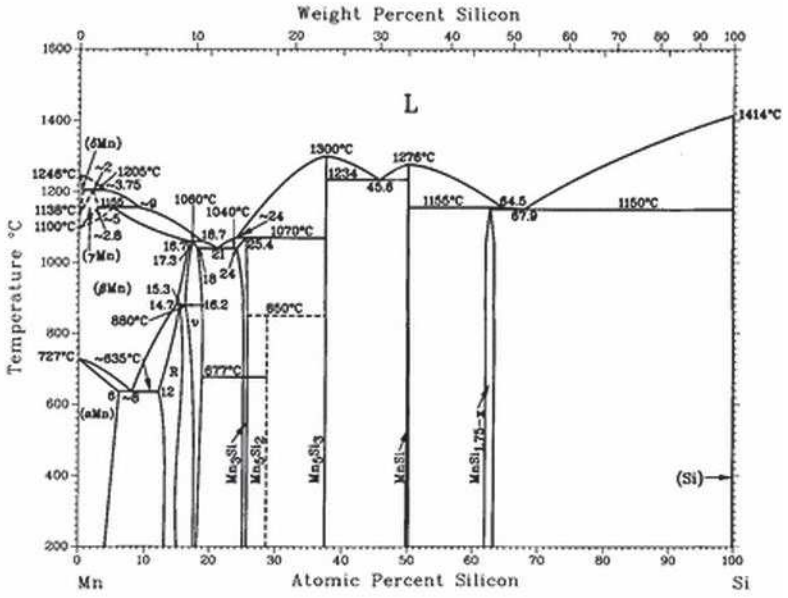

Figure 2.4: *Assessed Mn-Si phase diagram (adopted from A.B. Gokhale* [72]*).*

The higher manganese silicide (HMS) materials are the one that belong to the $MnSi_{1.75-x}$ domain, as designated by Gokhale and Abbaschian [72] HMS are found in the homogeneity range of 35-38 at. % Si and they form peritectically at 1155 °C. Single phase HMS materials are inherently difficult to obtain because the existence domain is very narrow. Most of the time, residual Si or MnSi phases are also present, depending on how the materials are fabricated in respect to the equilibrium lines shown on figure 2.4. In practice and for thermoelectrical applications it is more interesting to have residual Si as a second phase because it acts as a semiconductor. This is not the case for MnSi which adopts a typical metallic behavior.

2.2.2.2 Structure of Mn-Si – Higher manganese silicides (HMS)

HMS has a Nowotny chimney ladder structure (NCL) which is a particular intermetallic crystal structure as explained by Higgins [73]. NCL is a tetragonal phase composed of two separate sublattices. Sketch of NCL structure is given in figure 2.5, where manganese atoms (red) are placed as a tetragonal array and silicon atoms (blue) are positioned within the array. Manganese atoms form a "chimney" with helical zigzag chain. Silicon forms a ladder spiraling around the manganese helix.

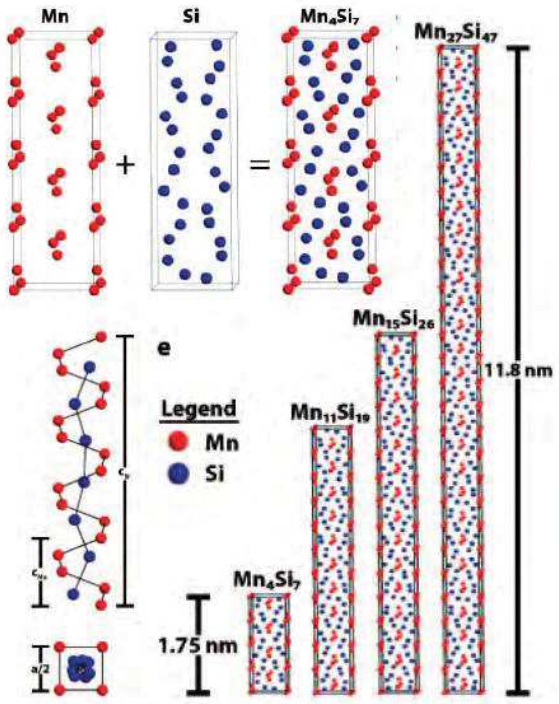

Figure 2.5: *Unit cell of HMS with different position of Mn and Si atoms, as well as different compositions and the difference in c lattice parameter (adopted from* [73]*).*

Translation symmetry of a silicon atom position in the direction of the c-axis, changes for the different HMS phases that have been discovered. As the tetragonal structure stays the same, the lattice parameter *a* (where *a* = 5.5250 Å (JCPDS reference file 00-020-0724) is the same for all HMS, while the c-axis changes. More precisely, distances between manganese layers are constant, but the distances between silicon layers are related to the chemical phase composition and are greater than those between manganese layers. Thusly, there is a mismatch between Mn and Si layers, resulting in formation of lattice with *c* parameter that is different

than the *c* parameter in Mn cell. Shin et al. [74] published how lattice parameters change with the change of HMS stoichiometry, as presented in the table 2.1.

HMS/lattice parameter	$Mn_{11}Si_{19}$ ($MnSi_{1.72}$)	$Mn_{15}Si_{26}$ ($MnSi_{1.73}$)	$Mn_{27}Si_{47}$ ($MnSi_{1.74}$)	Mn_4Si_7 ($MnSi_{1.75}$)
a (nm)	0.5518	0.5531	0.553	0.5525
c (nm)	4.8136	6.5311	11.79	1.7436

Table 2.1: *Lattice constants of the different HMS phases (adapted from* [74]*).*

2.2.3 Band gaps of $Mg_2Si_{1-x}Sn_x$ and HMS alloys

Energy gap varies between the different semiconductors and most of the values lie between 0.1 and 6.2 eV [75]. Decrease of band gap improves electrical conductivity and also induces an exponential increase in charge carrier concentration. It was theoretically calculated that Mg_2Si-Mg_2Sn has an anti-fluorite type structure with a band gap of 0.51 eV for $Mg_2Si_{0.6}Sn_{0.4}$, 0.77 eV for Mg_2Si, and 0.35 eV for Mg_2Sn [76,37].

Small doping of N-type $Mg_2Si_{1-x}Sn_x$ with Sb showed an enhancement of minority carriers at around 500 °C, which limits further increase of Seebeck coefficient and reduction of thermal conductivity [49].

Manganese silicide composition of MnSi (monosilicide) shows metallic behavior, while higher manganese silicides (HMS) with composition $MnSi_{2-x}$ ($0.25 \leq x \leq 0.28$) are a p-type degenerated semiconductor where hole concentration increases with the increase of x [77]. Depending on the HMS compositions, band gap has been calculated to be around 0.7 eV by Migas [78]. Experimentally, band gap was measured to be 0.4 eV [77,79,80]. This difference is most probably due to stacking faults which are common for NCL structure, where unit cells are rotated by 90 °C around the z axis [78].

2.3 Mechanical alloying

2.3.1 Introduction to basic principles of mechanical alloying

Mechanical alloying (MA) is a powder processing technique. MA allows the production of homogeneous materials by mixing of precursor elements. This technique was developed by John Benjamin in 1966 at the Paul D. Merica Research Laboratory of the International Nickel Company (INCO) in the USA. In the last 20 years, there is an increase of interest for the MA technique. It offers many features such as [81]:

- The production of fine dispersion of second phase particles devoted to be incorporated in a composite material;
- Reduction of grain size to nanometer size in sintered materials;
- Expanding the limits of solid solubility;
- Creation of new crystalline and quasi-crystalline phases;
- Enables the alloying of elements that could not be alloyed with other techniques;
- Allows chemical reactions to occur at low temperatures;
- Enables manufacturing to be scaled up from standard production methods as a complementary step to refine the materials before sintering (melt-spinning, Czochralski process, Bridgman technique, low-temperature growth process, etc.).

Mechanical alloying is a technique that uses a high-energy ball mill to produce an alloyed powder by solid-state reactions. MA occurs through a repeated process of fracturing and cold welding of powder particles which are caught in between two or more milling mediums (balls) as seen on figure 2.6.

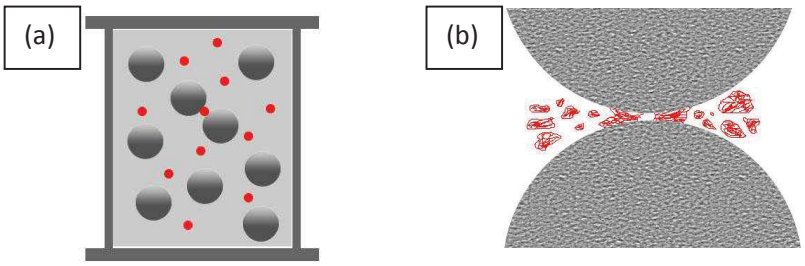

Figure 2.6: *a) Powder and ball interaction, b) ball-powder-ball collisions during mechanical alloying.*

Temperature during mechanical alloying by ball milling is around 100°C at a macroscopic scale. The friction between the balls and material locally increases the temperature of the alloy at a microscopic scale which increases the diffusion of the constituents.

Suryanarayana [82] explained that different parameters help in controlling the microstructure, the morphology, the crystallinity and the synthesis of the desired material phases. They are:

- Type of the mill: different mills have different capacities and energies;
- Size of the milling media: energy of milling is increased proportionally with the size of the milling medium (mainly balls);

- Ball to powder ratio (BPR): this is an important parameter that also scales with the milling time. Mass of the milling medium (balls) is compared to the mass of the milling powder, and the higher the number, the more energy will be introduced into the process. To achieve alloying, BPR should be between 10 and 30. Never above 30;
- Milling speed: with the increase of milling speed, the speed of balls in the jar is increased. It is necessary to find the optimum speed to achieve good alloying;
- Milling time: it depends on the BPR, the milling speed, and the temperature that develops during milling;
- Different atmosphere can be used (argon, air, helium, and vacuum). Choice of the atmosphere must not influence the chemical composition of the milled alloy;
- Process control agent (PCA): different types of agents (alkanes, for example) are introduced during milling to allow alloying for certain materials and reduce the effects of agglomeration;
- Milling vial (jar): requires having enough free volume to successfully perform the alloying. Maximum half of the volume of the milling vial can be filled (including milling medium, powder, PCA).

Depending on milling time, as well as the introduced energy level, we can expect to obtain a crystalline structure, or we can completely obtain an amorphous material. Depending on the material, PCA, and conditions of the milling, the temperature can increase greatly which improves the diffusion of species and homogenization of the composition. To obtain a perfect alloy, different conditions should be tested by typically changing the energy introduced to the process during a certain period of time.

2.3.2 State-of-art and our approach for mechanical alloying

2.3.2.1 Mg-Si-Sn

The solid-state synthesis via mechanical alloying stands on the severe plastic flow of constituents prior to solid-state reaction. In Mg-Si-Sn system, silicon is a typical brittle element with high melting temperature, without ductility and with low diffusion coefficient in magnesium and tin. Additionally, magnesium and tin are typical ductile constituents with much lower melting points. The solid-state reactivity is thought to be driven by the ductile deformation of magnesium and tin particles. During the mechanical alloying, the brittle phase (silicon) is fractured, while ductile phases of magnesium and tin have their particles firstly elongated and then fractured. This refinement happens early in the MA process, and particles of Mg and Sn plastically deform together [83].

You et al. [84] wanted to increase the electron concentration of Mg-Si-Sn alloys by adding more Mg and Sb, so they focused on creating $Mg_{2+x}Si_{0.7}Sn_{0.3}Sb_m$ (x = 0.1, 0.2; m = 0.01)

solid solutions. They used steel milling media (balls of 5 mm) and a steel vial (parameters given on table 2.2) to perform MA under argon from raw elements. XRD patterns of solid solutions corresponded to the targeted stoichiometry, but a high amount of second phase was also detected to the left side of the main alloy peaks. Large shoulders were observed, which is most likely due to a tin rich Mg-Si-Sn phase (also observed by Riffel [85]).

	Mill	Stoichiometry	BPR	Rotation speed (rpm)	Time of milling (h)
S. W. You et al. [84]	Planetary ball mill Pulverisette 5	$Mg_{2+x}Si_{0.7}Sn_{0.3}Sb_m$	20	300	24
M. Riffel and J. Schilz [85]	Planetary ball mill PM4000DLR	$Mg_2Si_{1-x}Sn_x$ $(0 \leq x \leq 0.4)$	n/a	300	8-150

Table 2.2: *Parameters applied for mechanical alloying of $Mg_2Si_{1-x}Sn_x$ (literature survey).*

M. Riffel and J. Schilz [85] used MA to produce $Mg_2Si_{1-x}Sn_x$ $(0 \leq x \leq 0.4)$ alloys in a 500 ml steel vial under argon atmosphere, with 100 (10 mm) steel balls, with 150 ml addition of n-hexane, but encountered a problem. A second phase of Mg_2Sn (or Mg-Si-Sn phase with large amounts of tin) was spontaneously created. Parameters of mechanical alloying were given in table 2.2. Their conclusion was that the good composition of $Mg_2Si_{0.6}Sn_{0.4}$ can be obtained if the milling lasts for 130 hours. They didn't use any dopants.

Mechanical alloying is an accurate manufacturing process (targeted stoichiometry is achievable), with a major advantage of high yield production capabilities for ball milling equipments (from several grams to tens of kilograms [82]), without wasting significant amounts of raw materials. Nonetheless this powder manufacturing method has been poorly investigated for Mg-Si-Sn thermoelectrical materials, especially for two reasons. Firstly, all investigators [84,85] used steel balls and vial, which introduced Fe contamination in the raw powder and in the sintered materials fabricated after. Then, thermoelectrical properties are disturbed and large iron-based defects may form. Moreover, such defects may have a detrimental influence on the mechanical/thermomechanical properties of the sintered material. Secondly, the non-optimized mechanical-alloying conditions used by the different investigators [84,85] lead also to the formation of bi-phasic materials. Then researchers of the thermoelectrical community working on the Mg-Si-Sn alloys changed their focus from MA towards the melting techniques for elaborating their materials.

2.3.2.2 HMS

Higher manganese silicides are generally prepared by melting [86], crystal growth [87] [88], chemical reaction [89], powder metallurgy (mechanical alloying belongs to this manufacturing processes category) [51], thin film processes [90] and so forth.

Highest thermoelectrical properties were found for $MnSi_{1.75}$ as it was published by Zamanipour et al. [49]. They mechanically alloyed three types of higher manganese silicides: $MnSi_{1.73}$, $MnSi_{1.75}$, and $MnSi_{1.77}$. $MnSi_{1.75}$ had the lowest thermal conductivity (2-2.7 W/m K in the temperature range of 450-650°C) of all three, while $MnSi_{1.77}$ composition had the highest Seebeck coefficient, and $MnSi_{1.73}$ the highest electrical conductivity (nearly 10% larger than the other two compositions). Parameters of mechanical alloying are resumed in table 2.3.

Zamanipour et al. [49] used tungsten carbide balls and vial (parameters given in table 2.3). Zamanipour reported that the intensity of XRD peaks of Mn and Si decrease with time while HMS peaks grow. After 12 hours of mechanical alloying the peaks of constituents Mn and Si completely disappeared. MnSi phase was present until 16 hours of milling and decreased after 80 hours of milling.

Lee et al. [91] mechanically alloyed a $MnSi_{1.73}$ solid solution (conditions are given in table 2.3). They observed a single phase of $MnSi_{1.73}$ forming after 24 hours of milling. No amorphous phase was observed during milling, but broadening of peaks during XRD analysis was noticed due to the particle refinement. Particle size continued to decrease as milling continued.

Itoh et al. [86] synthesized $MnSi_{1.73}$ compound by mechanical alloying, in a zirconia milling vial, with zirconia balls (experimental conditions resumed on table 2.3). They created three separate batches where the batch A was milled at 200 rpm for 10 hours, batch B at 400 rpm for 1 hour and batch C at 400 rpm for 10 hours. XRD patterns show that batch A did not have the desired $MnSi_{1.73}$ phase, while the other two did, without many differences between them.

	Mill	Stoichiometry	BPR	Rotation speed (rpm)	Time of milling (h)
Lee et al. [91]	SPEX (8000D)	$MnSi_{1.73}$	10	1750	24
Itoh [86]	Planetary mill (P-6, Fritsch)	$MnSi_{1.73}$	20	200/400	10/1
Zhou et al. [92]	Planetary mill	$MnSi_{1.75}$	10	300	12
Shin et al. [74]	Planetary mill (P-5, Fritsch)	$MnSi_{1.72-1.75}$	10	300-400	3-48
Zamanipour et al. [49]	Planteray Mill (P6/P7, Fritsch)	$MnSi_{1.7x}$ (x=3,5,7)	5	500 and 1000	50

Table 2.3: *Parameters applied for mechanical alloying of HMS (literature survey) in argon atmosphere.*

Zhou et al. [92] ball milled an ingot with a $MnSi_{1.75}$ composition firstly made by induction melting. $MnSi_{1.75}$ was milled for 30 minutes to get micropowder and 810 minutes for nanopowders (conditions given in table 2.3). SEM observation showed that micropowder had large particles of few micrometers, whereas nanopowder particles were within tens of nanometers (an average size of 26 nm was calculated).

Shin et al [74] synthesized $MnSi_{1.72-1.75}$ by mechanical alloying with steel balls (5 mm diameter) and hardened-steel vial in argon (conditions are summarized in table 2.3). Shin realized that $MnSi_{1.73}$ powders, when mechanically alloyed at 300 rpm for 12h, have a large amount of un-reacted Mn and Si. Additionally, after 48h of milling at 300 rpm, HMS phases ($MnSi_{1.72-1.75}$) created together with a large amount of MnSi phase. Shin et al. decided to increase the milling energy by setting rotation speed to 400 rpm and HMS ($MnSi_{1.72-1.75}$) was synthesized after 3h of MA, while after 12h, MnSi phase was also noticed. They concluded that MnSi creation contributes to reduce the free energy of the system during ball milling, because MnSi is thermodynamically more stable than pure phase of HMS ($MnSi_{1.72-1.75}$) . Shin reported that to create good HMS, mechanical alloying should have high rotation speed and short time of milling.

Mechanically alloyed Mn-Si alloys proved to be difficult to form without the MnSi phase which should be inhibited at all times. Indeed, MnSi phase is a metallic phase which greatly deteriorates the thermoelectric properties since it changes the nature of the HMS and making them to act like a conductor (instead like a semiconductor). There are two different approaches for eliminating the MnSi phase presence in HMS as given D.K Shin et al. [74] and Z Zamanipour

et al. [49]. Shin proposed a ball milling speed during a short time, while Zamanipour proposed a much longer time of milling (over 80 hours).

2.3.3 Experimental procedure used for our investigations

For the purpose of mechanical alloying and avoiding contamination by oxygen/humidity, we used a glove box filled with argon (T11-T12 model, Jacomex). Raw materials used in this thesis (Mg, Si, Sn, Sb, B, Ge, and Mn) were kept all the time under an inert atmosphere (argon) and their details can be seen in the table 2.4. To avoid the spoiling of the precursors, humidity and oxygen levels were kept at 0 ppm in the glove box.

Precursors	Mg	Si	Sn	Sb	Mn	B
Purity (%)	99.98	99.999	99.8	99.999	99.9	97
Form	Chips	Powder	Powder	Powder	Powder	Powder
Size (μm)	350	60	45	74	200	74

Table 2.4*: Nature of the precursors.*

Mechanical alloying is performed in a milling container (vial or jar) with milling medium (balls). In the literature, stainless steel was used [85], which has a big drawback as it pollutes the milled powder. Chosen material for this thesis is zirconia. It is a hard material with a high density of 6.1 g/cm^3.

To create a homogeneous matrix of $Mg_2Si_{0.4}Sn_{0.6}$ the raw elements were added into the jar (500 ml) together with zirconia balls (10 mm diameter), and the exact value of masses of each element (25 gram in total), as it can be seen on table 2.5.

	Mg	Si	Sn	Sb	B
$Mg_2Si_{0.3875}Sn_{0.6}Sb_{0.0125}$	9.1897	2.0574	13.4652	0.2877	/
$Mg_2Si_{0.38}Sn_{0.6}B_{0.02}$	9.2963	2.0410	13.6214	/	0.0414

Table 2.5: *Synthesized Mg-Si-Sn alloys by MA and the masses put into the 500 ml jar (g).*

Raw materials used to create Mn-Si alloys were placed in a smaller jar of 250 ml and targeted stoichiometry and masses of raw elements (total of 8 grams of materials was put in the jar) can be seen on table 2.6.

	Mn	Si
$MnSi_{1.75}$	4.2454	3.7546

Table 2.6: *Synthesized Mn-Si alloys by MA and the masses put into the 250 ml jar (g).*

Keeping BPR value above 10, allows mechanical alloying to happen. Keeping it below 1 will enable grinding (particle size reduction) without any alloying process. In table 2.7, the different milling containers and BPR used are presented.

	Balls number	Mass of M.M.	Mass of powder	BPR
250ml	70	210	8	26.25
500ml	200	600	25	24

Table 2.7: *Two types of jars with corresponding BPR.*

The precursors are put in the jar, under argon atmosphere of the glove box, all together with a processing aid (cyclohexane). Jar was secured with an adhesive tape and with a steel ring. This prevents the opening of the jar during the high energy ball milling. Secured jar is placed in the planetary mill. Milling parameters are as described in table 2.8, and the milling was done on a planetary ball mill presented on the Figure 2.7.

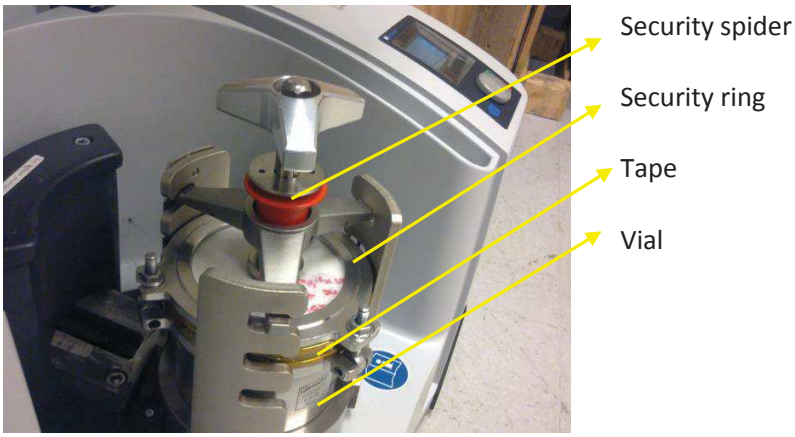

Figure 2.7: *Planetary ball mill – RETSCH PM200.*

Duration (h)	Speed of rotation (rpm)	Interval (min)	Pause (min)
60	300	10	2

Table 2.8: *Conditions of mechanical alloying.*

Interval in table 2.8 corresponds to the duration of milling in one direction. The interval is followed by a pause of 2 minutes. This pause avoids massive temperature build ups that can cause the creation different unwanted phases and is also useful to preserve the integrity of the planetary ball mill. New interval starts after the pause for 10 minutes, but in the opposite rotating direction.

When mechanical alloying is completed, powder is extracted from the jar in the glove box with 0.0 ppm of oxygen and humidity. This step is important as oxygen can react with the alloyed material to form oxide-based compounds. Increase of humidity and oxygen levels in the raw powder can also lead to problems in the next step that is sintering. It was especially noticed, that a humidity level of 2.4 ppm causes the sintering of $Mg_2Si_{0.4}Sn_{0.6}$ to fail and broken samples were obtained at the end. The exact problems encountered and solutions for a proper mechanical alloying step are described in the next section.

2.3.4 Problems and solutions for mechanically alloying of $Mg_2Si_{0.4}Sn_{0.6}$ and smaller difficulties for the HMS formulation

There were two types of problems noticed when we mechanically alloyed the $Mg_2Si_{0.4}Sn_{0.6}$ generic compounds. The first one was dealing with a slightly higher amount of humidity in the glove box, which resulted in a failed mechanical alloying process (the tailored phase composition is not obtained at the end). On figure 2.8, the difference is shown between a well alloyed powder (figure 2.8a) and the powder processed with a too high level (H_2O levels = 2.4 ppm) of humidity (figure 2.8b). The latter shows that magnesium did not react with silicon and tin. Chips of Mg_2Sn were also noticed as a residue in the vial. Reducing H_2O to 0.0 ppm solved this problem.

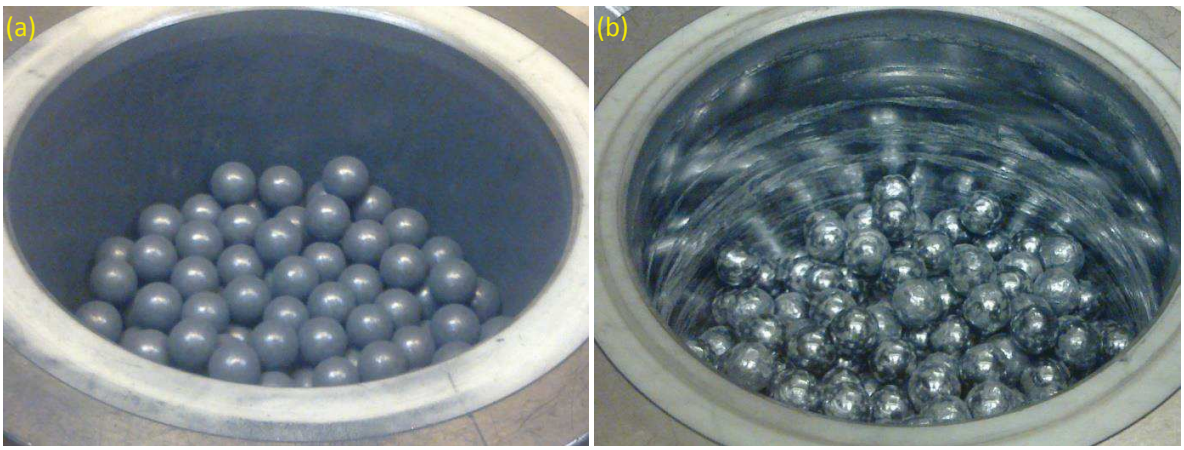

Figure 2.8: *(a) successful mechanical alloying; (b) Milling with high humidity (H_2O).*

Second problem was exactly the same as described by Riffel [85] if we did not used a process control agent (PCA) for mechanical alloying. Riffel described the formation of a tin-rich second phase along side with $Mg_2Si_{1-x}Sn_x$ phase which we also noticed (figure 2.9b). Then, we used cyclohexane as a PCA to eliminate the unwanted second phase as it can be seen on figure 2.9a. The PCA in this case inhibits agglomeration and cold welding by reducing the surface tension of the particles. Mechanical alloying without PCA was giving yield, for 500 ml jar, around 4.5 grams out of 25 grams that was introduced in raw precursors (18% yield). By adding 1 wt% of PCA of cyclohexane, in respect to the powder weight, the yield has increased to 17 grams (68% yield). A tiny amount of residue was still noticed at the bottom of the vial with Mg_2Sn composition, but the thermoelectric properties were vastly improved in the sintered material. Adding 3 wt% of cyclohexane, in respect to the powder weight, completely removed the residue from the bottom of the jar and the yield was increased to 22 g (88% yield). The rest of the

powder (12%) was present in the jar and on the balls, but it was hard to extract all of it with a spatula.

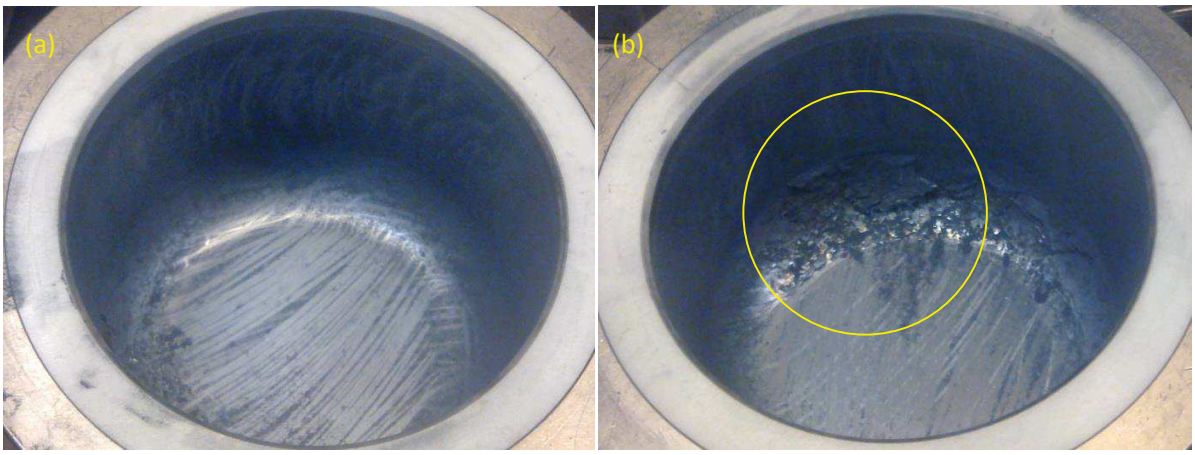

Figure 2.9: *(a) successful MA (b) Tin rich Mg-Si-Sn residue at the bottom of the jar versus.*

Mechanical alloying of HMS was done in a smaller jar (250 ml). We added 1 wt. % (of the total powder weight) of cyclohexane as PCA. We followed the guidance given by Z. Zamanipour et al. [49], where a long duration of milling is applied to eliminate the presence of the parasitic MnSi phase. With a milling speed set to 300 rpm, we shorten the successful milling time to 60 hours instead of 80 [49]. We encountered no problem with the collection of the powders, and the yield was around 94%.

2.4 Sintering

2.4.1 Introduction

Sintering is a processing technique used to produce density-controlled materials and components from metal, alloy or ceramic powders by applying thermal energy. Basically, sintering processes can be divided into two types: solid-state sintering and liquid-phase sintering. Solid-state sintering occurs when the powder compact is densified wholly in a solid state at the sintering temperature, while liquid-phase sintering occurs when a liquid phase is present in the powder compact during sintering.

The driving force for sintering is the reduction of the total interfacial energy. The total interfacial energy of a powder compact is expressed as γA, where γ is the specific surface energy and A the total surface area of the compact. The reduction of the total energy can be expressed as $\Delta(\gamma A) = A\Delta\gamma + \gamma\Delta A$. Here, the change in interfacial energy $(\Delta\gamma)$ is due to

densification and the change in interfacial area (ΔA) is due to grain coarsening, also named grain growth. For solid-state sintering, $(\Delta\gamma)$ is related to the replacement of solid/vapor interfaces (surfaces) by solid/solid interfaces (grain boundaries). Then, during sintering, the reduction in total interfacial energy occurs via densification and grain growth that are indeed two competing mechanisms.

In the early stage of solid-state sintering, necks form between the elemental particles constituting the starting powder in the green state. In that case, samples are consolidating without volume change or shrinkage. This step, named consolidation, can be simply simulated by investigating mater transport between the surface of two tangent spheres, representing two elemental crystallites, and the surface of the forming bridge. In that case, mater displacement proceeds either by surface diffusion, gas phase transport or bulk (said also volume) diffusion in the grains.

When the samples begin to shrink, it signifies that the residual porosity is now removed. This subsequent step is named densification. A simple way to simulate densification consists in investigating mater transport between the center of the surface formed by two intersecting spheres (grain boundary), still representing the two elemental crystallites, and the surface of the forming bridge. In that case, mater displacement proceeds either by grain boundary diffusion or bulk diffusion in the grains.

As stated earlier, during sintering, grain growth is also active to reduce the total interfacial energy. When grain boundaries and pores have a simultaneous displacement (a pore is always attached to a grain boundary), the grain growth is controlled either by the grain boundaries or by the pores. If the grain growth is controlled by grain boundaries, it means that the pore dragging effect on the grain boundaries motion is negligible. If the grain growth is controlled by pores, it means that the displacement rate of a pore / grain boundary ensemble is fixed by the displacement rate of the pore. When the grain growth is controlled by grain boundaries, the mater displacement invoked is the atomic migration from one grain toward another grain through the separating grain boundary. In the case of grain growth controlled by pores, mater displacement proceeds either by surface diffusion at the pore surface, gas phase transport in the pore or bulk diffusion in the grains.

The major variables which determine sinterability and the sintered microstructure of a powder compact may be divided into two categories: material variables and process variables (table 2.9).

Variables related to raw materials (materials variables)	*Powder:* Shape, size, size distribution, agglomeration, mixedness etc… *Chemistry:* Composition, impurities, non-stoichiometry, homogeneity etc…
Variables related to sintering conditions (process variables)	Temperature, time, pressure, atmosphere, heating and cooling rates etc…

Table 2.9: V*ariables affecting sinterability and microstructure*.

The variables related to raw materials include chemical composition of powder compact, powder size, powder shape, powder size distribution, degree of agglomeration etc… These variables influence the powder compressibility and sinterability b(densification and grain growth). In particular, for compacts containing more than two kinds of powders, the homogeneity of the powder mixture is of prime importance. To improve the homogeneity, not only mechanical milling but also chemical processing, such as sol-gel and coprecipitation processes, have been investigated and utilized. The other variables involved in sintering are mostly thermodynamic variables, such as temperature, time, atmosphere, pressure (uniaxial or isostatic), heating and cooling rates. Many previous studies have examined the effects of sintering temperature and time on sinterability of powder compacts. It appears, however, that in real processing, the effects of sintering atmosphere and pressure are more complicated and important. Unconventional processes (spark plasma sintering, flash sintering…) controlling these variables have also been intensively studied and developed.

2.4.2 Spark Plasma Sintering (SPS)

Spark plasma sintering (SPS) is a part of resistive sintering processes [93,94,95]. The SPS is a sintering method of densification of powders, involving simultaneous application of uniaxial compressive force [96] and an electrical pulsed current. The electric current is supposed to go, at least partially, inside the powder compact and / or allow the temperature rise (by conduction and Joule effect) within the system of compaction (pressing die and punches). This method gives SPS attractive features such as high heating and cooling rates (up to 600 °C/min and 100 °C/min, respectively). Additionally, thermal cycles are very short (from few minutes to few tens of minutes), which is good for industrial applications.

2.4.2.1 SPS principle

This method includes the simultaneous application of an electric current (direct current (DC) or alternating current (AC), pulsed or not) and a macroscopic mechanical uniaxial pressure (constant or not – depending on the sintering cycle). The powder bed is placed in a die, and between two punches. The whole assembly is pressed between two electrodes that allow the passage of the electric current (figure 2.12). The electric current produced is generally made of DC pulses. This current passes through the punches, and may also proceed wholly or partly through the powder bed compact, according to the electrical conductivity of the material. The order of magnitude of the standard electric current used is typically between 3000 and 20 000 A, while the potential difference between the two electrodes remains equal to a few volts. The heating rates may range from a few degrees to 600 °C/min. In the case of conventional hot-pressing, for example, it takes several hours to reach the sintering temperature (15-30 °C/min maximum heating rate), while this is not the case with SPS (figure 2.12).

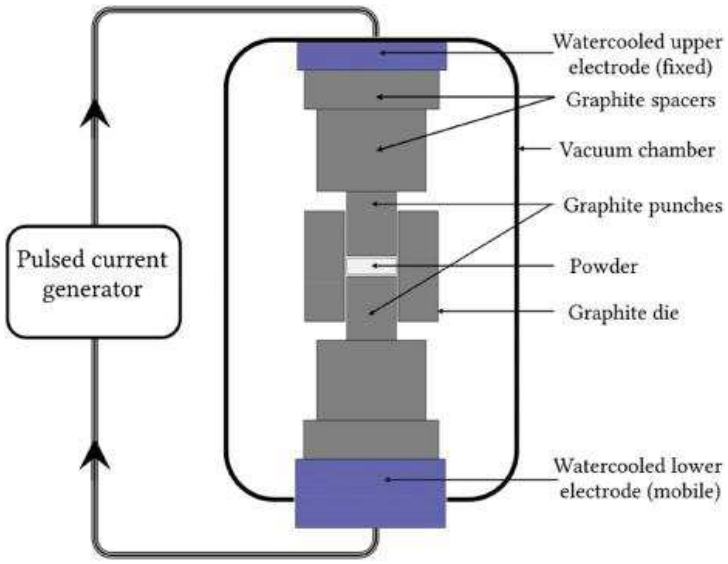

Figure 2.12: *Scheme of SPS.*

In most cases, the entire assembly of “die + punches” is made out of graphite. Thusly, the sintering temperature can go as high as 2000 °C. However, it is possible to use other systems of steel or ultra-hard carbide. If this is the case, the maximum temperature is reduced to 500 °C and 700 °C, respectively.

SPS sintering is usually performed under vacuum, but it is also possible to work under controlled atmosphere: neutral (nitrogen, argon), reduced (hydrogen) or air (in that case the die and pistons are made in another material than graphite).

2.4.2.2 Measuring of the temperature

Depending on the SPS cycle, the temperature can be measured in different ways:

1. by an optical pyrometer (through the top punches) or;
2. by a thermocouple placed in the die, close to the sample.

Between the two measurement methods, a difference of several tens of degrees can be observed. That is why it is important to specify the method of temperature measurement. Different positions for temperature measurement are shown in figure 2.13 hereafter.

2.4.2.3 Advantages of SPS

A short summary of few advantages and disadvantages of Spark Plasma Sintering (SPS) in comparison to conventional sintering is given here.

Advantages are:

- Short sintering cycles (few minutes to few tens of minutes for a cold-to-cold sintering run)
- Full densification
- Small grain size and controlled grain growth (nanomaterials can be prepared)
- Compacting and sintering steps are combined into one operation
- Sintering of all kinds of materials (metallic [97,98], ceramic [99,100,101], quasicrystalline [102], semiconductor [56], and glass [103]).

Disadvantages are:

- Limited geometrical shapes and sample size (due to thermal gradients within a sample)
- High cost for the generator of pulsed current
- Graphite contamination due to graphite tools is possible

In order to assess the SPS sintering technology, it is necessary to compare it to more conventional and therefore better known methods. The way of approaching SPS is to compare it with hot-pressing (HP).

2.4.3 State of the art - Sintering

2.4.3.1 $Mg_2Si_{1-x}Sn_x$

Song et al. [83] used bulk mechanical alloying to obtain a powder which was consolidated by hot-pressing. The pellets were obtained with a heating rate of 20°C/min and parameters as given in table 2.9. They showed that with the rise of pressure, density increases as well as thermoelectric properties (ZT value of 0.13 at 375 °C for an n-type undoped $Mg_2Si_{0.4}Sn_{0.6}$ solid solution).

Synthesis of Mg-Si-Sn was also done by Khan et al. [104] to create an n-type $Mg_2Si_{0.55-y}Sn_{0.4}Ge_{0.05}D_y$ (D - dopants Bi (y = 0.0175 and 0.02) and Sb (y = 0.0075 and 0.0125). To obtain the proper phase they did two homogenization steps before hot pressing. Composition of hot-pressed pellets was clearly heterogeneous. Spots were tin poor (but silicon rich) while others were silicon poor (but tin rich) when EDX mapping was carried out on as-sintered fracture surface. Conditions used for sintering can be seen in table 2.9.

You et al. [84] consolidated $Mg_{2+x}Si_{0.7}Sn_{0.3}Sb_m$ $(0 \leq x \leq 0.2,\ m = 0$ or $0.01)$ solid solution they obtained by MA. The parameters of sintering by hot-pressing (HP) were given in table 2.9. You [84] successfully achieved the targeted stoichiometry after hot pressing.

	Process	Pressure (MPa)	Atmosphere	Temperature (°C)	Duration (min)
Song et al. [83]	Hot-pressing	500/750/1000	Argon	800	N/A
Khan et al. [104]	Hot-pressing	80	Argon	770	N/A
You et al. [84]	Hot-pressing	70	Vacuum	600-800	2
Riffel [85]	Hot-Uniaxial press (HUP)	50	Vacuum	800-850	N/A
Liu et al. [42]	SPS	N/A	N/A	550-800	N/A

Table 2.9: *Parameters of sintering and types of sintering for $Mg_2Si_{1-x}Sn_x$ (literature survey).*

M. Riffel [85] parameters of hot-pressing were placed in the table 2.9 and reported that consolidation causes a partial decomposition of the materials that is not in accordance to published quasi-binary phase diagrams.

W. Liu et al. [42] used spark plasma sintering to consolidate Sb doped $Mg_2Si_{1-x}Sn_x$ solid solutions synthesized by two step solid state reaction (explained in chapter 1). They consolidated the powders they investigated in the temperature range 550-800 °C.

2.4.3.2 HMS

Sintering of HMS occurs at higher temperatures and investigators noticed the separation of the MnSi phase. Lee et al. [91] noticed the MnSi phase which appeared after consolidation by hot pressing (conditions given in the table 2.10). This was also reported by Itoh et al. [86] when using Pulse discharge Sintering (PDS) to consolidate their $MnSi_{1.73}$ powders (conditions in table 2.10).

	Process	Pressure (MPa)	Atmosphere	Temperature (°C)	Duration (min)
Lee et al. [91]	Hot-pressing	70	Vacuum	850	120
Itoh [86]	Pulse Discharge Sintering (PDS)	100	Vacuum	850	30
Zhou et al. [92]	Uniaxial hot pressing	100	Vacuum	900	60
Shin et al. [74]	Hot pressing	70	vacuum	700 - 850	120
Zamanipour et al. [49]	Hot pressing	108	Vacuum	950	5

Table 2.10: *Parameters of sintering and types of sintering for HMS (literature survey).*

Zhou et al. [92] hot-pressed (parameters can be seen at table 2.10) micro and nano sized powders. The sinter samples he manufactured an average grain size of 50-100 µm and 0.5-2 µm, respectively. The formation of MnSi phase started at 600°C.

Shin et al. [74] hot-pressed $MnSi_{1.72\text{-}1.75}$ powders. They confirmed what was said by Zhou et al. [92] that the MnSi phase is detected during sintering using the conditions shown in table 2.10.

Zamanipour et al. [49] reported that the melting points for $MnSi_{1.73}$, $MnSi_{1.75}$, and $MnSi_{1.77}$ are 1146, 1147, and 1149 °C, respectively. They gave no explanation to the shift of the melting temperature.

Single phase HMS is inherently difficult to form due to its peritectical nature and coexistence with residual MnSi phase. As soon as the sintering of HMS starts (which will be explained in chapter five), the MnSi phase will start to form because it is thermodynamically more stable.

2.4.4 SPS protocol adopted for our investigations

When sintering our samples with SPS method on an HPD-25 equipment (FCT Systeme GmbH), we measured the temperature data from both the pyrometer and the thermocouple. Pyrometer target area is found 4 mm from the powder bed in the upper punch, while thermocouple is found 4 mm from the edge of the powder bed (figure 2.13b). Thusly, they provide us the accurate temperature in the middle, and on the edge of the circular powder bed.

It is necessary to have a good electrical and thermal contact between different pieces of the die and the powder inserted inside. This was achieved using graphite paper (Papyex®-Mersen) which covers inside of the die. Papyex also equally absorbs strains.

Graphite die (Mersen 2340) used for sintering has an inside diameter of 20 mm, thickness of 15 mm and length of 64 mm. Punches were also made out of graphite (Mersen 2340). The graphite paper is cut so that it may fit the die.

Papyex was positioned inside the die, and first punch was inserted. The circular shaped papyex disk was positioned inside the die on the surface of the punch. Powder was placed in the glove box with 0.0 ppm of oxygen and H_2O on the paper covered surface of the punch and it was equally distributed. The second circular papyex was placed over the powder and second punch was placed inside the die. Figure 2.13a shows the papyex.

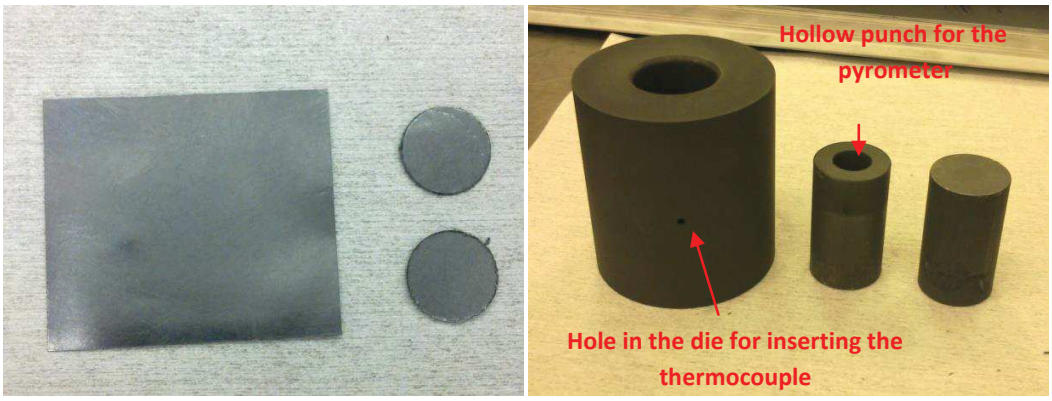

Figure 2.13: *a) Papyex graphite paper; b) graphite die with two punches (right).*

Afterwards, the die was placed in the SPS machine. The cycle used will be explained, for each material, separately in the third, fourth and fifth chapters.

Throughout the SPS sintering cycle, a sensor records the movement of the system/ sample along the compaction axis. This can be observed directly on the monitor of the equipment as the sample densifies. For each test run, the variation of the instantaneous height ΔL(>0) of the compact is measured. Due to the relative expansion of the assembly (die + punches) in the SPS, a correction must be made. This is done by subtracting the results of a blank run from the sintering cycle carried out with the powder. It is possible to calculate the

instantaneous height of the compact, $\Delta L = L_f + \Delta L_t - \Delta L$, where L_f is the final height of the sintered compact, and ΔL_t is the total variation in height recorded at the end of the sintering run (with powder). Finally, it is easy to show that the instantaneous sample height and instantaneous relative density are connected by relation:

$$D = \left(\frac{L_f}{L}\right) D_f \qquad 2.3$$

The apparent density of the sintered samples was measured using the Archimedes method in ethanol. The final relative density,D_f, was obtained using the theoretical density of the as-sintered sample.

2.5 Density measurements by Archimedes method

This is a precise method which easily calculates the apparent density of the as-sintered samples. A special kit is used for measurements (figure 2.14).

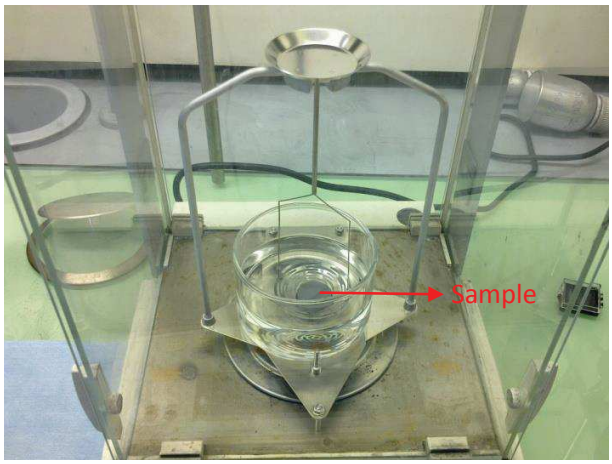

Figure 2.14: *Density measurement kit.*

The weight of the sample is measured three times (scale used is LA310s, Sartorius). First, mass is measured in air, obtaining the mass m_1. A second measure is done for the sample that is submerged into absolute ethanol, and second mass value, m_2 is measured. After that, the submerged sample is removed from the ethanol and wiped. Then, it's mass in air is measured again, obtaining the third mass value, m_3. Knowing these three masses, we can calculate the density of the material:

$$\rho_{sample} = \frac{m_{total}}{V_{total}} = \frac{m_1}{m_3 - m_2} \cdot \rho_{ethanol} \quad 2.4$$

where $\rho_{ethanol}$ represents the density of ethanol ($\rho_{ethanol} = 0.7893$ g/cm^3). It is necessary to compare the sample density with theoretical density to see if the densification process has been fully completed.

$$D(\%) = \frac{\rho_{sample}}{\rho_{theoretical}} \quad 2.5$$

Theoretical density, $\rho_{theoretical}$, was obtained from the volume of a unit cell of the alloy of interest (Mg-Si-Sn or Mn-Si) by using the lattice parameters of the unit cell. Theoretical density values for the chosen compositions in this thesis are: 5.1176 g/cm^3 for $MnSi_{1.75}$, 3.1348 g/cm^3 for $Mg_2Si_{0.3375}Ge_{0.05}Sn_{0.6}Sb_{0.0125}$, 3.0829 g/cm^3 for $Mg_2Si_{0.3875}Sn_{0.6}Sb_{0.0125}$, and 3.0475 g/cm^3 for $Mg2Si_{0.38}Sn_{0.6}B_{0.02}$.

2.6 X-ray diffraction

2.6.1 Introduction

X-ray diffraction is a technique for analyzing a wide range of materials, identifying crystalline phases and determining the parameters of the crystal structure. Measurements on the powders we synthesized and on the as-sintered samples were performed on a "BRÜKER D8 advance" device (sample holder/detector have a θ/2θ configuration). It has a copper anode ($\lambda_{K\alpha 1} = 1.54056$ Å and $\lambda_{K\alpha 2} = 1.54439$ Å) and nickel filters that allows the elimination of $K_\beta$rays.

Powders were placed in a glass holder with a hole in the middle so that the powder bed surface is in the same plane as the glass holder. Due to the glass holder, at lower angles some noise is noticed (shown in later chapters). Sintered samples are placed on the normal holder while kept in the plane of reference given on the holder. Analyses were performed in the domain of existence of most of diffraction peaks for a given formulation, which is between 20 and 80 °.

2.6.2 TOPAS and Grain size calculation

TOPAS stands for Total Pattern Analysis Solutions. XRD data of powders and as-sintered samples were analyzed by TOPAS software. It can distinct the different peaks related to the different phases, even if they overlap. The most important thing is that this software can be also

used to calculate the full width at half maximum height (FWHM) of the peaks which help us to determine the grain size using the following expression:

$$L = \frac{K\lambda}{\beta cos\theta} \tag{2.6}$$

where L is the grain size, K is a dimensionless factor that depends on the shape of the particles (we adopted K = 0.94), λ is the X-ray wavelength, β is the line broadening at half the maximum intensity (FWHM), and θ is the Bragg angle.

A more accurate method is the Williamson-Hall one [105], which takes into account the lattice strains. Then, finally, we can calculate the grain size using:

$$\beta = 4\xi tan\theta + K\lambda/Lcos\theta \tag{2.7}$$

where ξ represents the lattice microdeformations.

Software gives values of β and ξ parameters based on Gaussian or Lorentz functions for the deconvolution of left and right sides of each diffraction peak for a given diffraction angle θ. The data were computed by subtracting the XRD machine background.

2.7 SEM

A scanning electron microscope is able to produce images of a sample by scanning it with a focused beam of electrons. The electrons interact with atoms in the sample, and SEM gathers various detectable signals which give the information about the sample's surface topography and composition. Detector is catching the secondary electrons that emit from the surface of the samples. These secondary electrons form a topographic image of the surface of the sample.

The microscope we used to investigate our powders and sintered samples was a "LEO 1530VP Gemini, (LEO Elektronenmikroskopie GmbH)". It is equipped to do Energy Dispersion X-ray Spectroscopy (EDS). This method is used to investigate the chemical homogeneity of the samples.

Before SEM observations, solid samples were polished (SiC polishing paper 320, 800, 1200, 2000 mesh) and cleaned by cloth. Tools were used to break the samples. Observations were made on a freshly broken surface. In this manner, it was easy to see the grain shape, porosity levels (if any), and second phases/precipitates if they are big enough. Scanning was made with a 5 mm-6.3 mm working distance with an electron high tension (EHT) of 5kV.

Powders were placed on an adhesive graphite circular shaped tape. Due to their fast oxidation when exposed in air, this was performed few minutes before observations.

2.8 TEM

2.8.1 Sample preparation by FIB

Focused ion beam is a technique used for specific analysis, deposition, and ablation of materials. It looks like SEM, but instead of using a focused beam of electrons to make an image, FIB uses a focused beam of ions.

To investigate the microstructure of our different as-sintered sample, each one was cut from its center part put on a holder and introduced into the FIB equipment (beam of Ga). Then thin-foils, having a thicknesses ranging from 80 to 250 nm, where cut and glued onto a cupper grid (figure 2.15).

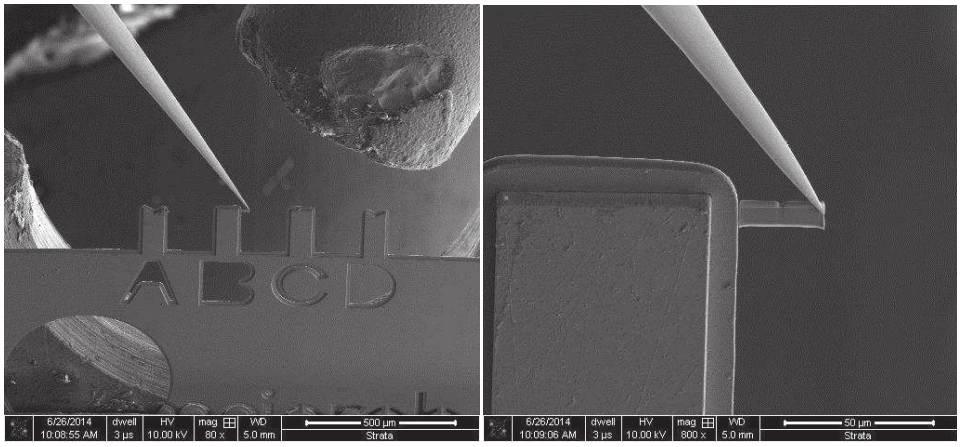

Figure 2.15: *Image of thin foil for TEM observation in FIB equipment.*

2.8.2 TEM observations

Transmission electron microscopy (TEM) is a microscopy technique in which a beam of electrons is transmitted through an ultra-thin specimen, interacting with it as it passes through. Image is formed from the interaction of the electrons transmitted with the specimen. The image is magnified and focused onto an imaging device, such as a fluorescent screen, on a layer of photographic film, or is detected by a sensor such as a CCD camera.

TEM uses the small de-Broglie wavelength of electrons and can create high resolution images.

Characterization of samples using TEM was performed on a Tecnai Osiris microscope (acceleration voltage of 200 kV, line resolution of 1.02 Å, point to point resolution of 2.5 Å). It is an analytical TEM instrument optimized for high speed and high sensitivity EDX measurements in STEM mode. With a high brightness XFEG gun, EDS maps can be acquired very fast. It has a BF (bright field), two ADF (annular dark-field imaging), and a HAADF (high angle annular dark field) detectors that provide a wide range of diffraction and Z-contrast conditions for STEM imaging and analyses. Tecnai Osiris has a 1.8 Å point to point resolution in HAADF/STEM mode.

Obtained TEM images are treated by ImageJ software to determine the average grain size of the as-sintered samples. Statistics analysis is effective on a surface of 100 to 150 grains. Apparent grain size *g*, can be explained with a sphere that has a diameter G. Using the three-dimensional correction factor of 1.2, given by G. Bernard-Granger [106], we can make an approximation of the real grain size, G:

$$G \approx 1.2g \tag{2.8}$$

For thermoelectric materials, inclusions/precipitates (second/different phases) that are coexisting with the surrounding matrix are very important as they disperse phonons and reduce the thermal conductivity. With TEM, it is possible to evaluate the volume fraction of inclusions/precipitates (*v*), when they are present in a given material, assuming that it is equal to the surface fraction (*s)* [107]. If the inclusions are spherical, then according to Delesse's equation [108] surface fraction is:

$$s = \frac{S_i}{S_t} \approx v \tag{2.9}$$

where S_i is the total area where inclusions are present (sum of all precipitate/nodular surfaces) and S_t represents the total area of the images that is being analyzed at the same magnification.

Quantification of the chemical elements that are found in the sintered samples was done using ESPRIT software (BRUKER, version 1.9). Mapping was done using Hypermap mode, where every pixel of the image corresponds to an EDS spectrum. Quantification is done using a Gaussian deconvolution of peaks that are associated to each element. Afterwards, the patterns were quantified using the Cliff-Lorimer method [109], which can determine the relative concentration of different elements based on the intensity of the peaks. For a binary system (where A is manganese, and B is silicon) it can be written as:

$$\frac{C_A}{C_B} = k_{AB}\frac{I_A}{I_B} \tag{2.10}$$

where C_A is the atomic fraction of the element A, C_B is the atomic fraction of the element B, I_A and I_B correspond to the intensity of the peaks for elements A and B, respectively, and k_{ab} is the Cliff-Lorimer factor or *k*-factor. Cliff-Lorimer factor is defined as:

$$k_{AB} = \frac{(Q\omega a)_A A_B \varepsilon_A}{(Q\omega a)_B A_A \varepsilon_B} \quad 2.11$$

where A is the atomic weight, Q is the ionization cross section (how easily a particular atom is ionized by a particular electron), ω is the fluorescence yield (ionization fraction resulting in X-ray emission), a is the relative intensity factor (fraction of the total measured *K* line intensity of an element), and ε the detector efficiency for a measured element. The sum of all atomic fractions for a binary system (A, B) is written with expression $C_A + C_B = 100\%$.

In ternary and higher order systems, the intensities of all the elements, whose mass concentrations are unknown, must be measured, or the weight fraction of a particular element in the sample must be known in advance of the analysis [110]. For a three-element analysis (in our case A is magnesium, B is silicon and C is tin):

$$\frac{C_A}{C_B} = k_{AB} \frac{I_A}{I_B} \quad 2.12$$

and

$$\frac{C_B}{C_C} = k_{BC} \frac{I_B}{I_C} \quad 2.13$$

where C_C is the atomic percent of the element C. The sum of all atomic fractions for a ternary system (A, B and C) is written as $C_A + C_B + C_C = 100\%$.

The k-factors are usually calculated from experiments, by using standards where the concentration of elements of interest are known. But they may also be theoretically calculated using equation 2.11. In our case, the k-factors used for our quantifications have been theoretically calculated using Esprit software by introducing the key parameters related to the Osiris TEM equipment used.

2.9 Measurement of thermoelectric properties

2.9.1 Preparation of sample for characterization

After successful production of pellets by SPS, the sample needs to be polished to remove the papyex and reveal the native sample. To do this, a SiC based polishing material was used. When a shiny surface is obtained, the sample is cut on a cutting machine (figure 2.17), following the scheme presented on figure 2.16. Excess material is used for SEM imaging.

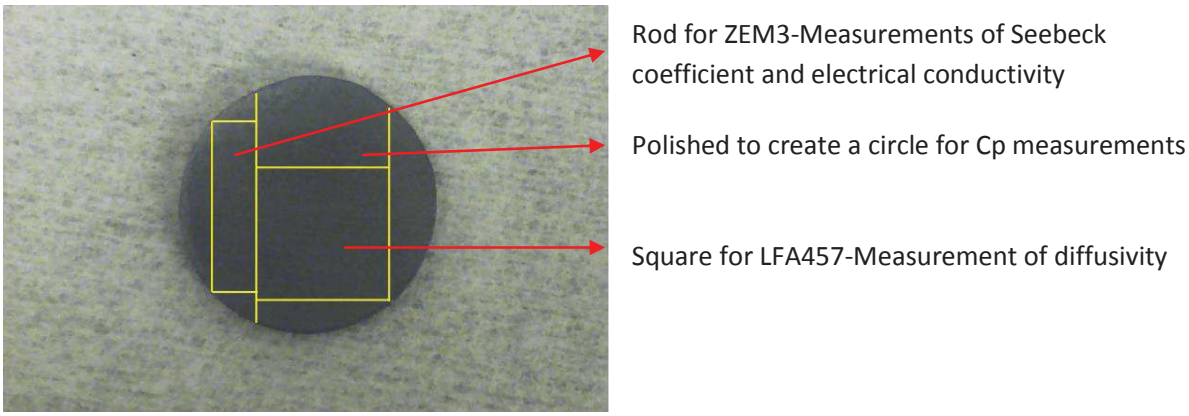

Figure 2.16: *Cutting of the samples for measurements.*

The contact with water should be avoided for Mg-Si-Sn alloys, as the sample quickly changes color from grey to dark-gray or even to rainbow colors. Additional polishing by SiC paper is then required to remove the oxidized layer of the sample after cutting it with water-based solution. Consolidated samples were polished on Mechatech 234 (PRESI) equipment.

Cutting is performed on IsoMet 1000 Precision Saw (Buehler) with a rotary blade. The speed is set to 175 rpm, as it was found to be the most efficient speed that doesn't damage the sample. The cooling was performed with a water-based emulsion. Water creates a layer of oxides on the surface of the sample. Therefore, it is necessary to additionally polish the surface.

Figure 2.17: *Cutting machine with the disc shaped blade - IsoMet 1000 Precision Saw (Buehler).*

As $Mg_2Si_{1-x}Sn_x$ acts as a brittle material, the pressure during the cutting procedure is quite important. It should be reduced as much as possible, therefore enabling the clean cut without parts breaking off.

Cutting of Mn-Si is much easier. Higher speeds of cutting can be imposed on the samples (up to 250 rpm) without damaging the edges of the cut sample.

2.9.2 Electrical measurements

As the material was polished and cut, a prepared rod (dimensions $3 \times 2 \times 15$ mm^3) is used for measuring the Seebeck coefficient and the electrical conductivity. For this, a ZEM3 equipment (ULVAC-RIKO) is used (figure 2.18). For $Mg_2Si_{1-x}Sn_x$ the sample was heated up to 500°C. For $MnSi_{1.75}$, maximum temperature was 600°C. Measurements were done in helium atmosphere to avoid the oxidation of the samples.

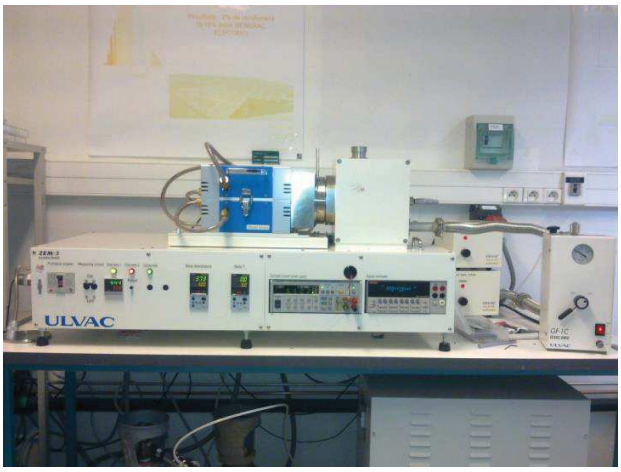

Figure 2.18: *ZEM-3 machine.*

The rod dimensions were measured and they were given to ZEM-3 software. Rod is placed between metallic nickel electrodes. Two C-type thermocouples were put on the surface of the sample (temperature probes) (figure 2.19).

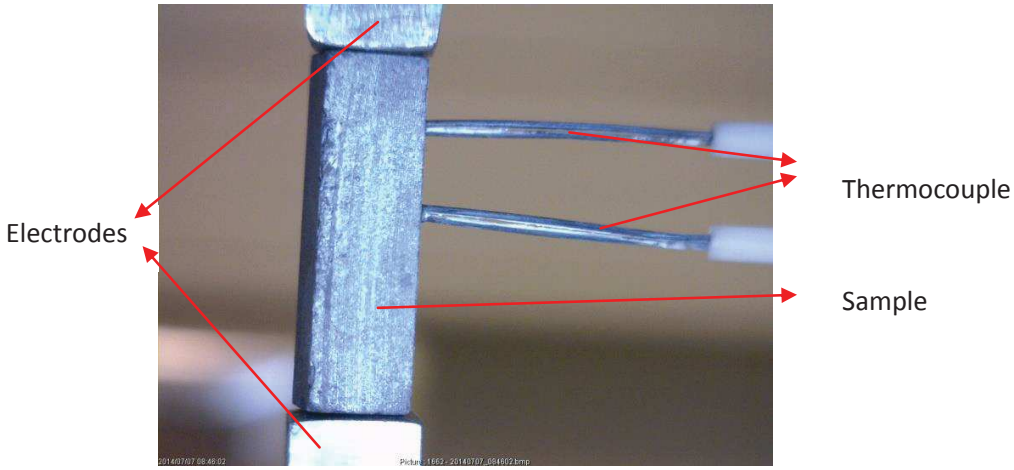

Figure 2.19*: Placement of the specimen in the ZEM3 and important parts.*

Besides the dimensions of the sample, the distance between the thermocouples is introduced into the machine software. This distance is measured using a camera. This is of outmost importance as it is one of the parameters needed to calculate the electrical conductivity.

2.9.3 Electrical conductivity

The electrical conductivity (inverse of the electrical resistivity, ρ) of the samples, *σ*, was measured by a four-point direct current (dc) switching technique. Contact resistance was measured between two metal (nickel) electrodes, two temperature sensors (C-type thermocouple) and the sample (figure 2.20). Current is introduced throughout the sample, while the voltage is concentrated on a small area using the thermocouple.

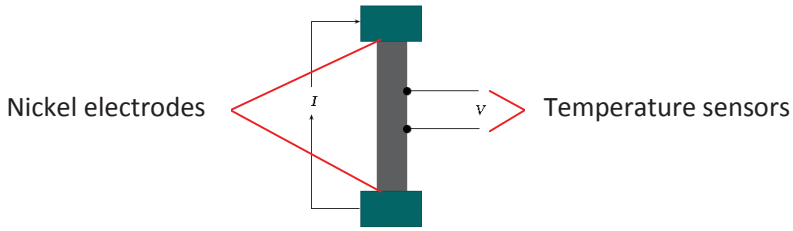

Figure 2.20: *Measurement of the electrical conductivity.*

It is necessary to obtain a good contact on all points so that the curve of I-V is linear. When the contact is successfully established, the electrical resistivity (ρ in Ω.m) is measured in the set temperature interval. The value is corrected by the dimensions of the sample and:

$$\rho = \frac{A}{l}\left(\frac{V}{l}\right) \qquad 2.14$$

where *A* is the base surface area (width×thickness of the sample) of the sample measured, *l* is the distance between the probes (thermocouples), and *V* is the voltage that is created when the current is flowing through the sample. Voltage is directly connected to the current and the measurements are made on every temperature segment.

Temperature of the probes is held at a constant value to reduce the voltage change for measuring Seebeck's coefficient. Electrical conductivity is then easily calculated as inversed electrical resistivity.

2.9.4 Seebeck Coefficient

Seebeck coefficient is measured by introducing a temperature difference between the probes and can be mathematically written as:

$$S = \left|\frac{\Delta V}{T_2 - T_1}\right| \qquad 2.15$$

where ΔV is the difference of potentials (voltage) on two probes, and T_2 and T_1 are the temperature on each separate probe (figure 2.21). Depending on the sign of *S* we can conclude if the material has a p-type (positive Seebeck coefficient) or an n-type (negative Seebeck coefficient) nature.

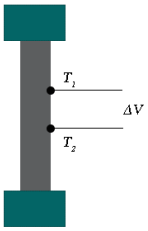

Figure 2.21: *Measurement of the Seebeck coefficient.*

Seebeck coefficient is measured by the probes. The temperature difference of the different ends of the sample is obtained by heating the lower electrode. Imposed temperature difference is 10, 20, and 50 °C. In this manner, the Seebeck measurements are much more precise. At the end, collected data is treated by ZEM-3 software to obtain the average value for a given temperature range.

2.9.5 Hall Effect measurements

The power factor of a thermoelectric material varies significantly with carrier concentration. Thus, it is necessary to measure the carrier concentration by a Hall effect measurement apparatus [111]. When a current carrying conductor is put into a magnetic field, the Lorentz force deflects moving charge carriers to one side of the sample and generates an additional electric field perpendicular to both the current direction and the magnetic field. From the measurement data, the Hall coefficient, which is the ratio of the perpendicular electric field to the product of current density and magnetic field, and the resistivity are calculated. Thus the carrier mobility is obtained as well, which is the product of the Hall coefficient and electrical conductivity.

If I is the current passing through the conductor with thickness b, and there is a magnetic field *B*, then the Hall voltage V_H is given by:

$$V_H = -\frac{IB}{nbe} \tag{2.17}$$

where *b* is the thickness of the material, *B* is the magnetic field, *e* is the elementary charge, and *n* is the charge carrier density of the carried electrons.

Besides measuring Hall voltage, it is possible to measure the concentration of the charge carriers. In the case of a semiconductor, it is possible to determine the type of the carriers using the Hall coefficient R_H:

$$R_H = \frac{E_y}{j_x B} = \frac{V_H t}{IB} = -\frac{1}{ne} \tag{2.18}$$

where E_y is the induced electric field and j_x is the current density of the carrier electrons. If $R_H > 0$ then the main charge carriers are holes (p-type semiconductor) and if $R_H < 0$ then electrons are the main charge carriers (n-type semiconductor). As the resistivity of the material is known, it is possible to measure the mobility, μ, of charge carriers:

$$\mu = \frac{|e|n}{\rho} \tag{2.19}$$

Mobility is important because it gives the information how quickly an electron (or hole) can move through a semiconductor when pulled by an electric field. As mobility is connected to the velocity, we can say that drift velocity expression is:

$$V_d = \mu E \tag{2.20}$$

V_d Is the average velocity of electrons when electrons are under the influence of an electric field, *E*.

2.9.5.1 Measuring charge carriers

Sample holder has a four point contact with the sample. Contact was controlled via the current (I)-voltage (V) diagram. Standard equipment (HMS-3000, Four Point Probes/Bridge Technology) was used for measurement of the carrier concentration in air (figure 2.22).

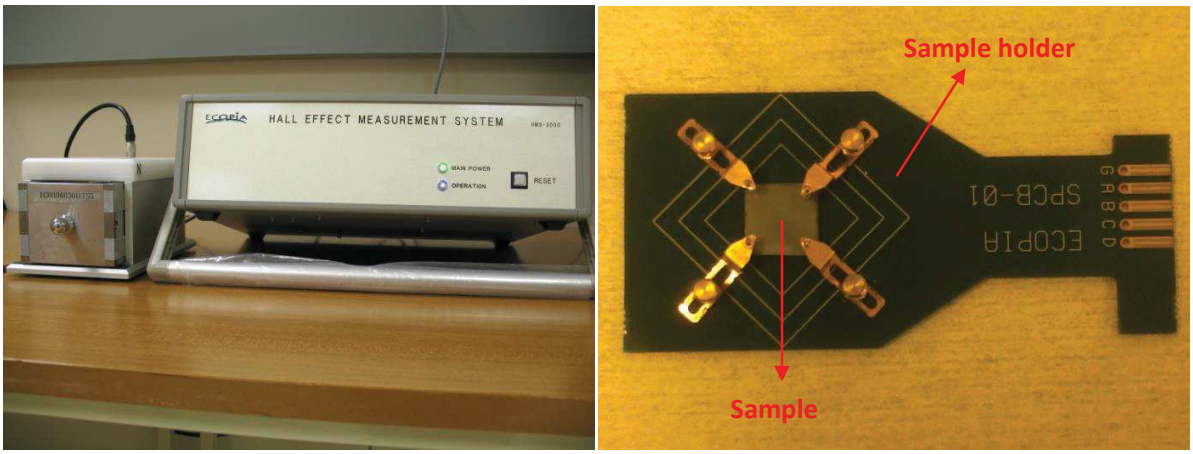

Figure 2.22: *HMS-3000 system and sample holder.*

To obtain better contact and provide accurate measurements, the thickness of the sample should be below 0.5 mm. Different thicknesses were tried (1.5 mm, 1.1 mm, 0.7 mm, and 0.5 mm) resulting in the same measured values. The only difference is that higher thicknesses lead to higher oscillations in the obtained data. This is eliminated by measuring more than 20 times the parameters and creating an average value which is consistent with the value of samples with lower thicknesses.

2.9.6 Thermal conductivity

2.9.6.1 Preparation of the sample

Samples were cut to squares of 10×10 mm^2. Sample surface was covered by a thin layer of carbon to avoid the reflection of laser during measurement. Afterwards, they were mounted on SiC sample holders and placed in LFA-457 MicroFlash (Netzsch-Gerätebau GmbH). The atmosphere was argon, and samples were heated up to 500°C with the following temperature sequence: until 100°C the heating rate was 1°C/min, up to 200°C heating rate was 2°C/min, up to 300°C with 5°C/min, and up to 500°C with 10°C/min with 3 shots and 2s cooling time between shots.

2.9.6.2 Thermal diffusivity

The thermal conductivity is one of the hardest parameter to evaluate. For the precise measurements of thermal diffusivity, specific heat and thermal conductivity, the laser flash technique (LFA-457 MicroFlash Netzsch-Gerätebau GmbH) has proven itself as a fast, versatile and absolute method.

The front surface of a plane-parallel sample is heated by a short light or laser pulse. The temperature rise on the rear surface is measured versus the time using an IR detector. The thermal diffusivity (α) is measured and the specific heat (c_p) can be determined from the measured signal. The density (ρ) is measured by Archimedes method. Then, the thermal conductivity can be determined as follows

$$\kappa(T) = \alpha(T) c_p(t) \rho(T) \left[\frac{W}{mK}\right] \quad 2.21$$

For measuring the thermal conductivity, LFA 457 Micro-Flash, (Netzsch-Gerätebau GmbH was used).

In theory, the temperature should increase monotonously to a limit. In the actual experiment, the measured temperature has a T_{max} value before checking the oven temperature. In the time required to reach the half of the temperature peak (relative to the temperature of the oven) allows determining the thermal diffusivity:

$$\alpha = \frac{1.37 \cdot b^2}{t_{0.5} \cdot \pi^2} \left[\frac{cm^2}{s}\right] \quad 2.22$$

where b is the thickness of the sample and $t_{0.5}$ is the time needed to achieve T_{max}.

2.9.6.3 Heat capacity at constant pressure

Differential Scanning Calorimetry (DSC) is one of the most frequently employed thermal analysis methods. All the samples were measured using this technique. It can be used to analyze nearly all energetic effects occurring in a solid or liquid during thermal treatment. The equipment we used was DSC 404 F1 Pegasus (Netzsch–Gerätebau GmbH).

Samples created for these measurements were circular with a 5.2 mm diameter and thickness of 1 mm, so that they may be put a platinum crucible with same dimensions (keeping the dimensions and mass close to the reference). Surface was highly polished and parallel so that sample can create good contacts. Thusly, a good heat exchange between the sample and the crucible is obtained.

Heat flows into the sample as a result of heating. DSC measures the difference in heat flow rate between a sample and an inert reference as a function of time and temperature. Another parameter is the baseline.

Accurate data is obtained when all three measurements (sample of importance, sample of reference and baseline) are done with the same conditions (same day with the same measurement program). Measurements were made with two platinum crucibles with a coating of alumina. Coating prevents interactions between the sample and the crucible. To calculate the baseline, two empty crucibles were placed in the DSC equipment. Afterwards, the sample of reference was placed in one crucible while the other crucible was left empty. Finally the sample of importance was placed in the crucible and measured along side with an empty crucible. The heat capacity at constant pressure is calculated as:

$$c_p = \frac{m_{reference} \cdot signal\ difference\ (sample - baseline)}{m_{sample} \cdot signal\ difference\ (reference - baseline)} \cdot c_p(reference.) \qquad 2.23$$

All measurements were done under an argon stream, with a heating rate of 20 °C / min. Data were registered in function of time and temperature.

2.9.6.4 Calculating the reduced figure of merit and uncertainties

Once we have performed electrical and thermal measurements, we are able to calculate the figure of merit ($ZT = \sigma S^2/\kappa$, where σ is the electrical conductivity, S is the Seebeck coefficient, and κ is the thermal conductivity). However, the uncertainty of this calculation is very important. These uncertainties depend on the equipment that is being used for measurements.

Therefore, ZEM-3 equipment has uncertainty of $\pm$ 3% and $\pm$ 1.5 % when measuring electrical conductivity and Seebeck coefficient, respectively. Total uncertainty from the thermal conductivity measurements are contributed by two devices (thermal diffusivity measurement on LFA-457 MicroFlash and heat capacity measurement on DSC 404 F1 Pegasus) and its value amass to $\pm$ 6%.

Finally, we have the total uncertainty value for the figure of merit (ZT) of $\pm$11.5 % that is represented by the sum of all uncertainties. Additionally, it is very rare to see in publications the uncertainty of the published results, which, depending on the equipment, can be as high as 21 %.

2.10 Conclusion

In this chapter, we have shown that the Mg-Si-Sn phase diagram is based on two phases: Mg_2Si and Mg_2Sn. The lattice parameter of $Mg_2Si_{1-x}Sn_x$ alloys varies linearly between the one of these two compositions. The problem of defining the $Mg_2Si_{1-x}Sn_x$ phases exist in the miscibility gap ($0.4<x<0.6$) where linearly expectable solid solutions do not exist. On the other hand, the binary Mn-Si system was shown to be much more complicated when it comes to the material we are interested in: i.e the higher manganese silicides family (HMS). Due to a peritectical reaction that controls synthesis, HMS single phase materials are difficult to create without the additional metallic MnSi phase, which has been shown to drastically lowers the thermoelectric properties. Also, due to the stackable crystal structure of HMS, different HMS species may form alongside the targeted one.

Additionally, the second chapter exposed how were synthesized the powders of interest for our investigations. In the same time, we explained why we have chosen spark plasma sintering to sinter our powders and what were the experimental setup we used. Then the methods used to measure the thermoelectrical properties and to investigate the microstructure of the dense as-sintered materials we manufactured have been explained.

CHAPTER 3

First investigations on an N-type $Mg_2Si_{0.3875}Sn_{0.6}Sb_{0.0125}$ thermoelectrical material

(This chapter is mainly the reproduction of a paper accepted for publication: Journal of Alloys and Compounds 598 (2014) 272–277)

3.1 Introduction

N and P-types $Mg_2Si_xSn_{1-x}$ alloys, with x varying from 0.2 to 0.8, have been deeply investigated for thermoelectrical applications in the 300–600 °C temperature range [36,37,38,39,41,42,43,44,112,113]. Nonetheless, processing methods to elaborate such materials of interest are complex, with numerous subsequent steps, and time consuming.

To prepare the raw powders he investigated, Liu was using a two-step solid state reaction method [42,43,37]. Commercial high purity powders of silicon, tin and antimony were weighted in stoichiometric amounts and powdered magnesium was added with an excess of several percent over its stoichiometric amount in order to compensate its evaporation at high temperature. The constituents were hand-ground in an agate mortar in a glove box, cold pressed and sealed in quartz tubes under vacuum for the first step of the solid state reaction at 600–700 °C. In order to promote the solid solution formation and to increase the homogeneity of the products, the resulting pellets were ground to fine powders in the glove box, cold-pressed again into cylinders and then sealed in quartz tubes in vacuum for the second stage solid state reaction at 700 °C. Finally, after the solid state reaction was completed, the compacts were ground into fine powders in a glove box and consolidated into dense bulk materials using spark plasma sintering (SPS). For an N-type $Mg_{2.14}Si_{0.39}Sn_{0.60}Sb_{0.009}$ composition (antimony being the dopant), a ZT peak value of 1.3 is obtained between 465 and 510 °C [42].

Zaitsev manufactured polycrystalline ingots of $Mg_2Si_{1-x}Sn_x$ solid solution by direct melting of the components in boron crucibles using high-frequency heating [38,39]. Long-time annealing was used for homogenization of the samples. Concentration of current carriers was controlled by antimony additions. A ZT peak value of 1.1 is measured for temperatures ranging from 430 to 530 °C for an N-type material having the $Mg_2Si_{0.4}Sn_{0.6}$ target composition with 3.7×10^{20} carriers/cm^3 [38].

Zhang [40] used a similar process to the one developed by Zaitsev to prepare the materials he investigated. The obtained ingots were ball milled and hot-pressed to obtain dense samples. Using also antimony as a dopant, he obtained a ZT peak value of 1.1–1.2 at 530 °C for an N-type $Mg_2Si_{0.3925}Sn_{0.6}Sb_{0.0075}$ formulation.

In the present chapter we are reporting about the microstructure / thermoelectrical properties of a $Mg_2Si_xSn_{1-x}$ sample that was sintered by SPS from a raw powder synthesized by mechanical alloying, a method thought to be simpler than the ones used up to now and described above.

3.2 Materials and methods

3.2.1 Material

A granulated n-type $Mg_2Si_{0.3875}Sn_{0.6}Sb_{0.0125}$ (target composition is then 66.66 at.%, 12.92 at.%, 20.00 at.% Sn and 0.42 at.% for Mg, Si, Sn and Sb respectively) alloyed powder was prepared by mechanical alloying, in an argon atmosphere, using magnesium (99.98%), silicon (99.999%), tin (99.80%), and antimony (99.50%) precursors (Sigma–Adlrich Chemie S.A.R.L., Saint-Quentin Fallavier, F, for Mg, Sn, Sb and Alfa-Aesar France, Schiltigheim, F, for Si). A planetary ball mill (PM100, Retsch France, Eragny sur Oise, F) was selected with zirconia jar and balls. A 1 wt.% of cyclohexane was also added as a processing aid. The quantity of powder produced is 25 g in 60 h (yield is around 99.5% in weight) for a milling speed set to 300 rpm and a ball to powder ratio of 25. Laser granulometer measurement and SEM observations showed that the collected powder is made of aggregates having a diameter in the range 2–30 µm. X-ray diffraction (XRD, D5000, Bruker AXS SAS, Champs-sur-Marne, France) shows that the alloyed powder exhibits only peaks that match quite well with the $Mg_2Si_{0.4}Sn_{0.6}$ phase. Each individual peak has a symmetrical profile (more evident at high diffraction angle values, as it can be seen on figure 3.1). Consequently, the alloy of interest is completely formed after the mechanical alloying step. Treating XRD spectrum using the Williamson–Hall (W–H) method [105] shows that each aggregate is composed of elemental crystallites having an average diameter around 30 nm.

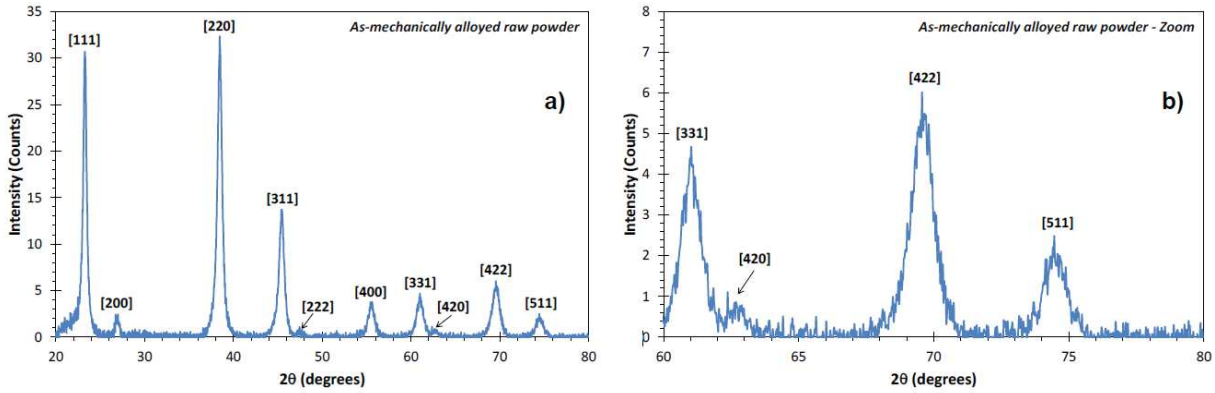

Figure 3.1: *XRD spectra on the as-mechanically alloyed raw powder: (a) Complete spectrum; (b) Zoom on the high diffraction angle values for the as-mechanically alloyed powder.*

3.2.2 Spark Plasma Sintering (SPS)

SPS has proved to be an efficient method to sinter metallic [97,98], ceramic [99,100,101,114,115], quasicrystalline [102], semiconductor [56,116]and glass [103] powders in a short time (cold to cold sintering cycles of few tens of minutes), with a perfect control of the final microstructure (relative density, grain size and residual porosity location if any). This method has been retained for sintering the raw powder we synthesized using mechanical alloying.

SPS runs were conducted in argon atmosphere (pressure set to 1035 hPa), on a HPD-25 equipment (FCT Systeme GmbH, Rauenstein, Ge). A graphite die (internal diameter of 20 mm, thickness of 15 mm) was filled with 2 g of the selected powder and mounted on the SPS equipment (graphite punches). A heating rate of 100 °C/min, a macroscopic compaction pressure of 50 MPa (applied at room temperature on the powder bed) and the standard 12:2 pulse sequence for the DC current [99] were chosen. The temperature was obtained from a thermocouple positioned at the close vicinity of the sample that was sintered.

The apparent density of the sintered samples was measured using the Archimedes's method with absolute ethanol (dry, wet and humid masses were measured).

A typical bell-shape curve is observed for the variation of the instantaneous densification rate in function of temperature (Fig. 3.3) for the as-mechanically alloyed powder, as it is usually the case for ceramic [99,100,101,114,115] and silicon–germanium alloyed powders [56,116].

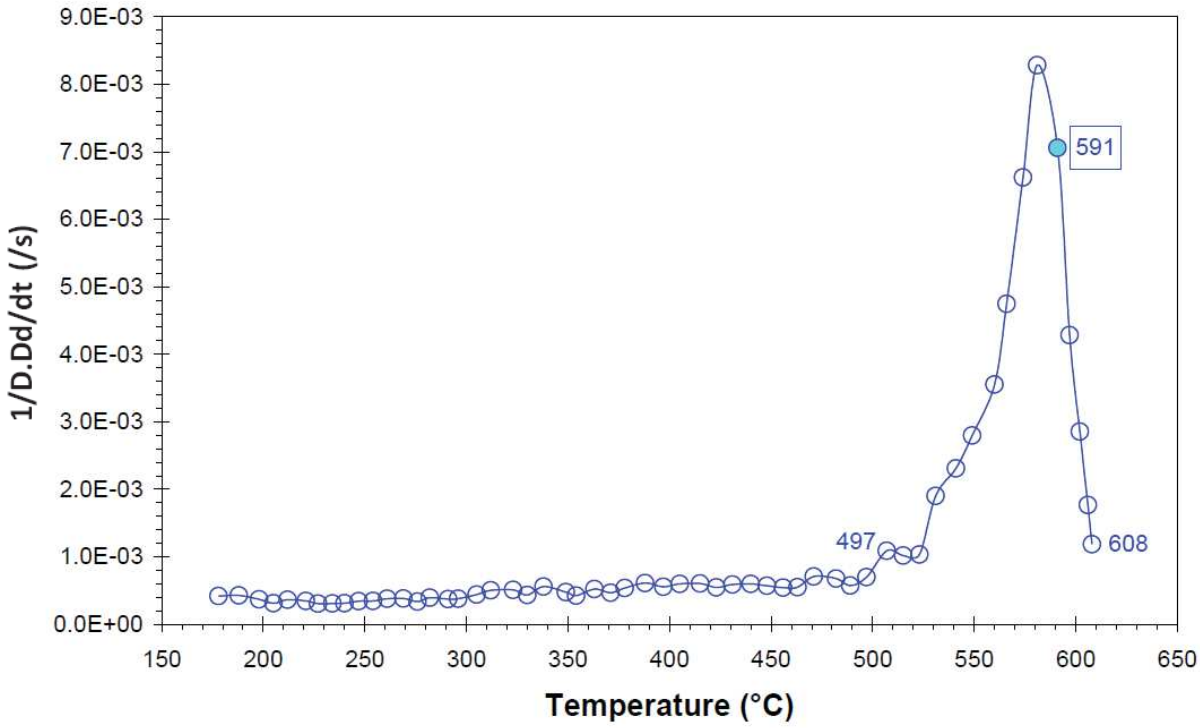

Figure 3.2: *Evolution of the densification rate in function of temperature.*

Densification starts around 500 °C and ends around 610 °C giving a sintering window that is very narrow. The maximum densification rate is 8.3×10^{-3}/s at 580 °C. Consequently, all other parameters being fixed and similar to the ones exposed above, samples were then sintered at 590 °C with a soak time ranging from 0 to 20 min. In all cases the cooling rate was fixed to 50 °C/min from 590 to 400 °C and, afterwards, natural cooling of the equipment was used. In this chapter, we have decided to focus on the particular sample sintered during 7 min at 590 °C.

Figure 3.3a and b shows the XRD spectrum acquired on the as-sintered material. As for the raw powder, all peaks are matching with the $Mg_2Si_{0.4}Sn_{0.6}$ phase (JCPDS reference file 01-089-4254).

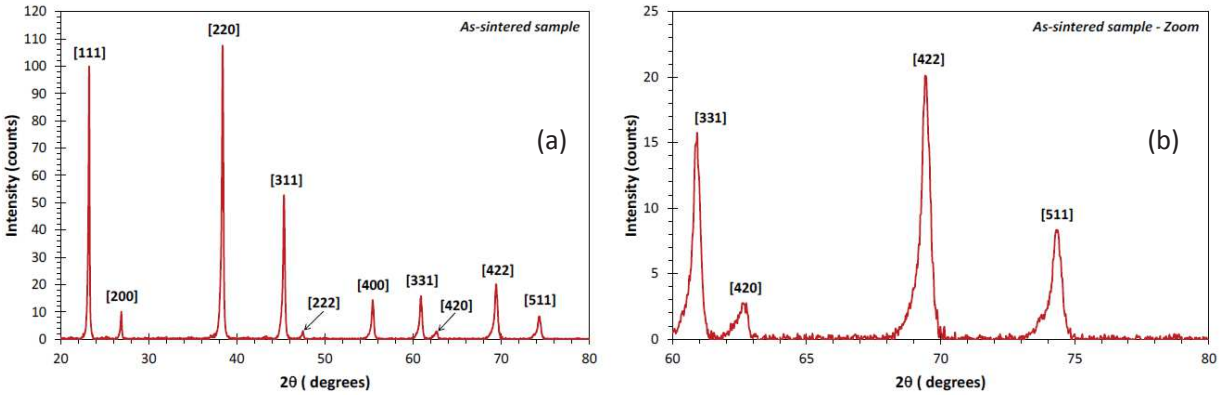

Figure 3.3: *XRD spectra on the as-sintered sample: (a) Complete spectrum; (b) Zoom on the high diffraction angle values for the as-mechanically alloyed powder.*

Nonetheless, peaks are slightly shifted to lower diffraction angle values which could be related to residual internal stresses having a tensile nature (first order stresses). Figure 3.3b shows also that peaks observed at high diffraction angle values are not symmetrical anymore. A clear shoulder is observed on their left side that is compatible with the presence of an $Mg_2Si_xSn_{1-x}$ phase containing a high amount of tin. Nonetheless, it is quite difficult to determine the x value from the XRD spectrum because of possible residual internal stresses in the sintered material affecting the real position of the peaks.

3.3 Measurement of thermoelectric properties

For thermoelectrical properties investigations, samples were machined from the central part of the as-sintered compact. The electrical conductivity of the samples, σ, was measured by a four-point direct current (DC) switching technique and the Seebeck coefficient, S, was measured by a static dc method based on the slope of the voltage versus temperature-difference curves (ZEM-3, Ulvac GmbH, Ismaning, Ge, samples are parallelepipeds of about 3 × 3 × 15 mm^3, working atmosphere is helium, overall measurement errors are ±2.5 % and ±1.5 % for electrical conductivity and Seebeck coefficient, respectively).

The thermal diffusivity was measured using laser-flash method (LFA 457 MicroFlash®, Netzsch-Gerätebau GmbH, Charbonnières les Bains, F, and samples are squares of 10x10 mm^2 with a thickness of 1 mm, working atmosphere is argon). The Specific heat was determined using differential scanning calorimetry (DSC 404 F1 Pegasus, Netzsch-Gerätebau GmbH, Charbonnières les Bains, F, samples are cylinders having a diameter of 5.2 mm and a thickness of 1 mm, working atmosphere is argon). We then calculated the thermal conductivity, κ, as the product of thermal diffusivity, specific heat and volumetric mass density of the samples (the

overall measurement error is ±6 %). To find out the contribution from the charge carriers and the lattice (phonon vibrations) to the total thermal conductivity, we estimated the carrier part via the Wiedemann–Franz–Lorenz relation: $\kappa_c = L_0 T\sigma$, with a Lorenz number L_0 of 2.45×10^{-8} V^2 K^{-2} that applies for degenerated semiconductors. The lattice thermal conductivity κ_l is then deduced from the simple relation $\kappa = \kappa_c + \kappa_l$.

The Hall effect method at room temperature (HMS-3000, Four Point Probes/Bridge Technology, Chandler Heights, AZ, US, samples are 10x10 mm^2 squares with a thickness of 0.25 mm, working atmosphere is air) was also used to determine the main carrier density ($R_H = 1/ne$, where R_H is the Hall coefficient, n is the main carriers density and e is the absolute value of the electronic charge). Knowing the carriers density and the electrical conductivity, it is easy to calculate the carriers mobility ($\sigma = ne\mu$, where μ is the carriers mobility in the samples investigated).

3.4 Post-sintering microstructure investigation

Microstructure of the as-sintered sample has been deeply investigated. A thin foil was prepared from the central zone of the sintered pellet using focus ion beam (Strata DB 235, FEI, Eindhoven, NL). The foil (confined to minimize contacts with air) was observed on a TEM apparatus (Tecnai Osiris, FEI, Eindhoven, NL, acceleration voltage of 200 kV, line resolution of 1.02 Å) equipped with a HAADF detector and an EDS (Energy Dispersive Spectroscopy) microanalysis system (Esprit, Bruker Nano GmbH, Berlin, Ge) connected to four quadrant SDD detectors (ChemiStem technology, FEI, Eindhoven, NL). Chemical quantifications from EDS analyses performed in map-mode have been done using the Cliff–Lorimer method with theoretical k-factors calculated for an acceleration voltage of 200 kV. Some additional investigations were also done using the HRTEM mode. To determine the grain size and the diameter of second phases possibly present in the sintered sample microstructure, image analyses from TEM pictures in bright field mode were performed (Image J free software, developed by the National Institute of Health, US) on at least 100 objects. The two-dimensional surface of each object appearing in the thin foil plan is measured and the diameter of a corresponding disc having the same surface value is calculated (a tridimensional correction factor of 1.2 is used [106]).

Figure 3.4a shows the typical microstructure observed by TEM in the as-sintered sample. The material is an almost fully dense polycrystal.

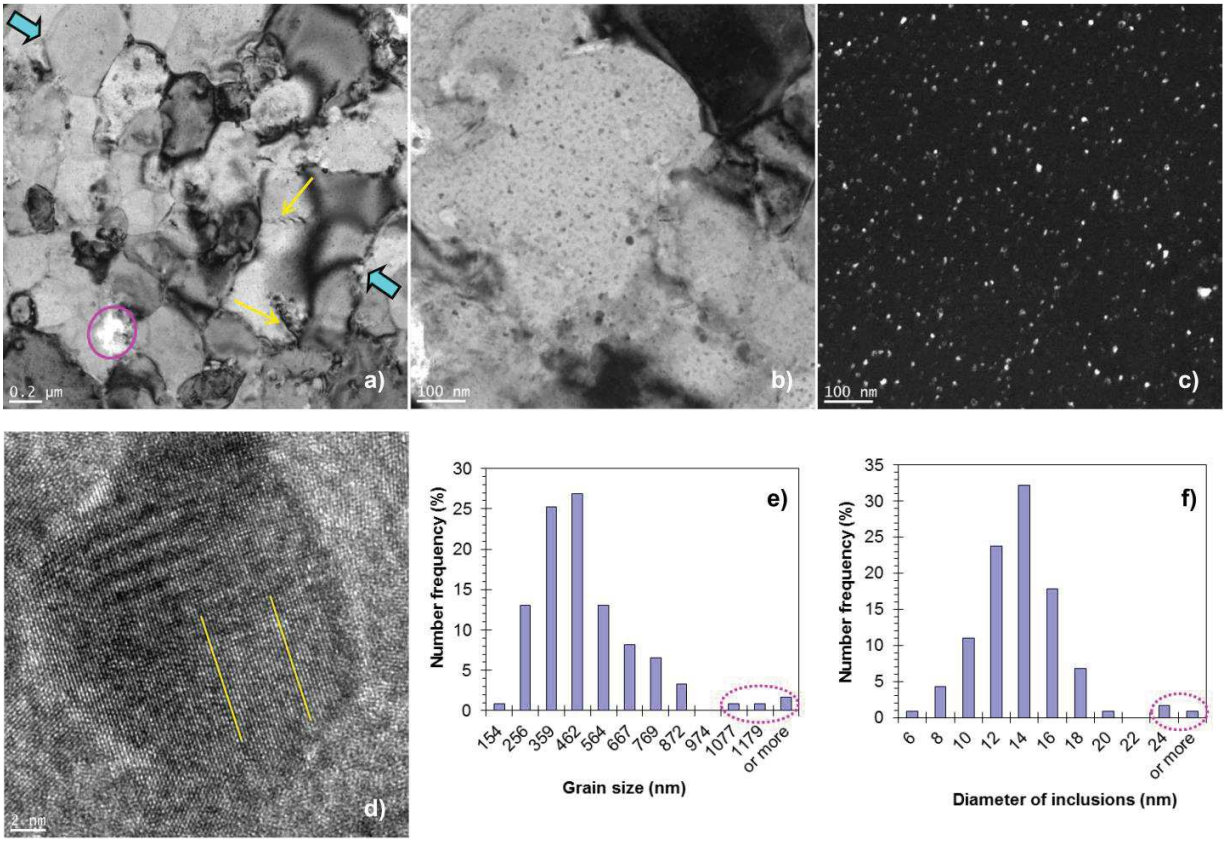

Figure 3.4: *Typical microstructure of the as-sintered sample: (a) general view; (b) detailed view in bright field mode showing very small inclusions; (c) dark field image where most inclusions in the field are illuminated; (d) HRTEM image on an inclusion; (e) grain size distribution in the as-sintered material; (f) inclusions diameter distribution.*

The individual grains are polyhedrons. Most of the grains are elongated/squeezed perpendicularly to a certain direction (blue arrows) that could be the one related to the pressure applied during the SPS run (this point has not scrupulously confirmed at this time). In some grains few dislocations are observed (yellow arrows). In contrary to what is usually observed in most thermoelectrical materials [56,107,116] the individual grains are not twinned. A few of residual porosities are also observed (pink ellipse). Using EDS analyses, it appears that such pores are correlated to oxidation areas.

The grain size distribution of the as-sintered sample is shown in Figure 3.4e. The material exhibits a sub-micron grain size, with a small amount of coarser grains resulting from local abnormal grain growth (pink-doted ellipse). An average grain size around 450 nm is calculated.

Figure 3.4b shows that very small inclusions are homogeneously distributed in the bulk of individual grains. By tilting the thin foil under the electron beam, their contrast is changing

confirming that they have a crystalline nature. Using the diffraction mode and selecting the good spot, it is possible to illuminate most of the inclusions in dark-field mode, as it is shown on Figure 3.4c, confirming that they have close orientations. Figure 3.4f shows that the inclusions have a nanometer-size character with an average diameter around 13 nm. A small fraction of them have a diameter twice the average one (pink-doted ellipse). A concentration of 1.9×10^9 inclusions/mm^2 has been calculated.

Figure 3.4d shows an inclusion observed using the HRTEM mode. Lattice fringes are visible attesting its crystalline nature. The inter-lattice distance is 2.137 Å. It is in good agreement to the inter-lattice distance for the {310} crystalline plans of Mg_2Sn or of an $Mg_2Si_{1-x}Sn_x$ phase with a high value of x. It is also compatible with the presence of shoulders observed on the left side of the main diffraction peaks related to the $Mg_2Si_{0.4}Sn_{0.6}$ phase, as shown in Figure 3.2b.

Figure 3.5a shows a HAADF image in STEM mode of the nanometer-sized inclusions. Most of them do appear bright. EDS maps prove that bright inclusions are enriched in tin (Figure 3.5d) and impoverished in magnesium (Figure 3.5b).

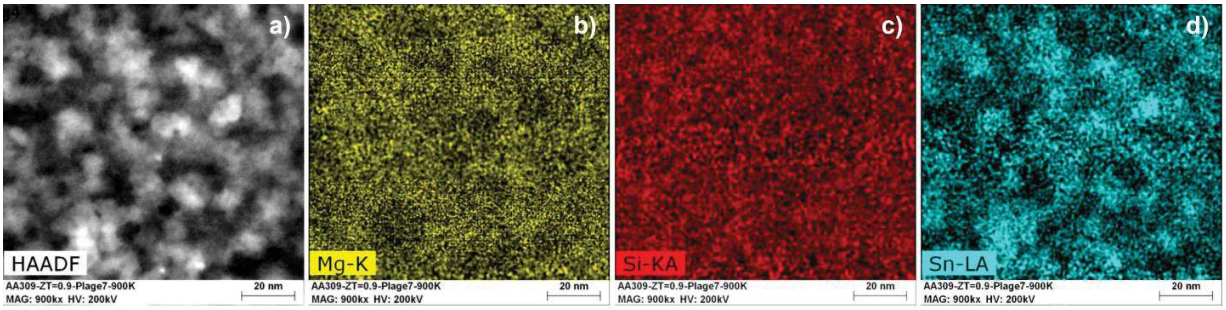

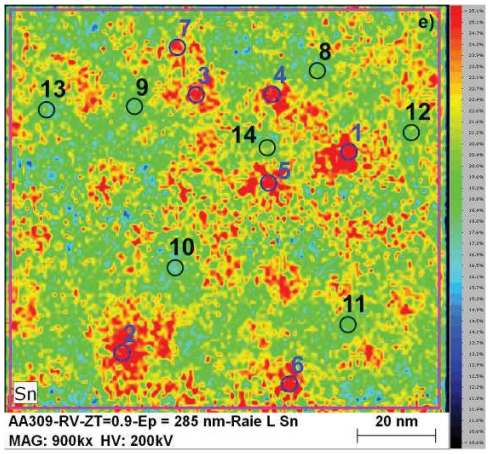

Zone of interest	Mg (at %)	Si (at %)	Sn (at %)
1	60.53	12.06	27.41
2	61.56	12.28	26.16
3	62.18	12.92	24.90
4	61.51	12.75	25.74
5	60.81	12.73	26.46
6	59.82	12.97	27.21
7	60.16	14.90	24.94
8	68.01	12.84	19.15
9	68.15	13.34	18.51
10	67.44	14.82	17.74
11	67.22	13.74	19.04
12	66.43	14.12	19.45
13	66.69	15.11	18.20
14	65.69	13.91	20.40
Average values	60.94	12.94	26.12
Standard deviation	0.78	0.86	0.93
Average values	67.09	13.98	18.93
Standard deviation	0.82	0.73	0.81

Zone of interest	Mg (at %)	Si (at %)	Sn (at %)	Sb (at %)
Global area composition	66.66	14.19	18.68	0.47
Standard deviation	1.16	0.04	1.59	0.08

Figure 3.5: *(a) HAADF image focused on inclusions dispersed in an individual grain; (b) Mg map; (c) Si map; (d) Sn map; (e) Quantitative Sn map.*

The silicon content is almost constant throughout the zone of interest (Figure 3.5c). The corresponding quantitative map for tin is shown in Figure 3.5e (the thin foil thickness estimated to be 285 nm). On this map different local zones of interest are also shown, with the corresponding compositions given in the table presented in Figure 3.5 (Sb content has not been evaluated). The average composition of the bright inclusions is $Mg_{1.83}Si_{0.39}Sn_{0.78}$. The average composition of the surrounding material is $Mg_{2.01}Si_{0.42}Sn_{0.57}$. The composition of the total zone of interest (pink rectangle on Figure 3.5e) is $Mg_{2.000}Si_{0.426}Sn_{0.560}Sb_{0.014}$ (antimony dopant is homogeneously dispersed in the sintered microstructure with a concentration close to the target one).

3.5 Thermoelectric properties

Let us now investigate the thermoelectrical properties of the as-sintered sample. They are summarized in Figure 3.6 and compared to what was obtained by Zaitsev [38,39], Zhang [40] and Liu [42] on similar alloy compositions. The carrier concentration in the material we manufactured has been measured at room temperature around 1.9×10^{20} carriers/cm^3 and the mobility is then calculated to be 39 cm^2/V.s. The carrier content we determined is then of the same order of magnitude than the ones reported by Zaitsev (3.7×10^{20} carriers/cm^3) [38,39], Zhang (1.0×10^{20} carriers/cm^3) [40] and Liu (1.7×10^{20} carriers/cm^3) [42] in the materials they investigated. All graphs shown in Fig. 3.6 shows that different investigators are able to obtain different materials having, most probably, very different microstructures (especially grain size) and dopant levels. Comparing results of Zaitsev [38,39] and Zhang [40], it seems probable that Zaitsev's material has a coarser microstructure, even if both materials have finally a similar dimensionless figure of merit, as shown in Fig. 3.7.

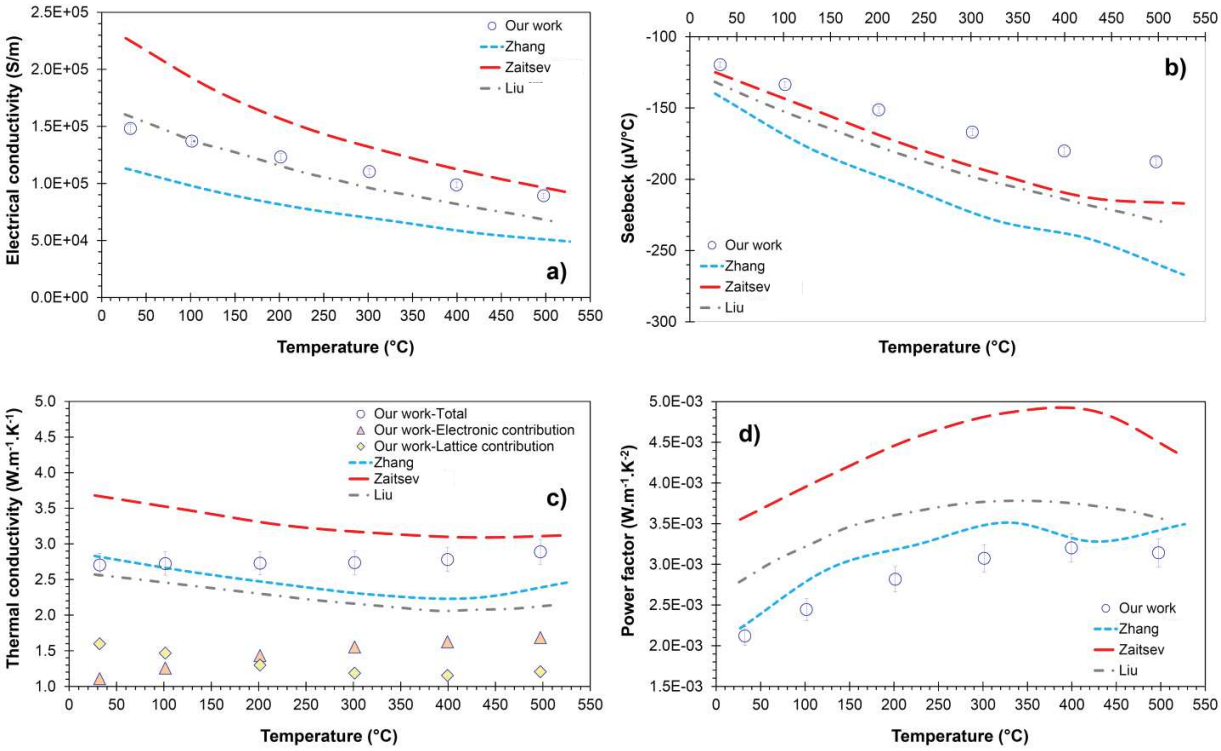

Figure 3.6: *Thermoelectrical properties in function of temperature measured on the as-sintered sample made from powder synthesized by MA: (a) electrical conductivity; (b) Seebeck coefficient; (c) thermal conductivity; (d) power factor.*

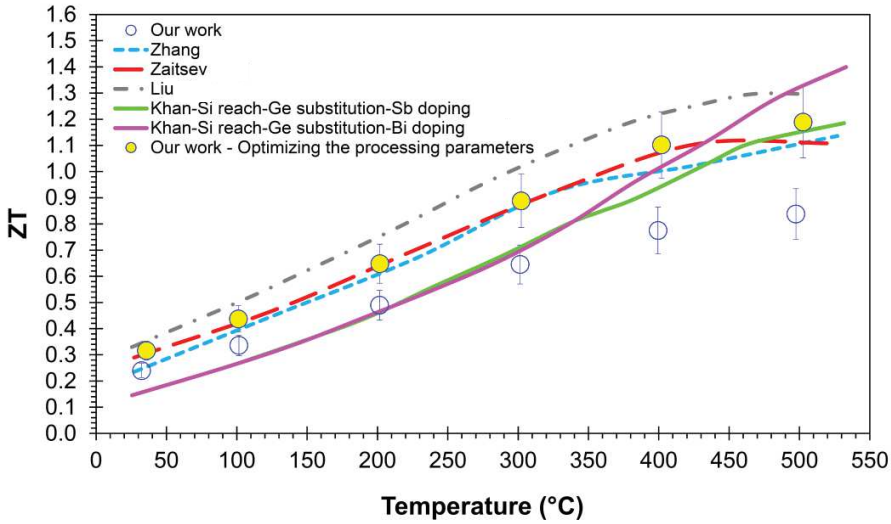

Figure 3.7: *Thermoelectric figure of merit (ZT) in function of temperature.*

Indeed, less grain boundaries (material with a higher grain size) signifies less electrons and phonons scattering, explaining why the electrical and thermal conductivities are significantly higher for Zaitsev's material (Figure 3.6a and c). Our material exhibits also other thermoelectrical properties. The electrical and thermal conductivities we measured (Figure 3.6a and c) are, whatever the temperature, comprised between the values obtained by Zaitsev and Zhang. Then, it is probable that our sample has an average grain size lower than the one of Zaitsev's material and higher than the one of Zhang's material. In comparison to the results we report in this paper and to the ones published by Zhang and Zaitsev, it is interesting to note that the material investigated by Liu [42] exhibits a relatively high electrical conductivity associated to a particularly low thermal conductivity. This behavior is probably correlated to an optimized microstructure (presence of a proper amount of nanometer-sized structural non-uniformities) and to a tailored magnesium stoichiometry in the alloy he investigated [42]. Looking at Fig. 3.6b shows that the sample we characterized is possibly over-doped. Indeed the Seebeck coefficient we obtained is always smaller than the ones measured by Zaitsev [38,39], Zhang [40] and Liu [42] for all temperatures. In the same time, the mobility we measured at room temperature is 17% lower than what it should be in an $Mg_2Si_{0.4}Sn_{0.6}$ ideal composition having a carrier concentration of 2.3×10^{20} carriers/cm^3 [39], then close to the 1.9×10^{20} carriers/cm^3 we have in our material. Figure 3.6c shows the evolution of the thermal conductivity in function of temperature for our as-sintered material. Even if the global thermal conductivity remains always low (2.7–2.9$Wm^{-1}K^{-1}$), it is important to point out that the lattice contribution becomes lower than the electronic one above 200 °C. The presence of Mg–poor/Sn reach nanometer-sized inclusions reported above, homogeneously dispersed in the individual grains constituting the as-sintered polycrystalline material is then thought to maintain the thermal conductivity at a low value, especially for temperatures above 200 °C. Fig. 3.6d shows how the power factor is changing in function of temperature for the as-sintered material we investigated. Because each investigator develops its own material with a given microstructure/dopant level having a direct impact on the electrical conductivity and Seebeck coefficient values, the variations of the power factor in function of temperature are different. Nonetheless, the order of magnitude and the shape of the curves are similar.

Finally, the dimensionless figure of merit in function of temperature for the as-sintered material is finally shown in Fig. 3.7. A maximum ZT value around 0.85 is obtained at 500 °C. Zaitsev [38,39], Zhang [40] and Liu [42] obtained values above 1 on similar compositions for a similar temperature. Nonetheless, the process used to manufacture the samples they characterized is complex and time consuming. In our case, they are only two subsequent steps: synthesis of the alloyed raw powder by mechanical alloying followed by SPS. By optimizing the mechanical alloying (for example by tailoring the amount of processing aid incorporated, as it will be explained in Chapter 4) and SPS (tailoring the heating/cooling rates and pressure release) steps, a ZT around 1.1–1.2 between 400 and 500 °C is measured (Fig. 3.7) on our sintered

samples. The results are then equivalent to what has been previously reported par Zaitsev [38,39] and Zhang [40] but still a little bit below the excellent results of Liu [42]. The optimized material we are now able to manufacture is better in the 20–400 °C temperature range than what has been recently reported for a Si reach/Sn poor $Mg_2Si_xSn_{1-x}$ composition that was also fabricated using complex and time-consuming processes and where Bi was the dopant chosen [104]. Detailed results regarding the optimized material will be presented in the chapter four.

3.6 Conclusions

Mechanical alloying has been shown to be an effective and simple method to elaborate an agglomerated N-type $Mg_2Si_{0.3875}Sn_{0.6}Sb_{0.125}$ powder made of elemental crystallites having a nanometer-size. Spark plasma sintering of the as-mechanically alloyed powder enables the manufacturing of an almost fully dense sample having a sub-micron grain size. Each individual grain constituting the polycrystal contains a huge amount of inclusions having a nanometer- size and that are impoverished in magnesium and enriched in tin in comparison to the surrounding matrix. Such inclusions, homogeneously dispersed in the as-sintered microstructure, are thought to scatter lattice vibrations, leading to a dimensionless-thermoelectrical figure of merit (ZT) around 0.85 at 500 °C. The advantage of the manufacturing process we used is based on only two subsequent steps: synthesis of the alloyed raw powder by mechanical alloying followed by spark plasma sintering. It is simpler and less time consuming in comparison to what is usually used by other authors reporting on the same topic.

Let us now switch to Chapter 4 to show how we are able to increase the ZT parameter of our sintered N-type material.

CHAPTER 4

Thermoelectric properties of an optimized $Mg_2Si_{0.3875}Sn_{0.6}Sb_{0.0125}$ alloy and addition of Half-Heusler nanoparticles to the matrix

4.1 Introduction

Extensive work has been done in pursuing the best way of synthesizing Mg-Si-Sn alloyed powders and different methods of production were used including solid state reaction [37,44], high-frequency heating [38,39] or mechanical alloying [85,118]. Powders were consolidated either by hot pressing [38,39] or by spark plasma sintering (SPS) [37,44,118].

When it comes to consolidation, research was mostly focused on obtaining unbroken and fully dense samples with, if possible, minimum grain growth.

Using SPS, our approach was to use the bell-shaped curve of the instantaneous densification rate in function of temperature for the powders we investigated (figure 3.3, Chapter 3). Then, we picked different temperatures all along the bell-shaped curve (before the main peak, at the main peak temperature and after the main peak) to sinter different samples.

The production of pellets by SPS had some mixed results at first, where only 50% of the samples were produced intact. Then we also optimized the process by adjusting the sintering cycle, giving at the end the highest production output (100% intact samples produced) and the highest thermoelectric properties.

First part of this chapter explains the effect that the optimization of the sintering cycle has on the thermoelectric properties and microstructure of the $Mg_2Si_{0.3875}Sn_{0.6}Sb_{0.0125}$ material.

In a second part, we will show how the addition of a tiny volume fraction of Half-Heusler nanoparticles to the matrix improves the thermoelectric properties.

4.2 Optimization of $Mg_2Si_{0.3875}Sn_{0.6}Sb_{0.0125}$ production

4.2.1 Spark plasma sintering

This time again, we prepared the same granulated n-type alloyed powder by mechanical alloying, in argon atmosphere, with stoichiometry of $Mg_2Si_{0.3875}Sn_{0.6}Sb_{0.0125.}$ Conditions of mechanical alloying are already described in previous chapter, and XRD pattern of the powder is shown in figure 3.3 (Chapter 3).

From the bell-shaped curve of the densification rate in function of temperature shown on figure 3.2 (Chapter 3), we decided to use a global soak temperature of 630 °C, where argon was always the atmosphere (pressure set to 1035 hPa). Heating rate was fixed to 100 °C/min, soak time to 7 minutes and compaction pressure to 45 MPa (always applied at room temperature on the powder bed). Indeed, soak had three different parts. Firstly, the sample is held at 630 °C for five minutes, followed by a minute of slow pressure release (to slowly release the stress in the material) and then another minute at the same temperature to stabilize

thermally the sample. Slow cooling was imposed, with a cooling rate of 20-30 °C/min until 200°C, which differs from the as-sintered sample explained in chapter 3. This was done in order to release slowly residual stresses (at the cost of a possible grain growth in the sintered material).

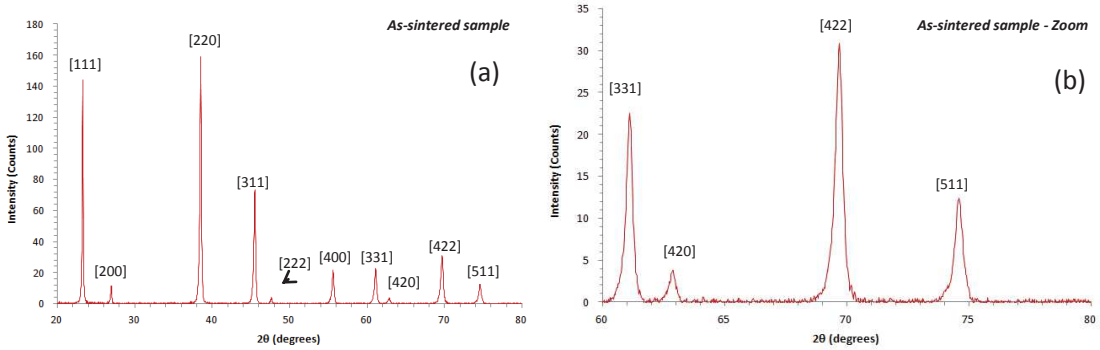

Figure 4.1: *XRD pattern on the as-sintered sample: (a) Complete spectrum; (b) zoom on the high diffraction angle values.*

On the XRD pattern shown on figure 4.1, the peaks related to the $Mg_2Si_{0.4}Sn_{0.6}$ phase are not as asymmetrical as those on figure 3.2. However, shoulders at low diffraction angles are still noticeable, due to the presence of a possible $Mg_2Si_xSn_{1-x}$ phase that contains a high amount of tin. The relative density of the sintered sample was as high as 99.6 %. Treating this XRD pattern with TOPAS software and using the Williamson-Hall method [105], an average grains size of 610 nm was calculated for the as-sintered material. SEM observations on a fresh fracture surface shows (figure 4.2) that the grain growth calculated using TOPAS software is possibly a little bit underestimated.

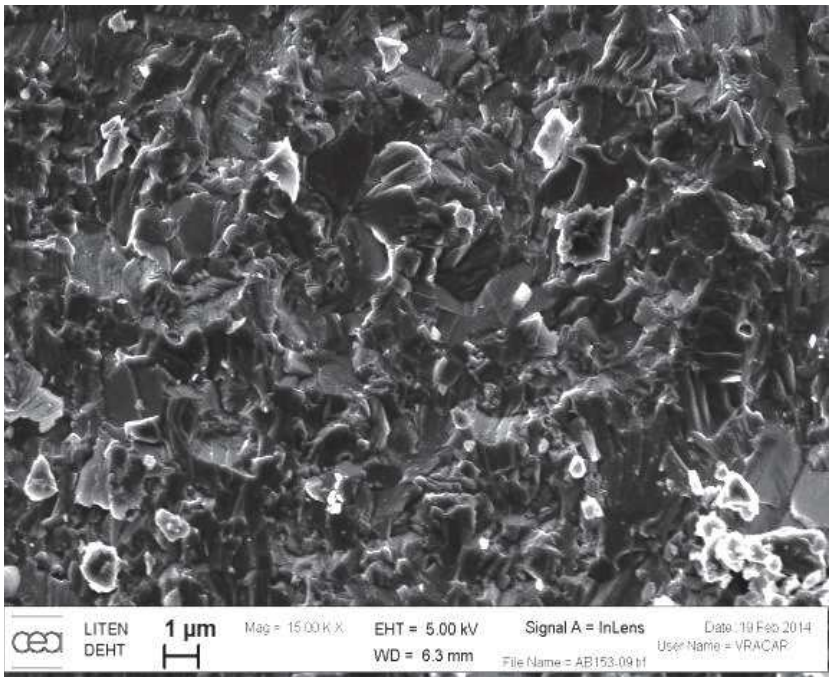

Figure 4.2: *Image of SEM on a freshly broken surface of the sample.*

4.2.2 Post-sintering microstructure investigations of the optimized $Mg_2Si_{0.3875}Sn_{0.6}Sb_{0.0125}$ material

Microstructure of the as-sintered sample was deeply investigated. A thin foil was prepared from the central zone of the as-sintered sample using FIB technique. The foil was kept under vacuum until the observation on the TEM apparatus.

TEM observations in bright field mode show the large grain size, as it is presented in figure 4.3a and 4.3b. The thin foil area of interest exhibited so large grains that we were not able to calculate a grain size distribution from TEM pictures. In the grains of the $Mg_2Si_{1-x}Sn_x$ matrix a great number of precipitates/inclusions are present, as shown in figure 4.3c. The individual grains are seen as polyhedrons. We did not observe any residual porosities or dislocations. The bright polygonal object, named nodule, appearing on figure 4.3a is an oxide-based phase, as it will be shown after.

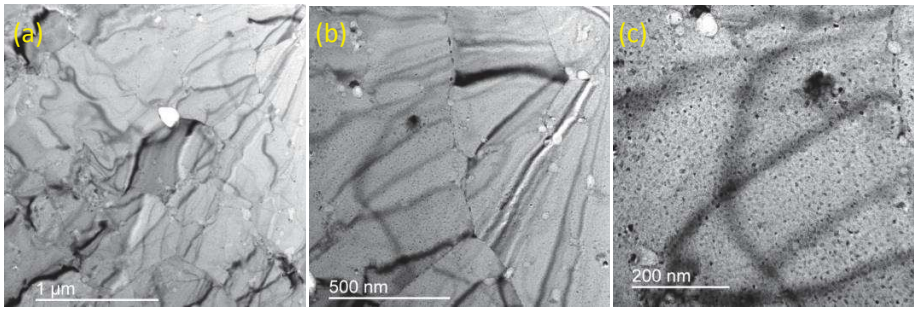

Figure 4.3: *TEM bright field image showing large elementary grains and inclusions.*

Figure 4.4 shows small precipitates/inclusions which are homogeneously distributed in the bulk and at the grain boundaries. In STEM/HAADF mode, they do appear bright, which proves that they are made out of heavy elements, probably tin. In contrary, dark nodules that are also homogeneously dispersed in the sintered microstructure are made of light elements. Consequently, they are most probably oxide-based compounds.

By tilting of the thin foil under the electron beam, the contrast of precipitates/inclusions was changing, which showed their crystalline nature.

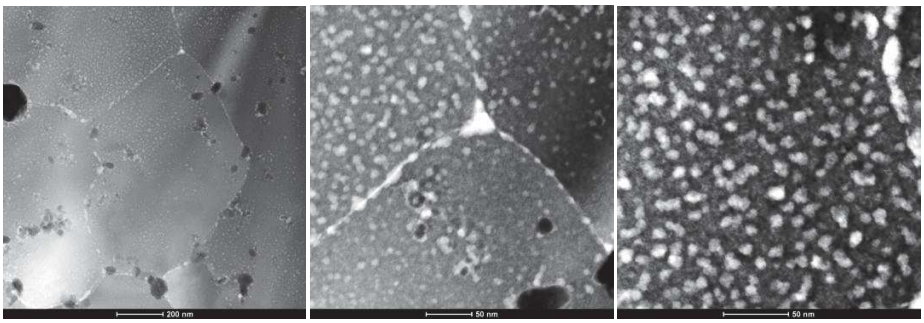

Figure 4.4: *STEM/HAADF image of the optimized sample with bright intergranural/intragranular precipitates/inclusions and dark nodules.*

Typical TEM bright field and STEM/HAADF observations of one of the nodules (the large bright one shown on figure 4.3a in TEM bright field mode) are shown on figure 4.5. Clearly they have an oxide-based composition, with the O peak having a much higher intensity than what is encountered in the surrounding matrix.

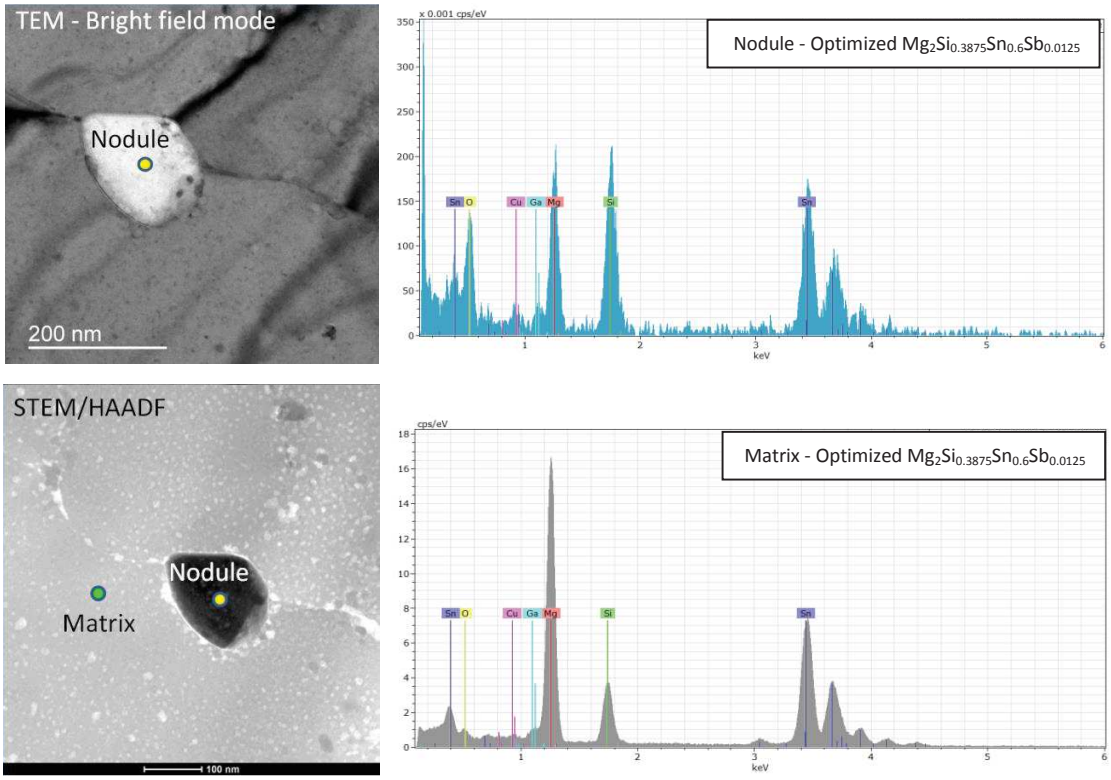

Figure 4.5: *Composition of the nodules and the matrix in STEM/HAADF mode.*

Figure 4.6a and 4.6b show two precipitates/inclusions observed using the HRTEM mode. Lattice fringes are visible, which proves the crystalline nature of these objects. The inter-fringe distance for the precipitate/inclusion shown in figure 4.6a is 2.96 Å. It is in good agreement to the inter-planar distance for the {210} orientation of Mg_2Si (2.84 Å), Mg_2Sn (3.03) and $Mg_2Si_{0.4}Sn_{0.6}$ (2.94 Å). The average composition of the inclusion is then calculated to be $Mg_2Si_{0.35}Sn_{0.65}$ using Vegard's law. For the second precipitate/inclusion, figure 4.6b shows two different series of perpendicular fringes, with inter-fringe distances of 2.99 Å and 3.04 Å. As before, these values are in good agreement to the inter-planar distance for the {210} orientation of Mg_2Si (2.84 Å), Mg_2Sn (3.03) and $Mg_2Si_{0.4}Sn_{0.6}$ (2.94 Å). Using Vegard's law the average composition of this precipitate/inclusion is determined as being $Mg_2Si_{0.13}Sn_{0.87}$, if an averaged value of 3.00 Å is taken for the inter-fringe distance. Then, it is concluded that, at least, two kinds of precipitates/inclusions are present in the as-sintered microstructure.

Figure 4.6c shows the precipitates/inclusions size distribution. An average diameter of 12 nm is calculated, while the one obtained for the non-optimized material was 13 nm (see Chapter 3). The concentration of precipitates/inclusions is $3.7\times10^9/mm^2$, which is then 95 % higher than the one measured for the non-optimized material (1.9×10^9 $/mm^2$, see Chapter 3).

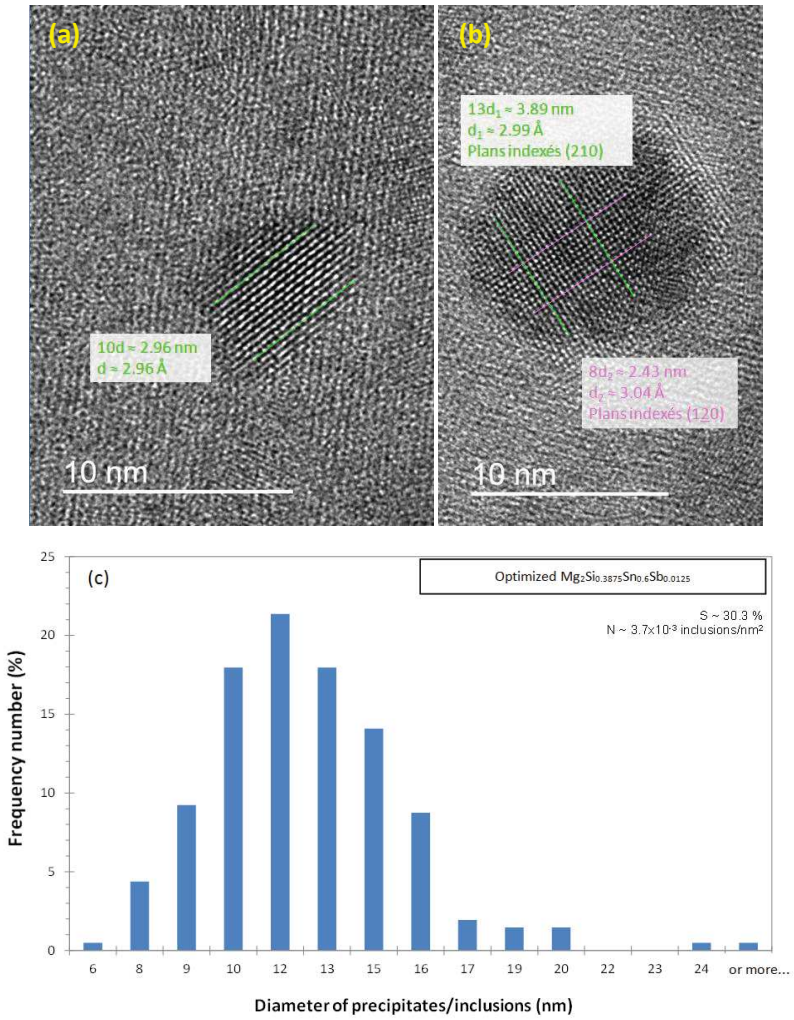

Figure 4.6: *HRTEM pictures of precipitates/inclusion and their size distribution in optimized $Mg_2Si_{0.3875}Sn_{0.6}Sb_{0.0125}$.*

An EDS analysis in map mode (figure 4.7) of a chosen area shows that bright precipitates/inclusions are enriched in Sn and impoverished in Mg, in respect to the surrounding material. The silicon content is more or less the same throughout the zone of interest. The global Sb content is lower than the target one. Indeed, the chemical composition of the selected area shown on figure 4.7 is $Mg_{1.999}Si_{0.414}Sn_{0.578}Sb_{0.009}$ (see table 4.1) against $Mg_2Si_{0.3875}Sn_{0.6}Sb_{0.0125}$ for the target composition.

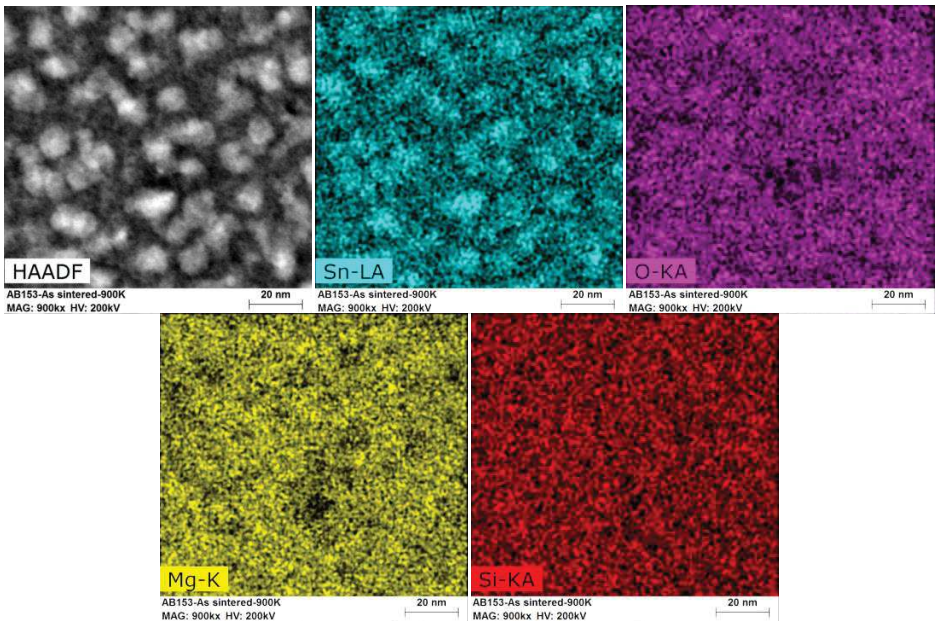

Figure 4.7: *EDS analysis of a targeted area.*

Element	Series	[norm. wt. %]	target comp. at %	[norm. at. %]	error in wt. %
Magnesium	K-Series	37.41	66.67	66.65	1.15
Silicon	K-Series	8.95	12.92	13.79	0.05
Tin	K-Series	52.79	20	19.26	1.64
Antimony	K-Series	0.85	0.41	0.3	0.07

Table 4.1: *Chemical composition from the EDS analysis of the whole area shown on figure 4.7.*

Figure 4.8 shows different local zones of interest, with the corresponding compositions shown on the table next to the HAADF image. The average composition of bright precipitates/inclusions (blue color) is $Mg_{1.944}Si_{0.406}Sn_{0.650}$. Surrounding material (red color) has the composition of $Mg_{2.029}Si_{0.422}Sn_{0.549}$.

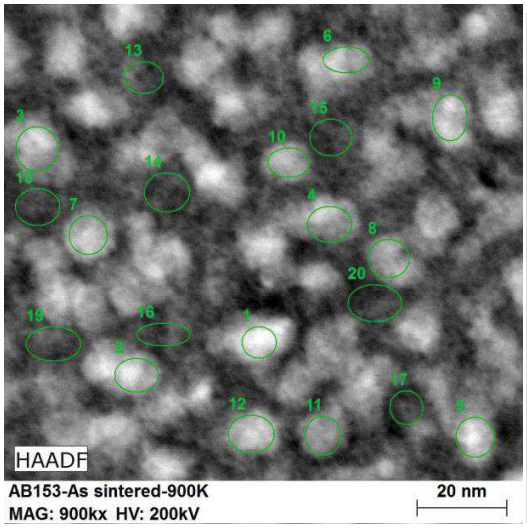

Spectrum	Mg-K (at %)	Si-KA (at %)	Sn-KA (at %)
1	61.91	13.31	24.78
2	64.63	13.69	21.68
3	63.62	13.27	23.11
4	62.16	14.02	23.83
5	65.68	14.52	19.80
6	65.01	13.99	21.00
7	66.75	13.72	19.54
8	65.91	13.31	20.78
9	65.47	12.98	21.55
10	64.67	13.02	22.30
11	66.34	13.81	19.85
12	65.38	12.89	21.73
13	67.61	13.82	18.57
14	68.93	14.36	16.71
15	67.49	13.60	18.91
16	68.97	14.34	16.69
17	67.36	13.74	18.90
18	65.91	14.79	19.29
19	66.17	13.93	19.90
20	68.57	13.85	17.58
Moyenne	**64.79**	**13.54**	**21.66**
ET	1.53	0.49	1.63
Moyenne	**67.63**	**14.05**	**18.32**
ET	1.17	0.40	1.19

Figure 4.8: *STEM/HAADF/EDS - Difference in composition between the matrix (red) and the precipitates/inclusions (blue).*

4.2.3 Thermoelectric properties

Thermoelectrical properties were investigated similarly as it was previously described in Chapter 3. Figure 4.9 shows the variations of electrical conductivity, Seebeck coefficient, power factor and thermal conductivity in function of temperature for the optimized material in comparison to the non-optimized one and also in comparison to results from the literature.

A carrier concentration of 1.5×10^{20} carriers/cm^3 is measured at room temperature for the optimized material against 1.9×10^{20} carriers/cm^3 (26 % lower) for the non-optimized one. Carrier mobility is determined to be around 66 cm^2/Vs for the optimized material which is a 69% increase over the non-optimized one.

In table 4.2 are summarized the difference in parameters of prime importance concerning the microstructure and the thermoelectric properties of the non-optimized and optimized materials.

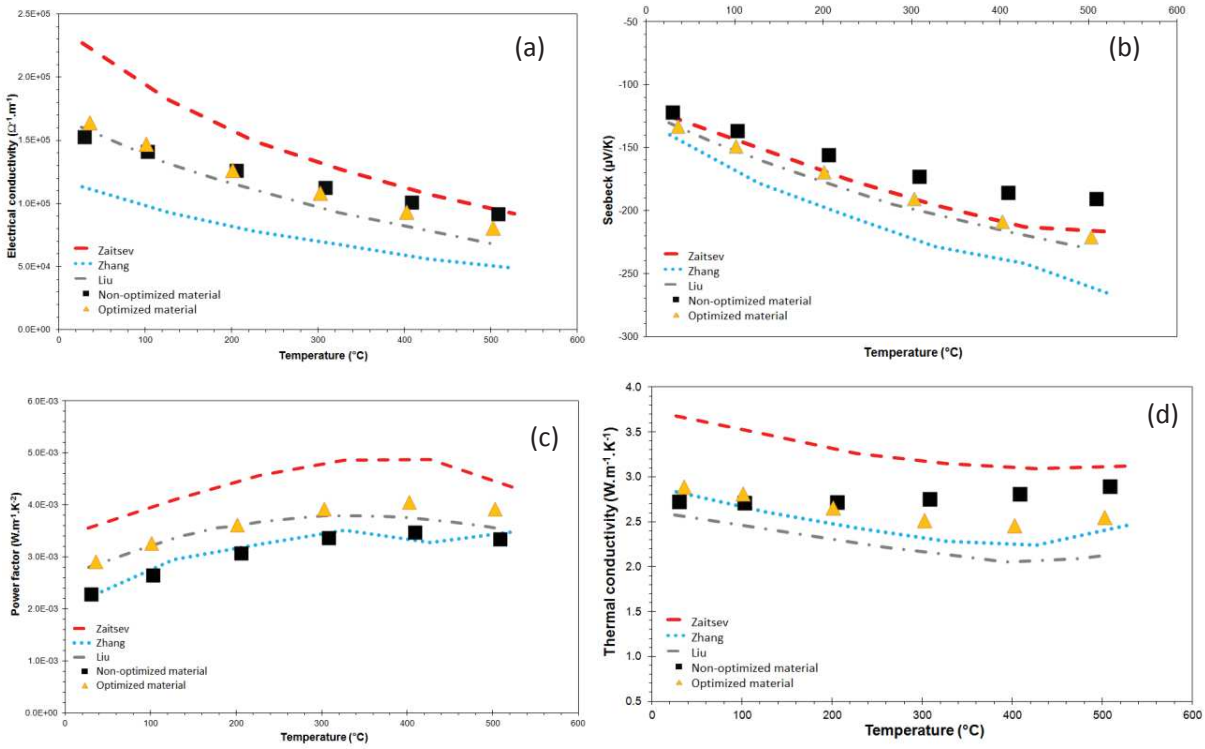

Figure 4.9: *Thermoelectric properties in function of temperature measured on the optimized as-sintered material and comparison to results from the literature and to what has been measured on the non-optimized material. (a) electrical conductivity; (b) Seebeck coefficient; (c) power factor; (d) thermal conductivity.*

Figure 4.9a shows that the electrical conductivity of the optimized material is slightly below the one of the non-optimized material above 100 °C. In the same time, the Seebeck coefficient is significantly higher for the optimized material in comparison to the non-optimized one (figure 4.9b), whatever the temperature of interest is. The carrier mobility is the same for both materials, but the carrier concentration is 60 % lower in the optimized material. The Seebeck coefficient is inversely proportional to the carrier concentration. The electrical conductivity is proportional to the carrier concentration and to the carrier mobility. Accordingly, the results observed on figures 4.9a and 4.9b are logical. It is interesting to point out that the grain size of the optimized material is, at least, 36% higher than the one of the non-optimized material. It is then concluded that, at this grains size scale, the concentration of grain boundaries in the sintered polycrystal has not a drastic influence on the displacement of the main carriers.

For all the temperature range of interest, the power factor is higher for the optimized material (figure 4.9c) and its variation in function of temperature is now similar to the one reported by Liu on the material he investigated.

Sample	Non-optimized material	Optimized material
Grain size (nm)	450	More than 610 (≥+36%)
Precipitates/inclusion concentration (/mm^2)	1.9×10^9	3.7×10^9 (+95%)
Average precipitate/inclusion diameter (nm)	13	12 (similar)
Chemical composition of the inclusions/precipitates (EDS)	$Mg_{1.83}Si_{0.39}Sn_{0.78}$	$Mg_{1.94}Si_{0.41}Sn_{0.65}$
Chemical composition of the surrounding material (EDS)	$Mg_{2.01}Si_{0.42}Sn_{0.57}$	$Mg_{2.03}Si_{0.42}Sn_{0.55}$
Carriers concentration (/cm^3)	1.9×10^{20}	1.5×10^{20} (-26%)
Carriers mobility (cm^2/Vs)	39	66 (+69%)

Table 4.2: *Comparison of different features for non-optimized and optimized material*.

The variation of the thermal conductivity in function of temperature is somewhat different for the optimized material in comparison to the non-optimized one (figure 4.9d). From a general point of view, the thermal conductivity is lower for the optimized material above 100 °C. More than that, the thermal conductivity decreases above 200 °C for the optimized material, while the value for the non-optimized material increases. The curve shape of the optimized material follows the ones obtained by Zaitsev, Liu and Zhang on the materials they investigated.

The electronic and lattice contributions to the total thermal conductivity of the materials of interest are shown on figure 4.10. Above 200 °C, both contributions are lower for the optimized material. Even if the average size of the inclusions/precipitates that are homogeneously dispersed in the sintering microstructure is similar for both materials, it is critical to point out that the optimized material contains around 95% more of such microstructural events. Then, phonons propagation is more disturbed in the optimized material, which leads to lower values of the lattice contribution. In the same time, for similar carrier mobility, the carrier concentration is 60% lower for the optimized material. Accordingly, the electronic contribution to the thermal conductivity is lower for the optimized material. It is also

interesting to observe that the grain size of the sintered material has not a strong importance on the thermal conductivity, at least in this grain size range. Indeed, the optimized material exhibits a grain size at least 36 % higher than the one of the non-optimized material. If the grains size is a first-order parameter regarding the thermal conductivity, this parameter should be higher for the optimized material, which is clearly not the case.

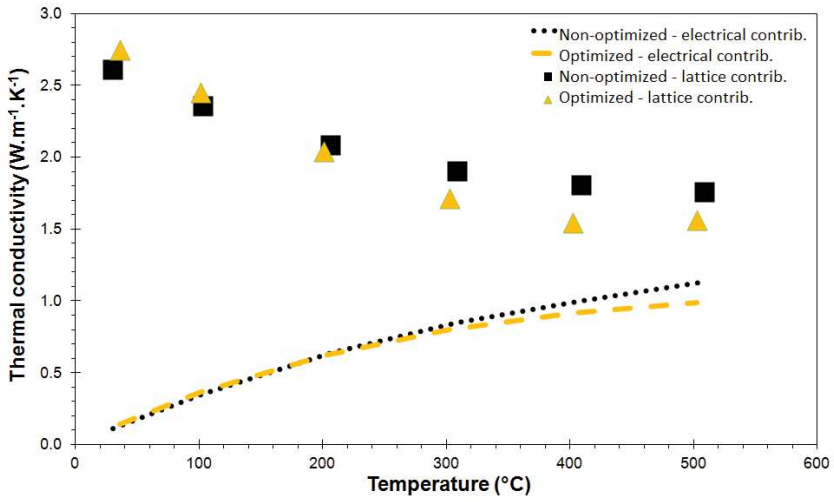

Figure 4.10: *Different contribution to thermal conductivity for the materials of importance.*

Finally, the figure of merit of the optimized material is shown on figure 4.11. A maximum ZT of 1-11.2 is obtained between 400 and 500 °C.

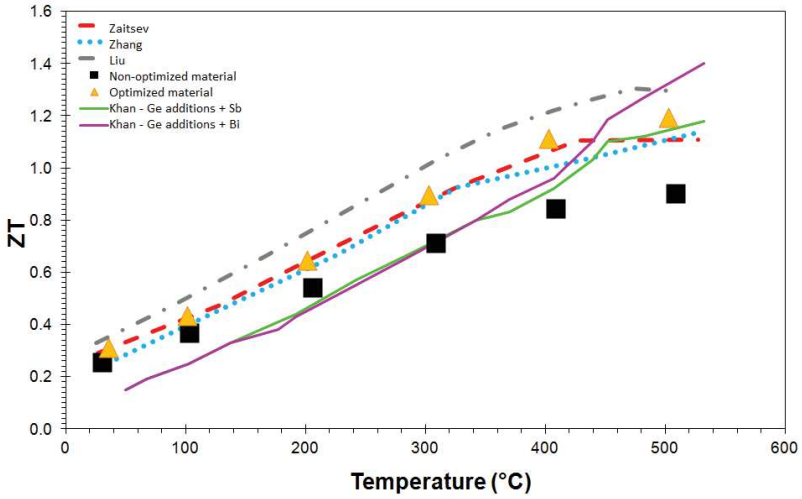

Figure 4.11: *Thermoelectric figure of merit (ZT) in function of temperature.*

Such values are on par with Zaitsev [38,39], Zhang [114], Khan [104] but are still a little bit lower than what was measured by Liu [44]. When compared to Khan [104], who added Ge in the formulation he investigated and used Bi as an n-type dopant, the ZT parameter we obtained with our optimized material is better in the 20-450 °C temperature range. Finally, in comparison to the literature, the main advantage of our material is that it was fabricated using only two simple steps: mechanical-alloying followed by spark plasma sintering.

We performed additional developments to try to increase as much as possible the ZT parameter of our material for temperatures ranging from 20 to 500 °C. The first way was to evaluate the influence of a small volume fraction of nanoparticles added to the generic $Mg_2Si_{0.3875}Sn_{0.6}Sb_{0.0125}$ material formulation as described in the following paragraphs.

4.3 $Mg_2Si_{0.3875}Sn_{0.6}Sb_{0.0125}$ with Half-Heusler additions

4.3.1 Introduction

The specificity of Half-Heusler (HH) compounds is that their band gap can be tailored by changing their chemical composition. HH have a band gap in the range of 0-1.1 eV, which is suitable for moderate temperature thermoelectric applications [119,120,121]. Nonetheless, a major disadvantage for thermoelectric application of Half-Heusler compounds is their high thermal conductivity (6.7 – 20 $Wm^{-1}K^{-1}$) [122,123,124,125].

Theoretical calculations (Natalio Mingo, unpublished results) have shown that adding a small volume fraction of different kinds of HH nanoparticles, in a polycrystalline Mg-Si-Sn alloy, could be a way to increase the ZT parameter by a drastic reduction of the thermal conductivity (phonons propagation is disturbed because of the nanometer-sized inclusions). For our investigations, we have chosen nanoparticles of the MgCuSn Half-Heusler (HH) phase because its lattice parameter of 6.224 Å (JCPDS reference file 04-001-5603) is matching quite well with the one of the $Mg_2Si_{0.4}Sn_{0.6}$ matrix which lattice parameter is 6.580 Å (JCPDS reference file 01-089-4254).

4.3.2 Material

We obtained the Half-Heusler MgCuSn powder from “Johnson Matthey PLC”. It was synthesized by mechanical alloying in an inert (argon) atmosphere. The powder is aggregated (soft ones) and the elemental crystallites have an average size of 25 nm. Constituents to prepare an n-type $Mg_2Si_{0.3875}Sn_{0.6}Sb_{0.0125}$ powder were placed in a zirconia jar (500 ml), with 10 mm zirconia jar (BPR is 24), together with 1.7 vol.% of MgCuSn as-received nanoparticles. The yield, at first, was lower than expected, even with the addition of 1% cyclohexane (about 15 grams

out of 25 grams – 60%). Adding 3 wt% of cyclohexane increased the yield (to 20 grams – 80%) while small amount of residue was still present at the bottom of the jar.

XRD data on the collected aggregated powder manufactured with 3 wt% cyclohexane are shown in figure 4.11.

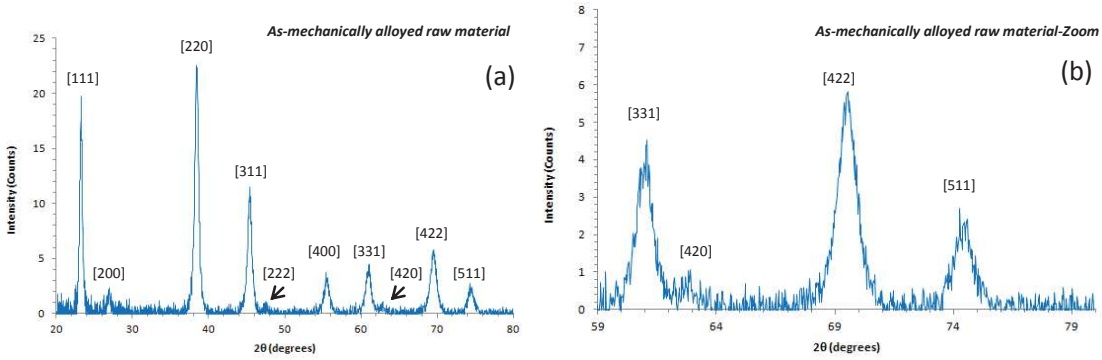

Figure 4.11: *XRD spectra on the as-mechanically alloyed raw powder with Half-Heusler nanoparticles addition: (a) Complete spectrum; (b) Zoom on the high diffraction angle values*.

As before, the alloyed powder exhibits only peaks that match quite well with the $Mg_2Si_{0.4}Sn_{0.6}$ phase. These peaks do not show any asymmetric profile even for the high diffraction angle values. The XRD pattern was treated with the Williamson-Hall method [105] showing that the aggregate is composed of elemental crystallites with an average diameter around 32 nm. No peaks related to MgCuSn HH compound are detected.

4.3.3 Sintering

We have again used the Spark Plasma sintering method to consolidate our $Mg_2Si_{3.875}Sn_{0.6}Sb_{0.0125}$ alloyed powder with 1.7 vol. % of MgCuSn addition. We used the same optimized conditions, as exposed previously in this chapter. The relative density of the as-sintered sample is calculated to be 99.6 %.

Figure 4.12a and b show the XRD pattern that was acquired on the as-sintered sample. Although the peaks match the $Mg_2Si_{0.4}Sn_{0.6}$ phase, it is obvious that peaks at higher angles are not symmetrical anymore, as it was also observed on the other materials investigated before in Chapter 3 and 4.

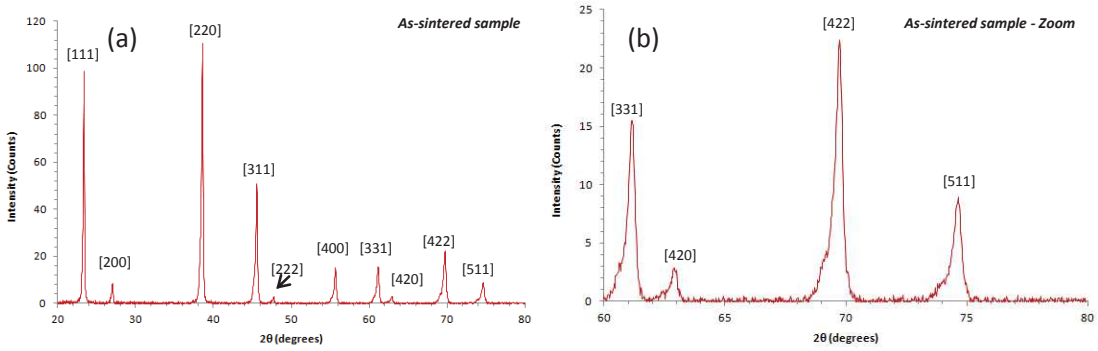

Figure 4.12: *XRD spectra on the as-sintered sample with half-Heusler additions: (a) Complete spectrum; (b) Zoom on the high diffraction angle values.*

Treating the XRD pattern with TOPAS software and using the Williamson – Hall method [105] gives an average grains size of 520 nm for the as-sintered material. As it was the case for the raw powder, we did not observe any peak linked to the MgCuSn HH phase.

4.3.4 Post–sintering microstructure investigations

A deep investigation of the as-sintered microstructure was performed. A thin foil was created from the central zone of the pellet using focus ion beam (FIB). Afterwards, the foil is mounted on a TEM apparatus (minimization of the time where the foil is in direct contact with ambient air).

TEM observations in bright field mode show that individual grains are polyhedrons (figure 4.13a). The grain size distribution is shown on figure 4.14. An averaged grain size around 520 nm is measured, which is in good agreement with the value obtained from XRD experiments. A lamellar second phase is also detected (figure 4.13a, pink ellipse). Most of the lamellas appear to be concentrated in the vicinity of grain boundaries (figure 4.13b, 4.13c, purple arrows) and 4.13d. The as-sintered material is also devoted of any residual porosity related to poor sintering. Nonetheless, some pores exhibiting a diffusive aspect are observed and are connected to strong oxidation areas (green doted ellipses in figures 4.13a (TEM mode) and 4.13c (HAADF mode)) homogeneously dispersed in the sintering microstructure. As shown on Figure 4.13b a high number of bright nodules (TEM mode) are entrapped in most of the elemental grains constituting the sintered polycrystal. Such nodules are seen grey in HAADF mode (figure 4.13c) and local EDS analyses shown that they are made of an oxide-based compound. Finally, in most of the elemental grains and at grain boundaries are also observed (different tilting conditions are possibly needed from one grain to another one for imaging) the same kind of precipitates/inclusions (bright color in HAADF mode) as the ones described before

in Chapter 3 and in the paragraphs before this one in this chapter (figure 4.13c, yellow doted ellipse).

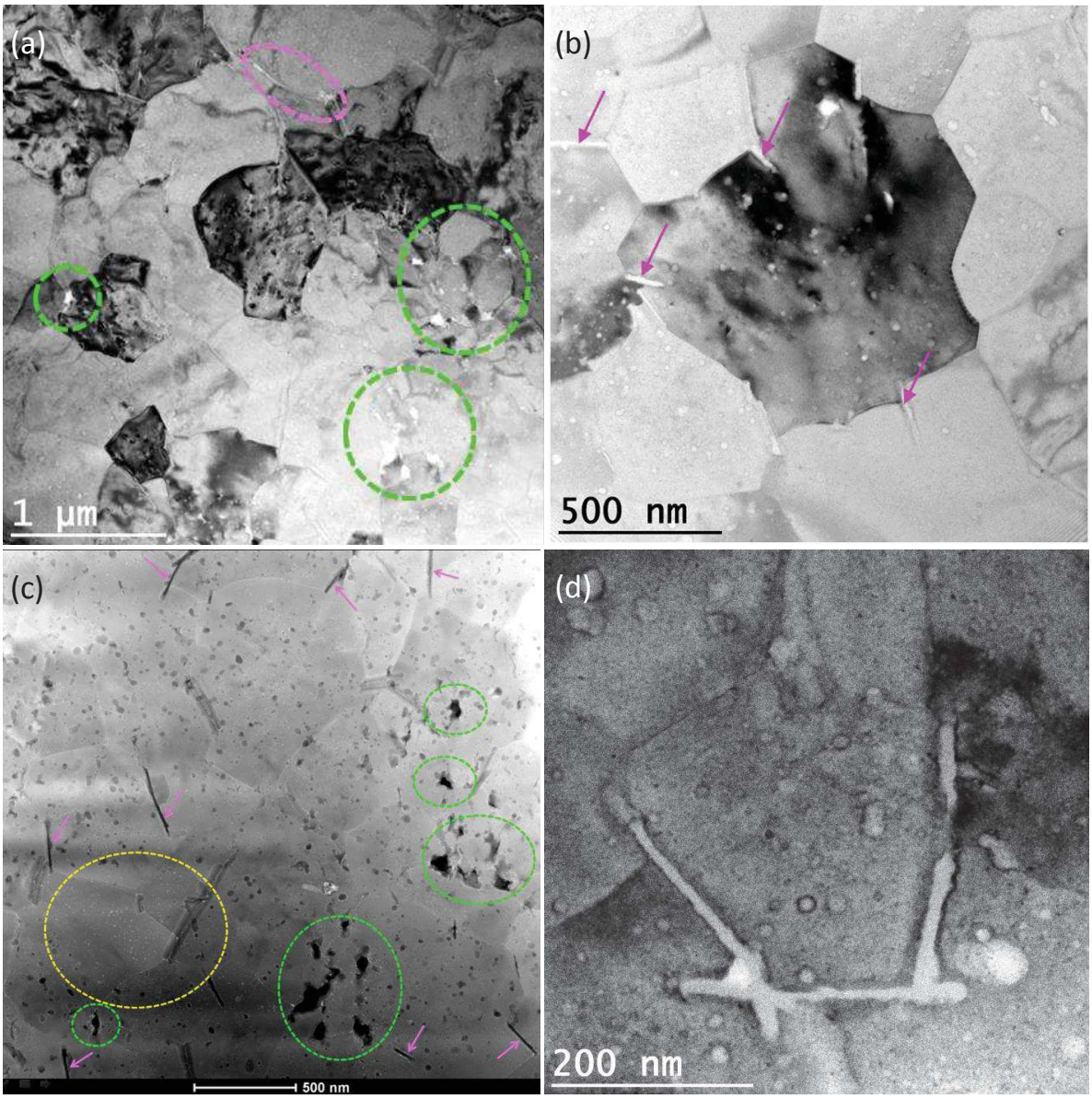

Figure 4.13: *Microstructure of the as-sintered material: a) TEM bright field – porosities connected to oxidation areas (green circles) and lamellar second-phase (pink ellipse); b) TEM bright field – lamellar phases in the vicinity of grain boundaries (purple arrows) and bright nodules in intragranular position; c) STEM/HAADF – overview with many white intragranular precipitates/inclusions (yellow ellipse), lamellar second-phase (pink arrows) and porosities conneceted to oxidation areas (green ellipses); d) TEM bright field – lamellar second-phase located at grain boundaries.*

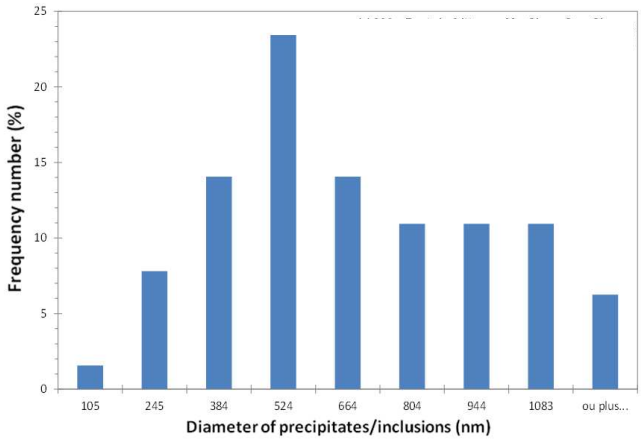

Figure 4.14: *Grain size distribution of the optimized $Mg_2Si_{0.3875}Sn_{0.6}Sb_{0.0125}$ material with 1.7 vol.% MgCuSn.*

Figure 4.15 shows detailed images of the small precipitates/inclusions which are homogeneously distributed in the bulk of the elemental grains and grain boundaries, a already shown in figure 4.13c (doted grey ellipse). In STEM/HAADF they do appear bright, which proves that they are made out of heavy elements (most probably tin). On the other hand, the same dark/ grey nodules as the ones shown in figure 4.13c, made out of light elements, are also observed (figure 4.15a). Thusly, they are most probably oxide-based compounds. Tilting of the thin foil under the electron beam, the contrast of precipitates/inclusions was changing, which showed their crystalline nature.

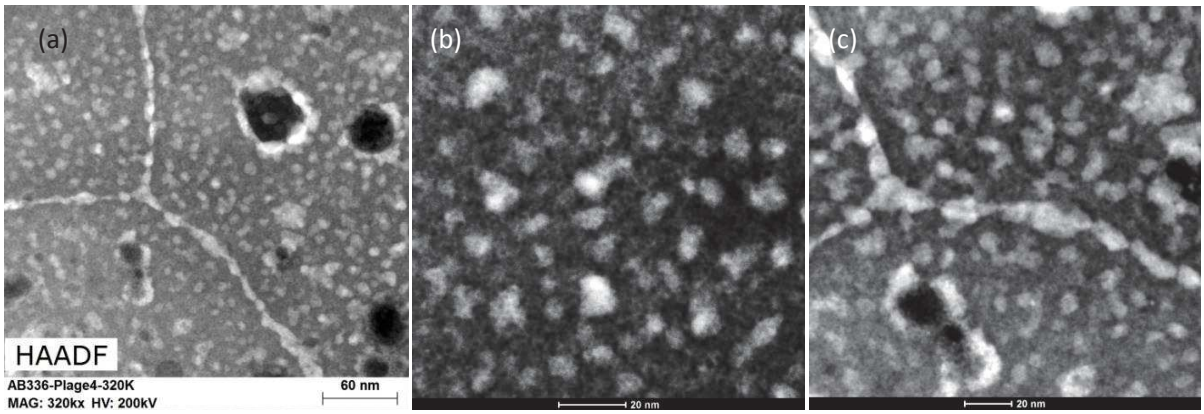

Figure 4.15: *STEM/HAADF images of dark nodules and bright precipitates/inclusions concentrated in the grains and at the grain boundaries.*

An EDS analysis in map mode is represented in figure 4.16 for an area of interest that contain precipitates/inclusions. Clearly, the bright precipitates/inclusions are enriched in Sn and poor in Mg. when compared to the surrounding matrix, as it was previously reported for the materials investigated in Chapter 3 and in the previous paragraph of this chapter. The silicon content is constant throughout the zone of interest. In table 4.3 we can see the average chemical composition of this zone. The chemical composition of the chosen area is $Mg_{1.999}Si_{0.428}Sn_{0.561}Sb_{0.012}$ against the $Mg_2Si_{0.3875}Sn_{0.6}Sb_{0.0125}$ for the target composition. Then the Sb doping level is very close to the desired one.

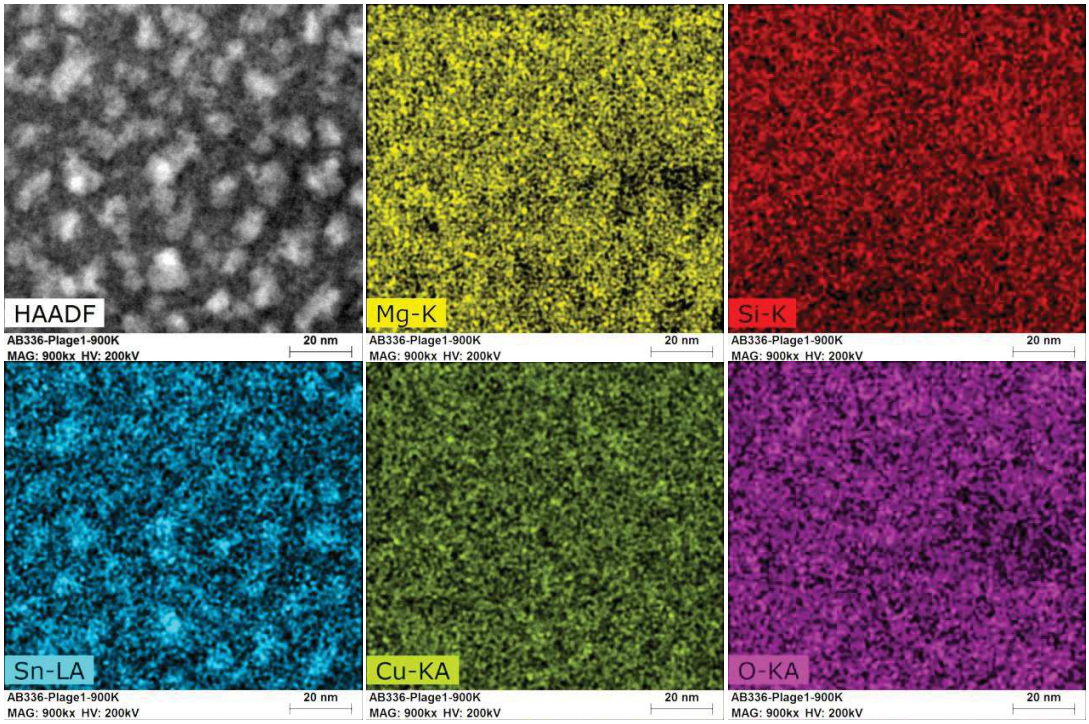

Figure 4.16: *STEM/HAADF/EDS analysis of a targeted area.*

Element	Series	[norm. Wt. %]	target comp. at %	[norm. at. %]	Error in wt. %
Magnesium	K-series	37.78	66.67	66.65	1.16
Silicon	K-series	9.34	12.92	14.26	0.05
tin	K-series	51.76	20	18.7	1.61
antimony	K-series	1.13	0.41	0.4	0.09

Table 4.3: *Chemical composition from the EDS analysis of the whole area shown on figure 4.18.*

We have chosen different areas to see the difference in composition between the matrix (dark areas) and the bright precipitates/inclusions detected using the HAADF mode, as it can be seen on figure 4.17. Figure 4.17 shows different local zones of interest, with the corresponding compositions shown on the table in the same figure. The average composition of bright precipitates/inclusions (blue color) is $Mg_{1.926}Si_{0.415}Sn_{0.659}$. Surrounding material (red color) has the composition of $Mg_{2.046}Si_{0.430}Sn_{0.524}$.

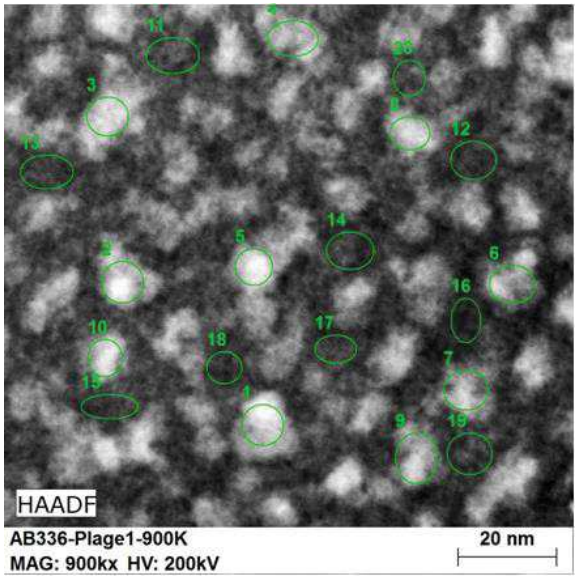

Spectrum	Mg-K (at %)	Si-KA (at %)	Sn-KA (at %)
1	63.74	13.02	23.24
2	64.45	14.29	21.26
3	64.34	13.79	21.87
4	65.42	14.32	20.26
5	65.70	12.97	21.33
6	62.15	15.02	22.83
7	64.94	13.99	21.06
8	64.45	14.48	21.07
9	63.03	13.24	23.72
10	63.75	13.09	23.16
11	67.83	13.67	18.50
12	67.82	15.13	17.05
13	68.39	14.97	16.64
14	69.04	14.31	16.65
15	69.10	13.59	17.31
16	68.30	14.45	17.25
17	68.52	14.70	16.77
18	68.43	13.95	17.62
19	67.21	13.97	18.82
20	67.35	14.51	18.13
Moyenne	**64.20**	**13.82**	**21.98**
ET	1.08	0.72	1.17
Moyenne	**68.20**	**14.33**	**17.48**
ET	0.64	0.53	0.78

Figure 4.17: *STEM/HAADF/EDS - Difference in composition between the matrix (red) and the precipitates/inclusions (blue).*

Using image analyses from TEM pictures, the size distribution for the bright precipitates/inclusions and the grey nodules that are observed (HAADF mode) throughout the as-sintered microstructure are shown on figures 4.18a and 4.18b, respectively. An average diameter of 10 nm and a concentration of $4.3x10^{-3}/nm^2$ are obtained for the precipitates/inclusions. An average diameter of 16 nm and a concentration of $9.0x10^{-4}/nm^2$ are obtained for the grey nodules.

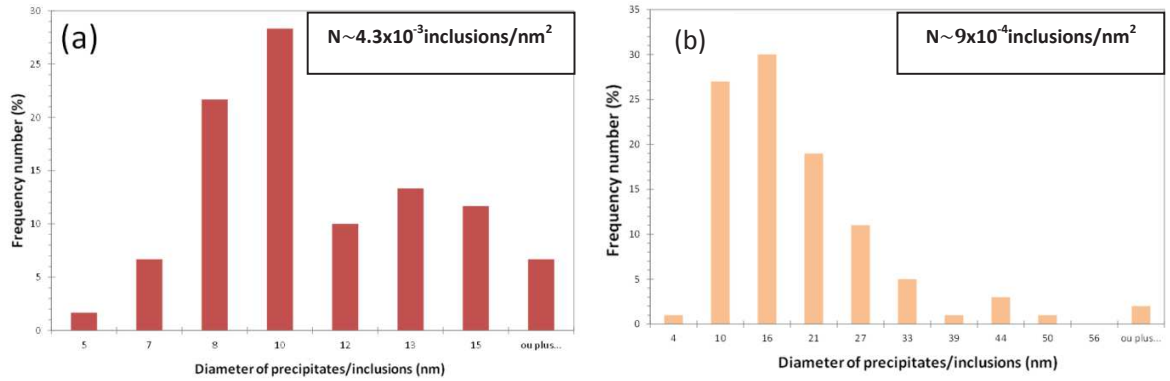

Figure 4.18: *Optimized $Mg_2Si_{0.3875}Sn_{0.6}Sb_{0.0125}$ material with 1.7 vol.% MgCuSn. Size distribution of: a) precipitates/inclusions; b) oxide-based nodules.*

An EDS analysis in map mode (figure 4.19) on a chosen area that contain the lamellar second-phase located at a grain boundary is shown on figure 4.11. It is evident that the grey nodules are made of an oxide-based material. In comparison to the surrounding material, it is critical to note that the lamellar second-phase is strongly enriched in Si and depleted in any of the other elements.

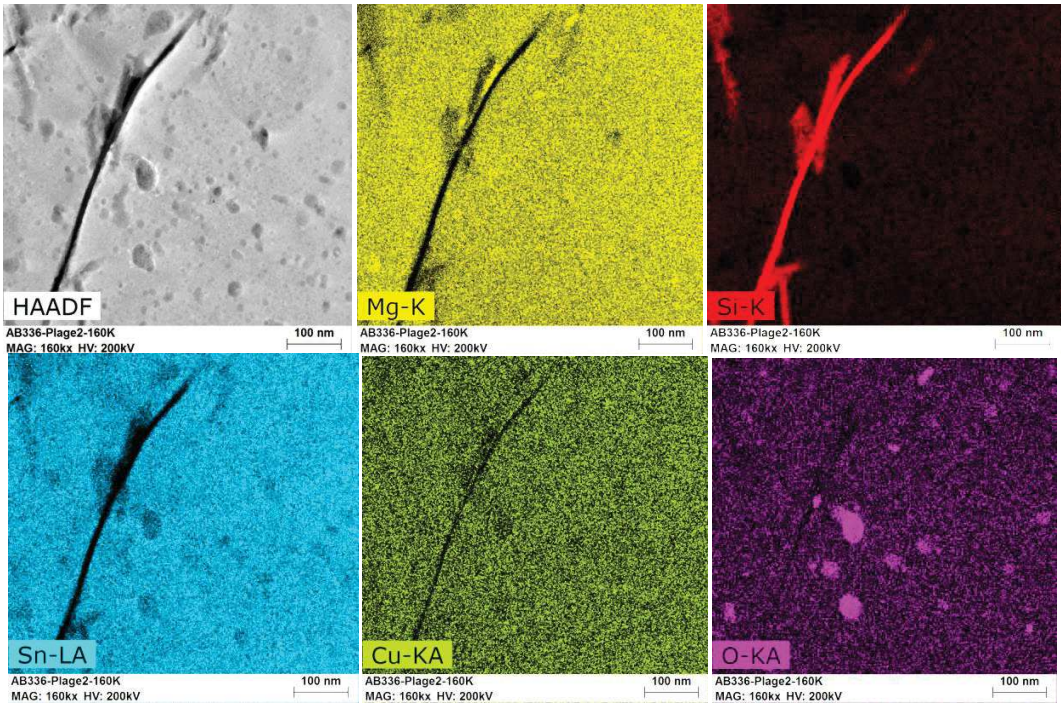

Figure 4.19: *Nodules of oxide and silicon rich lamellar second-phase.*

Additional observations were done using the HRTEM mode on an interface between the lamellar second-phase and the surrounding matrix (figure 4.20). Lattice fringes are observed in the matrix (figure 4.20a). The inter-fringe distance for optimized $Mg_2Si_{0.3875}Sn_{0.6}Sb_{0.0125}$ material with 1.7 vol.% MgCuSn is 3.81 Å. It is in good agreement to the inter-planar distance for the {111} orientation of $Mg_2Si_{0.4}Sn_{0.6}$ (3.80 Å). The lattice parameter of the cubic cell of the matrix is then calculated to be 6.592 Å. Then, using the Vegard's law, we can find that the matrix composition of the as-sintered material is $Mg_2Si_{0.41}Sn_{0.59}$ which matches well with the target composition. Additionally, it is interesting to observe that the FFT of the image selected in the lamellar second-phase (presented by the yellow square on figure 4.20a) exhibits the typical aspect of an amorphous material (figure 4.20b). Thusly, the lamellar second phase that is homogeneously dispersed in the sintered materials results probably from local melting/degradation of the material during sintering. The high cooling rate used at the end of the soak prevents its crystallization.

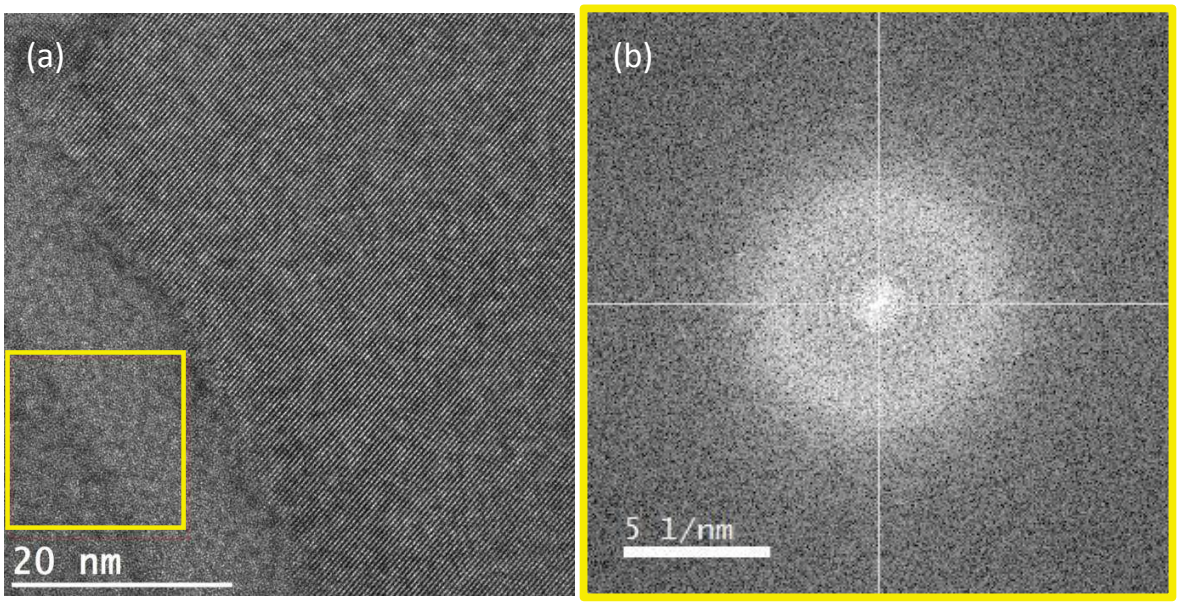

Figure 4.20: *HRTEM image of a) matrix lattice fringes and amorphous silicon rich phase; b) Fast Fourier transformation (FFT) of the amorphous Si phase.*

Finally, an additional EDS analysis in map mode is shown in figure 4.21. It appears that the precipitates located at grain boundaries are enriched in Sn/Cu and are impoverished in Mg in comparison to the surrounding material. This is true also some precipitates that are in intragranular position, located at the vicinity of oxide-based nodules. Nevertheless, it was not possible to know if such precipitates are made of the native MgCuSn HH phase. But at least, part

of the Cu element, initially contained in the added nanoparticles of HH, is still combined to Sn and segregate at most of grain boundaries.

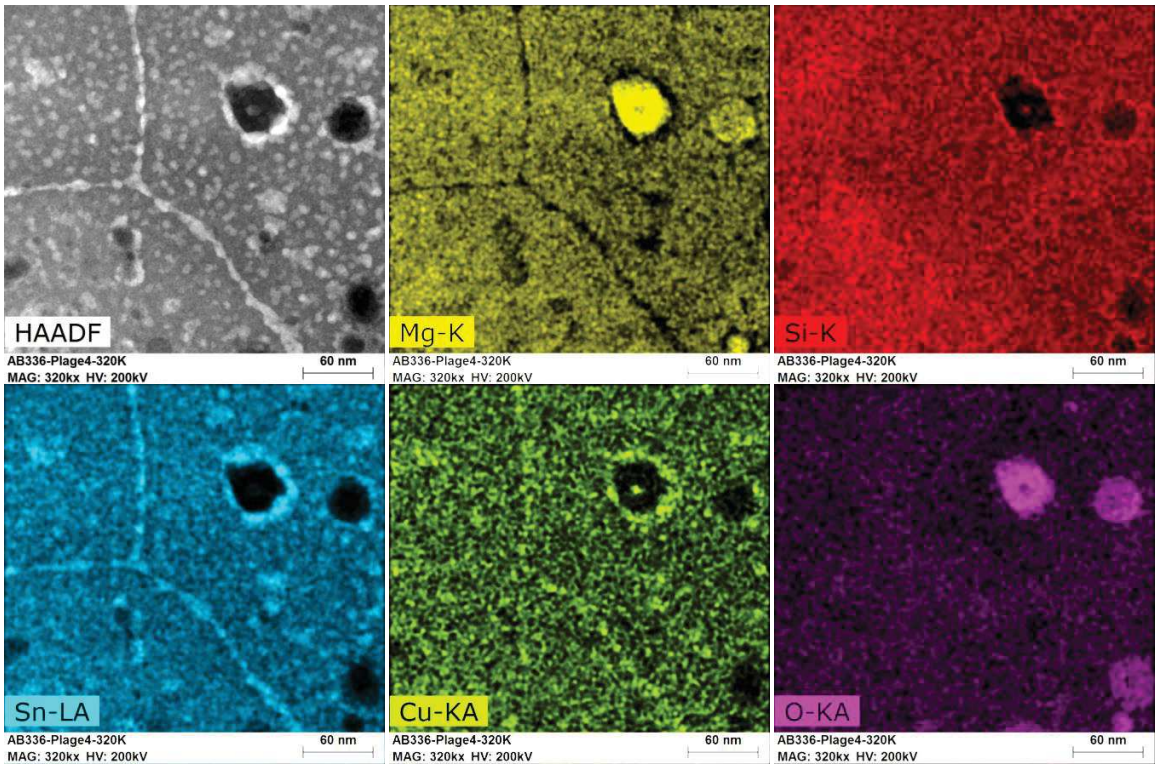

Figure 4.21: *STEM/HAADF/EDS of grain boundaries and oxide nodules.*

4.3.5 Thermoelectric properties

Thermoelectric properties were investigated similarly as it was previously described. Figure 4.22 shows the variations of electrical conductivity, Seebeck coefficient, power factor, and thermal conductivity in function of temperature for the optimized material with HH nanoparticles, in comparison to the non-optimized and optimized material we previously investigated. Results from the literature are also included.

Additionally, a carrier concentration of 1.7×10^{20} carriers/cm^3 is measured at room temperature for the material with HH nanoparticles against 1.5×10^{20} carriers/cm^3 (13 % higher, so the values are similar) for the optimized one. The carrier mobility for the material that contains HH nanoparticles is determined to be 77 cm^2/Vs, which is 16 % higher than the one for the optimized material.

In table 4.4 are summarized the differences in parameters of prime importance concerning the microstructure and the thermoelectric properties of the non-optimized and optimized materials and the ones for the material that contain HH nanoparticles.

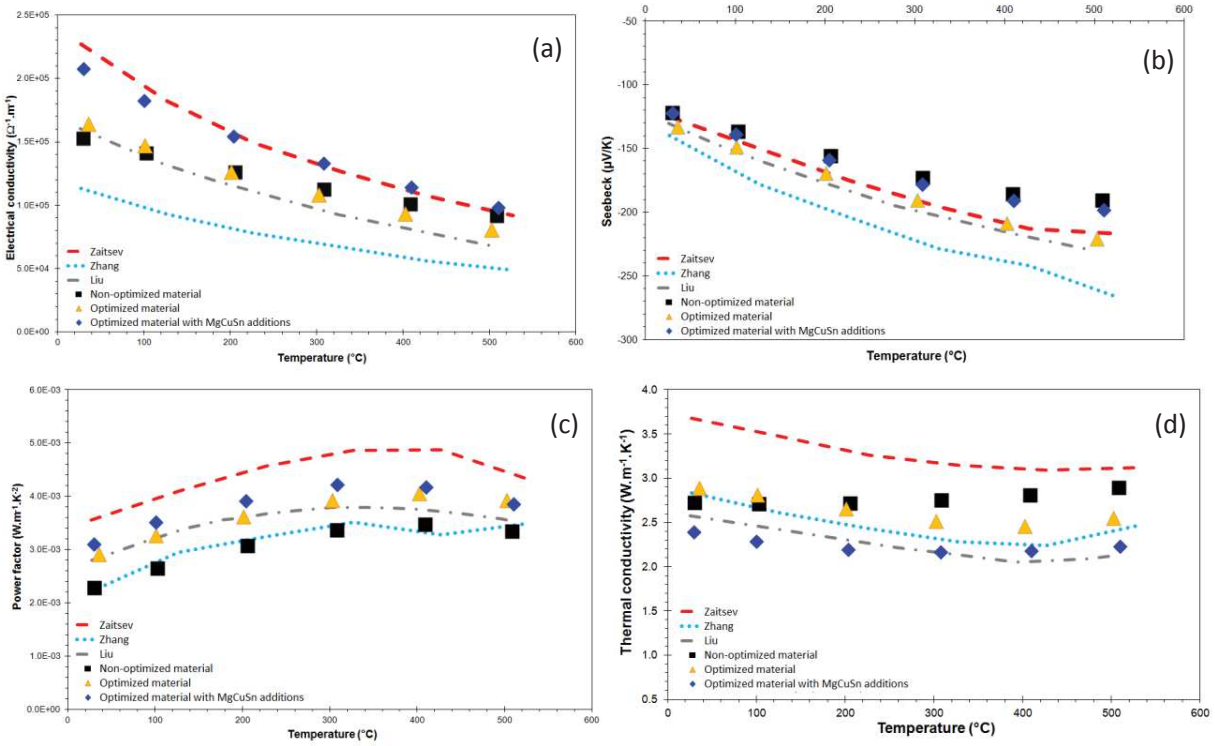

Figure 4.22: *Thermoelectrical properties in function of temperature measured on the as-sintered sample made from powder synthesized by MA: (a) electrical conductivity; (b) Seebeck coefficient; (c) power factor; (d) thermal conductivity*.

Figure 4.22a shows that the electrical conductivity of the optimized material with HH nanoparticles is significantly above the one of the optimized material, in all the temperature range of interest. Whatever the temperature of interest is, figure 4.22b shows that the Seebeck coefficient is significantly lower for the optimized material with HH in comparison to the optimized one and is close to what was reported on the non-optimized material. In comparison to the optimized material, the carrier mobility is 16% higher for the material with HH nanoparticles for the same carrier concentration and an average grain size slightly lower (-14%). The Seebeck coefficient is inversely proportional to the carrier concentration. The electrical conductivity is proportional to the carrier concentration and to the carrier mobility. Accordingly, the results observed on figures 4.22a and 4.22b are easy to interpret. It is postulated that the

incorporation of the HH nanoparticles into the formulation has an impact of the band structure of the sintered material..

For all the temperature range of interest, the power factor is the highest for the optimized material where HH nanoparticles have been added (figure 4.22c).

Sample	Non optimized material	Optimized material	Optimized material with HH additions
Grain size (nm)	450	More than 610	524 (-14%)
Precipitates/inclusion concentration (/mm^2)	1.9×10^9	3.7×10^9	4.3×10^9 (+16 %) 0.9×10^9 (oxides) (+41% in total)
Average precipitate/inclusion diameter (nm)	13	12	10 16 (oxides)
Chemical composition of the inclusions/precipitates (EDS)	$Mg_{1.83}Si_{0.39}Sn_{0.78}$	$Mg_{1.94}Si_{0.41}Sn_{0.65}$	$Mg_{1.93}Si_{0.42}Sn_{0.66}$ oxide
Chemical composition of the surrounding material (EDS)	$Mg_{2.01}Si_{0.42}Sn_{0.57}$	$Mg_{2.03}Si_{0.42}Sn_{0.55}$	$Mg_{2.05}Si_{0.43}Sn_{0.52}$
Carriers concentration (/cm^3)	1.9×10^{20}	1.5×10^{20}	1.7×10^{20} (+13 %)
Carriers mobility (cm^2/Vs)	39	66	77 (+16%)

Table 4.4: *Comparison of different features for non-optimized, optimized and optimized material with Half-Heusler nanoparticles addition.*

The variation of the thermal conductivity in function of temperature is different for the optimized material with HH addition in comparison to the optimized one (figure 4.22d). Generally, the thermal conductivity is lower at all temperatures.

The electronic and lattice contributions to the total thermal conductivity of the materials of interest are shown on figure 4.23. Phonon propagation is disturbed by a high level of nanometer-sized precipitates/inclusions homogeneously dispersed in the microstructure. Thusly, due to a raise of 41 % of the concentration of nanometer-sized precipitates/inclusions (including the oxide-based ones) present in the sintered microstructure, the optimized material with HH additions exhibits lower values of the lattice contribution to the thermal conductivity in all the temperature range investigated. In the same time, because of its especially high electrical

conductivity in the 20-500 °C temperature range, the optimize material where HH nanoparticles were added presents the higher electronic contribution to the total thermal conductivity.

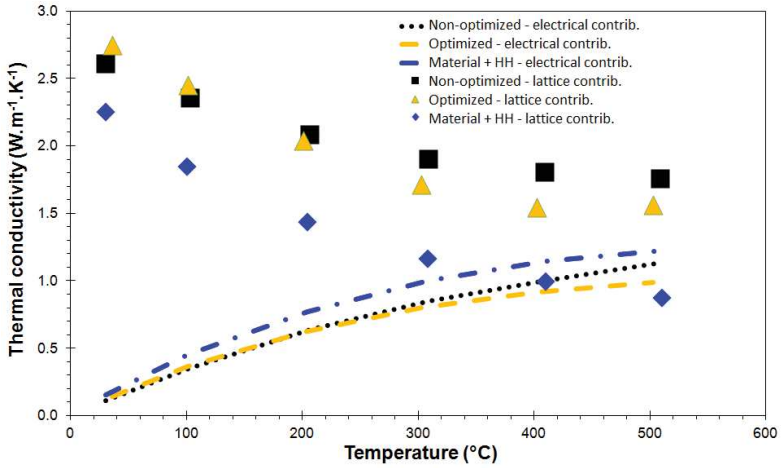

Figure 4.23: *Different contribution to thermal conductivity for the materials of importance.*

Finally, the dimensionless figure of merit of the optimized material with HH is shown on figure 4.24. A maximum ZT of 1.3-1.4 is obtained between 400 and 500 °C.

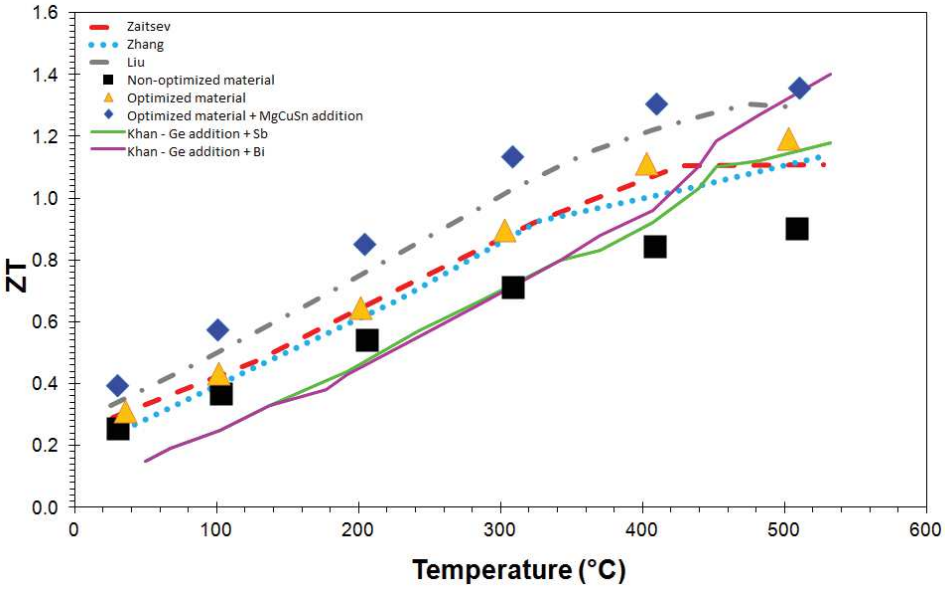

Figure 4.24: *Thermoelectric figure of merit (ZT) in function of temperature.*

4.4 Conclusion

In this chapter we have shown that tailoring the sintering conditions is an effective way for increasing the ZT parameter of an n-type $Mg_2Si_{0.3875}Sn_{0.6}Sb_{0.0125}$ thermoelectric material. A ZT value of 1.2 at 500 °C was obtained. Adding Half-Heusler nanoparticles to the $Mg_2Si_{0.3875}Sn_{0.6}Sb_{0.0125}$ matrix has been shown to be an effective way to further increase the ZT parameter. A value around 1.4 is then obtained at 500 °C. Such a value belongs to the highest one ever reported on that kind of material.

We have also clearly demonstrated that mastering the sintering microstructure is an important step to develop n-type Mg-Si-Sn materials having high ZT values. The size and concentration of nanometer-sized precipitates/inclusions/nodules, whatever their chemical composition, are key parameters to control, because they have a strong influence on the thermal conductivity. Even if the grain size should be also an important parameter, it appears as being a second order parameter for the grain size range of the materials we investigated.

The following chapter will provide some candidates for a p-type material, thusly completing the picture of n- and p-type silicides that can be used in the temperature range 300-600 °C for thermoelectric applications.

CHAPTER 5

P-type $Mg_2Si_{1-x}Sn_x$ and $MnSi_x$ materials

5.1 Introduction

In Chapter 3 and Chapter 4, we have exposed how it is possible to obtain an n-type $Mg_2Si_{1-x}Sn_x$ material that exhibits a particular microstructure enabling ZT values as high as 1.2 to 1.4 to be obtained in the temperature range 400-500 °C. Therefore, the next step is to develop a p-type Mg-Si-Sn material.

There have been many attempts to produce a p-type thermoelectric material based on Mg-Si-Sn. Aizawa [126] found out that below 200°C, undoped $Mg_2Si_{0.8}Sn_{0.2}$ alloy acts like a p-type material, and above 200 °C a p→n transition occurs. As we mentioned before (see Chapter 1, subchapter 1.3.3), Isoda [46] doped $Mg_{2.00}Si_{0.25}Sn_{0.75}$ with Ag (20000 ppm) and Li (5000 ppm) to create a p-type material, gaining a ZT value of 0.32 at 500 °C. Isoda also said that the stoichiometric decrease of Mg (from $Mg_2Si_{1-x}Sn_x$ to $Mg_{1.98}Si_{1-x}Sn_x$) can create a p-type material. The third variant is proposed by Ihou-Mouko [48] where he put Ge in the place of Sn atoms to obtain $Mg_2Si_{1-x}Ge_x$ alloys. Then, to increase the carrier concentration, he doped it with Ga, finally obtaining a p-type material with a ZT value of 0.36 at 377 °C. This last result is the best one reported for p-type Mg-Si-Sn and Mg-Ge-Sn formulations up to now.

These methods have a lot of problems tied to them. Aizawa's method leads to a material that is switching from n-type to p-type above 200°C. Isoda increased massively the price of the material he developed by introducing high doping concentrations of Ag and Li. Also lithium is not safe for manipulation, due to its corrosive nature and it also requires special handling. Ihou-Mouko's substitution of Sn atoms with Ge also highly increased the price of the raw material because the cost of Ge is high (around 1250 $/kg for 99.99 % purity).

This chapter will explain how $Mg_2Si_{1-x}Sn_x$ was doped with B in an effort to create a p-type alloy. The goal is to create a thermoelectrically compatible material with the n-type one, for easiness when these both materials will be introduced in real thermoelectrical modules. We will explain why B doping failed, which forced us to take an alternative route in finding a new p-type candidate. Then, the higher manganese silicides were our next choice. It has to be outlined that experimental results exposed hereafter are only preliminary ones because time was missing to complete a whole study.

5.2 P-type Mg-Si-Sn alloy doped with B

5.2.1 Raw powder of $Mg_2Si_{1-x-y}Sn_xB_y$ (x = 0.6; y = 0.0125, 0.02)

We have synthesized two powders having a composition of $Mg_2Si_{1-x-y}Sn_xB_y$ (x = 0.6; y = 0.0125, 0.02). Based on the valence atoms of B, we estimated that it may be a good candidate as a p-type dopant that will interchange with silicon atoms. After using the same milling conditions as before (explained in Chapters 2, 3 and 4) we obtained XRD patterns that are

similar for both compositions. The one related to the $Mg_2Si_{0.38}Sn_{0.6}B_{0.02}$ formulation is shown on figure 5.1.

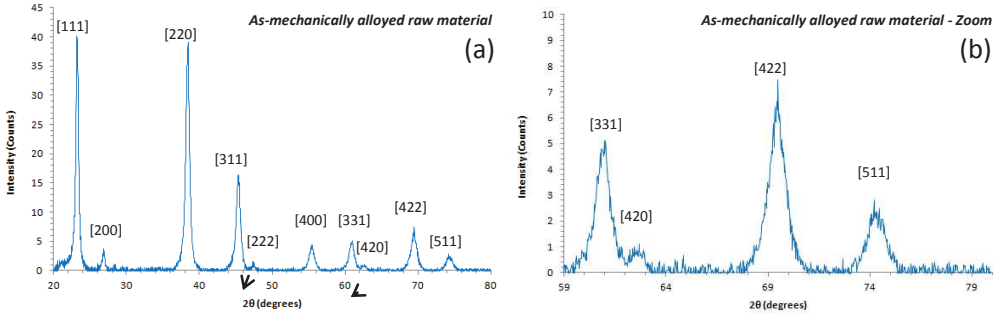

Figure 5.1: *XRD spectrum on $Mg_2Si_{0.38}Sn_{0.6}B_{0.02}$ as-mechanically alloyed raw powder: (a) Complete spectrum; (b) Zoom on the high diffraction angle values.*

The XRD patterns of both powders show only peaks related to the $Mg_2Si_{0.4}Sn_{0.6}$ specie. In both cases, all peaks are symmetrical, whatever the value of the diffraction angle.

SEM observations show that both powders consist of large agglomerates made of nanometer-sized crystallites, as shown on figure 5.2. An average crystallite size of 40 nm is calculated for both powders (Williamson-Hall method [105]).

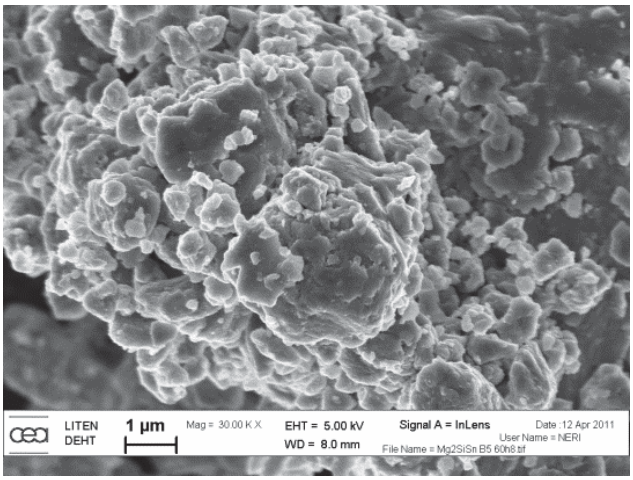

Figure 5.2: *SEM image of the boron doped Mg-Si-Sn powder.*

5.2.2 Sintering of $Mg_2Si_{1-x-y}Sn_xB_y$ (x = 0.6; y = 0.0125, 0.02) compositions

As spark plasma sintering (SPS) is an efficient way to produce fully consolidated samples in a short time, we applied it again to both powders synthesized. We placed 2 grams of powder $Mg_2Si_{1-x-y}Sn_xB_y$ (x = 0.6; y = 0.0125, 0.02) in a graphite die (internal diameter was always 20 mm, thickness was always 15 mm) and put everything in the SPS machine as was described in previous chapters. Sintering was performed with a pressure of 61 MPa (always applied on the powder bed at room temperature), in an argon atmosphere (pressure always set to 1035 hPa). Heating rate was 100 °C/min until the maximum temperature of 575 °C ($Mg_2Si_{0.3875}Sn_{0.6}B_{0.0125}$) and 625 °C ($Mg_2Si_{0.38}Sn_{0.6}B_{0.02}$) were reached. In all cases, soak time was 5 minutes. It was followed by a 50 °C/min cooling step until 400 °C. Afterwards, natural cooling of the equipment was used. During this cooling step, pressure was fully released. Final relative sintered densities were 94.52 % and 99.07 % for the $Mg_2Si_{0.3875}Sn_{0.6}B_{0.0125}$ and $Mg_2Si_{0.38}Sn_{0.6}B_{0.02}$ formulations, respectively.

Figure 5.3a and 5.3b show the XRD spectrum of the $Mg_2Si_{0.38}Sn_{0.6}B_{0.02}$ as-sintered material (for the $Mg_2Si_{0.3875}Sn_{0.6}B_{0.0125}$ formulation, the XRD data is similar). All the peaks are matching with the ones of the $Mg_2Si_{0.4}Sn_{0.6}$ phase. No shoulder is detected at the left side of the diffraction peaks for large angle values.

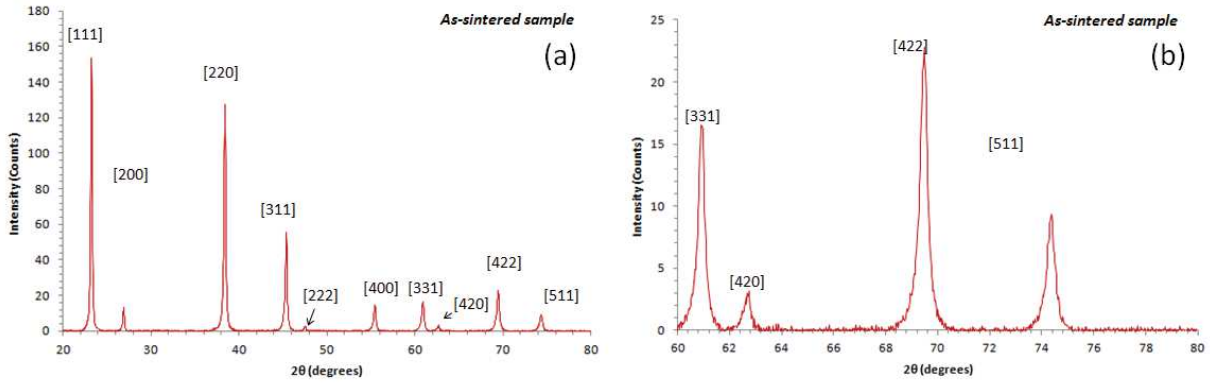

Figure 5.3: *XRD spectrum on $Mg_2Si_{0.38}Sn_{0.6}B_{0.02}$ as-sintered sample: (a) Complete spectrum; (b) Zoom on the high diffraction angle values.*

The microstructure of both as-sintered samples is shown in figure 5.5. No detailed microstructure observations have been completed on these samples, because the thermoelectrical properties were disappointing, as it will be presented hereafter.

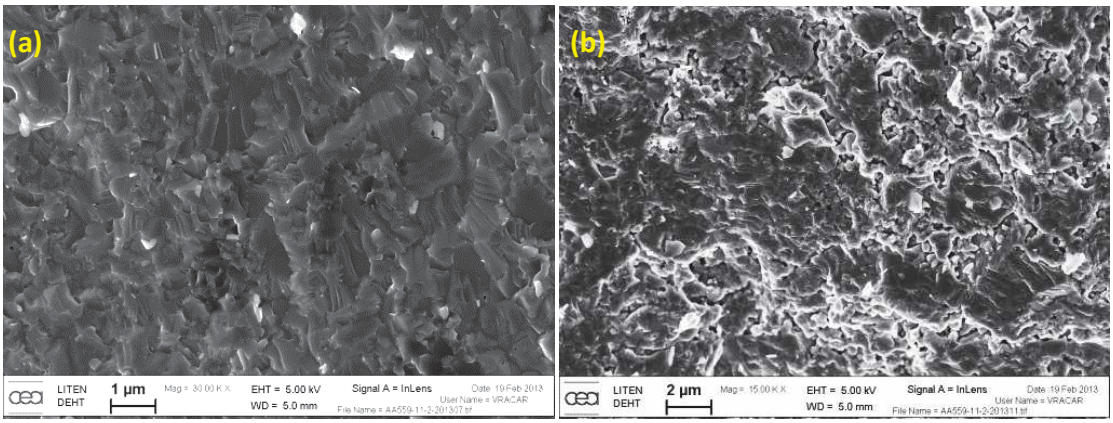

Figure 5.5: *Fracture surface of both as-sintered samples: a) $Mg_2Si_{0.38}Sn_{0.6}B_{0.02}$; b) $Mg_2Si_{0.3875}Sn_{0.6}B_{0.0125}$.*

5.2.3 Thermoelectric properties

The thermoelectrical properties of both boron doped Mg-Si-Sn as-sintered materials are shown in figure 5.6. Obviously, the electrical conductivity is much lower than that of the n-type material we investigated in previous chapters (figure 5.6a). For example, at 500 °C, the electrical conductivity for the boron doped Mg-Si-Sn samples is in the range 12000-16000 S/m, against 90000 to 100000 S/m for the n-type material. More important is that the as-sintered p-type materials exhibit a metallic behavior (increase of the electrical conductivity with the raise of the temperature) instead of the ones of degenerated semiconductors. Whatever the sample, it is also interesting to point out that the Seebeck coefficient shows p→n transition, as shown in figure 5.6b. Thusly, power factor (figure 5.6c) suffers due to the drastic changes of Seebeck coefficients and low electrical conductivities.

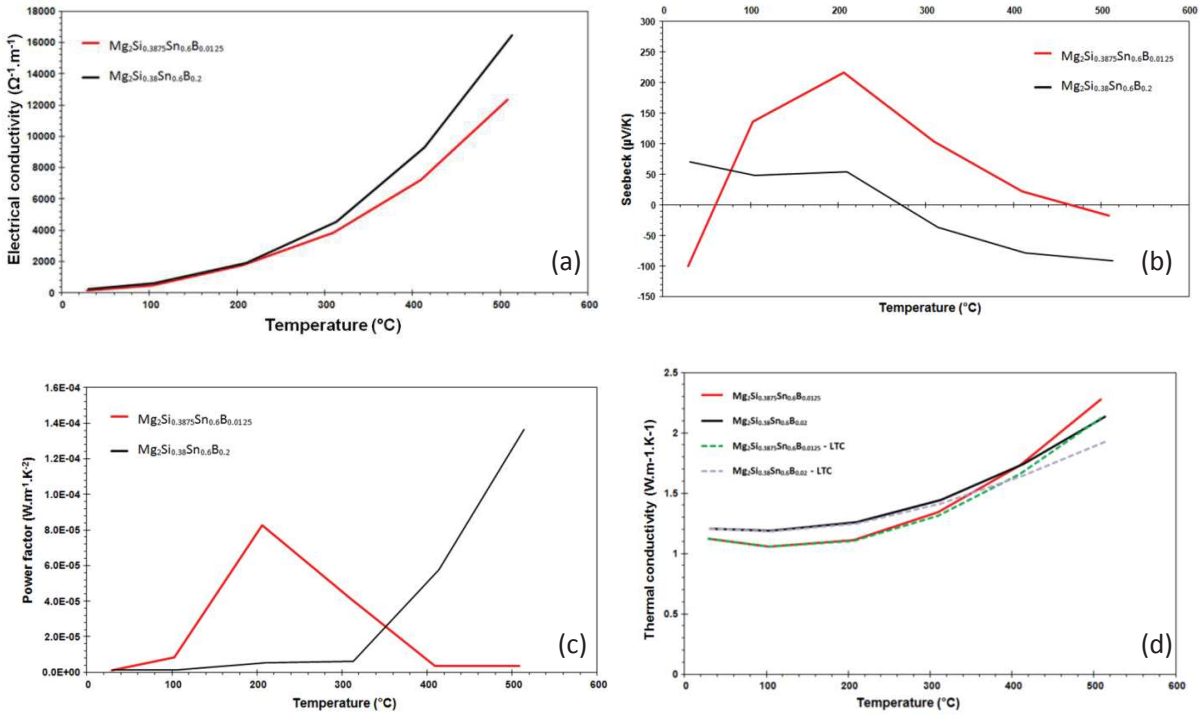

Figure 5.6: *Thermoelectrical properties in function of temperature measured on the as-sintered sample made from powder synthesized by MA: (a) electrical conductivity; (b) Seebeck coefficient; (c) power factor; (d) thermal conductivity.*

Figure 5.6d shows the variation of thermal conductivity in function of temperature for both as-sintered samples. Clearly, whatever the sample, the thermal conductivity is driven by the lattice contribution (LTC).

Finally, whatever the boron concentration introduced, the dimensionless figure of merit is kept to a very low level with a maximum value around 0.05 obtained at 500 °C for the $Mg_2Si_{0.38}Sn_{0.6}B_{0.02}$ material.

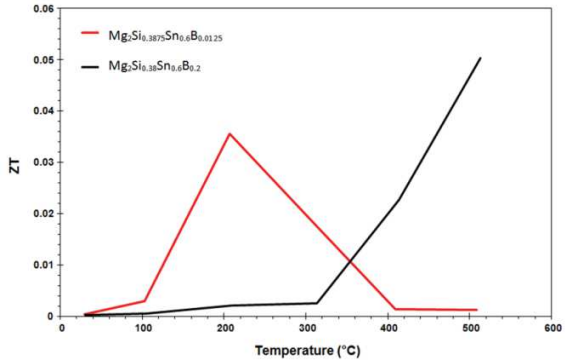

Figure 5.7: *Thermoelectric figure of merit (ZT) in function of temperature.*

5.2.4 Conclusion

Doping Mg-Si-Sn alloys with boron did not provide a stable p-type behavior of the as-sintered materials when exposed to increasing temperatures. Moreover, the ZT parameter reaches a maximum value around 0.05 at 500 °C which is drastically low. Accordingly, we decided to stop investigations on p-type Mg-Si-Sn materials and to switch to HMS alloys.

5.3 Higher manganese silicides - $MnSi_{1.75}$

5.3.1 Material

We have prepared a p-type $MnSi_{1.75}$ alloyed powder by mechanical alloying, in argon atmosphere. Again, we used the same planetary ball mill, but this time we used a smaller zirconia jar (250ml), and zirconia balls (BPR = 26.25). A 1 wt. % of cyclohexane was added as a processing aid.

To optimize the synthesis of $MnSi_{1.75}$, we put 8 grams of constituents (Mn and Si) into the jar and we milled it for 6, 12, 24 and 60 hours in argon atmosphere. XRD data on the mechanically-alloyed powders are shown in figures 5.8 and 5.9.

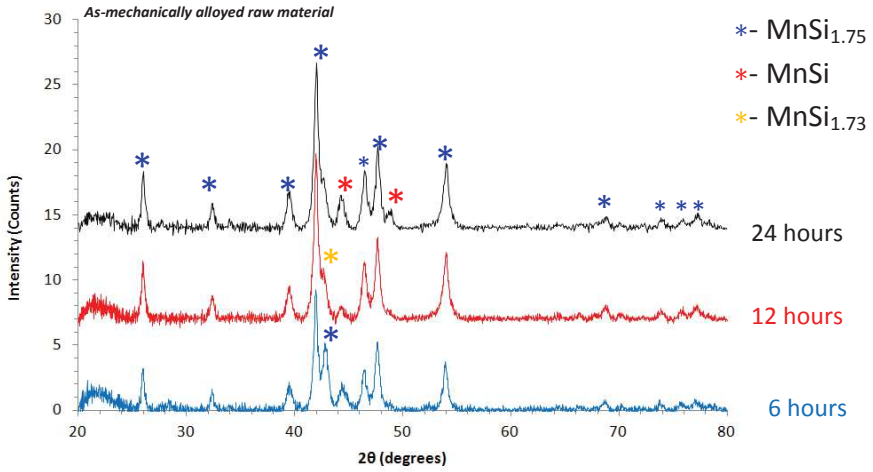

Figure 5.8: *XRD patterns of as-mechanically alloyed $MnSi_{1.75}$ alloy with milling times of: 6 hours (blue); 12 hours (red); 24 hours (black).*

In figure 5.8, we observed that after 6 hours, the peaks of $MnSi_{1.75}$ are clearly visible, while after 12 hours, different phases were present (smaller amounts of $MnSi_{1.75}$ and large amount of $MnSi_{1.73}$). We also observed the occurrence of peaks related to the MnSi phase which is not desirable because it has metal and not semiconducting properties. This is in agreement with the literature, since Zamanipour [49] observed also the creation of the MnSi phase while

mechanically alloying $MnSi_x$ (x = 1.73, 1.75 and 1.77). He prepared his material by mixing stoichiometrically the constituents in a tungsten carbide jar and milled with ball-to-powder ratio of 5 with tungsten carbide balls. XRD patterns, as the one shown on figure 5.9, are used to calculate the size of the elemental crystallites that constitute the aggregated collected powders at the end of the mechanical-alloying step (Williamson-Hall method [7]). Finally, it has been calculated that each aggregate is composed of elemental crystallites having an average diameter of 218, 110, 70, and 40 nm for milling times of 6, 12, 24, and 60 hours, respectively.

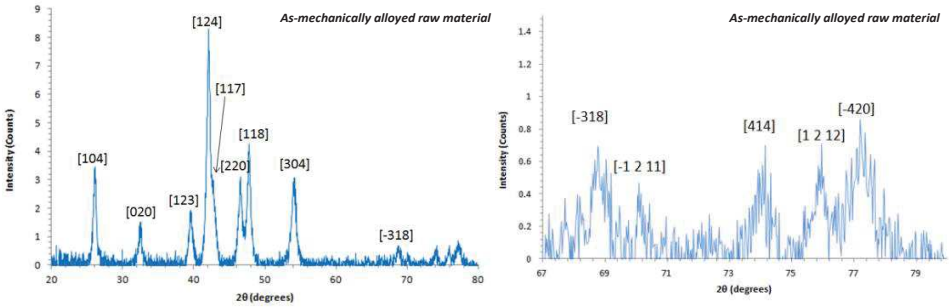

Figure 5.9: *XRD spectra on the as-mechanically alloyed raw powder after 60 hours of milling: (a) Complete spectrum; (b) Zoom on the high diffraction angle values.*

5.3.2 Spark Plasma Sintering (SPS)

We have chosen the powder that has been collected after 60 hours of mechanical alloying. Then SPS has been used to consolidate this powder. Most of the parameters were the same exposed for n and p-type Mg-Si-Sn alloys. The die was filled with 3.15 grams of powder, to obtain as-sintered samples having a height around 2 mm. We used heating rate of 100 °C/min, a macroscopic compaction pressure fixed to 50 MPa, and always the standard 12:2 pulse sequence for the DC current.

Figure 5.10 shows the densification rate in function of temperature for the powder investigated. As before for the n-type Mg-Si-Sn alloys (see Chapter 3), it exhibits a bell-shape curve.

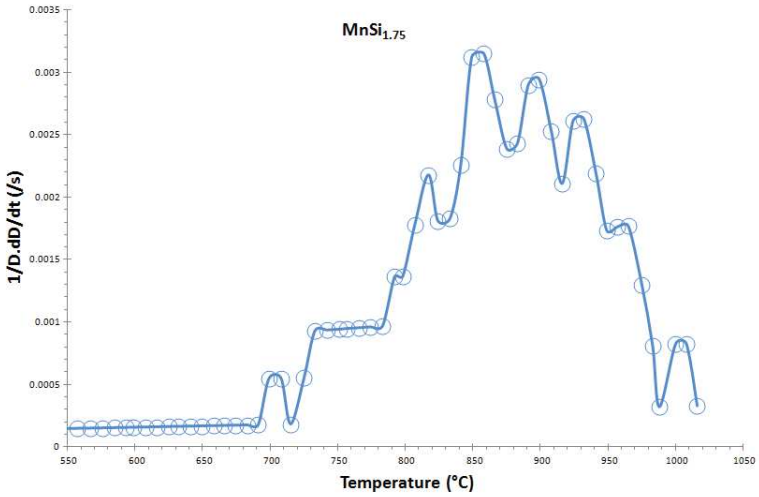

Figure 5.10: *Evolution of the densification rate in function of temperature for the selected raw powder.*

From the figure 5.10, we can see that densification starts around 700 °C and ends around 990 °C. Maximum densification rate is 3.1×10^{-3}/s at 849 °C. Thusly we sintered one sample at 980 °C, with a soak time of 7 minutes (after five minutes, pressure was released to zero in one minute, followed by another minute of pressureless soak), and cooling was fixed to 30 °C/min from 980 °C to 400 °C. The final relative density of the sintered sample was measured to be 99.01 %.

XRD spectrum of the as-sintered sample is shown on Figure 5.11. Most of the peaks match with the $MnSi_{1.75}$ phase, but some are also linked to the undesirable MnSi one.

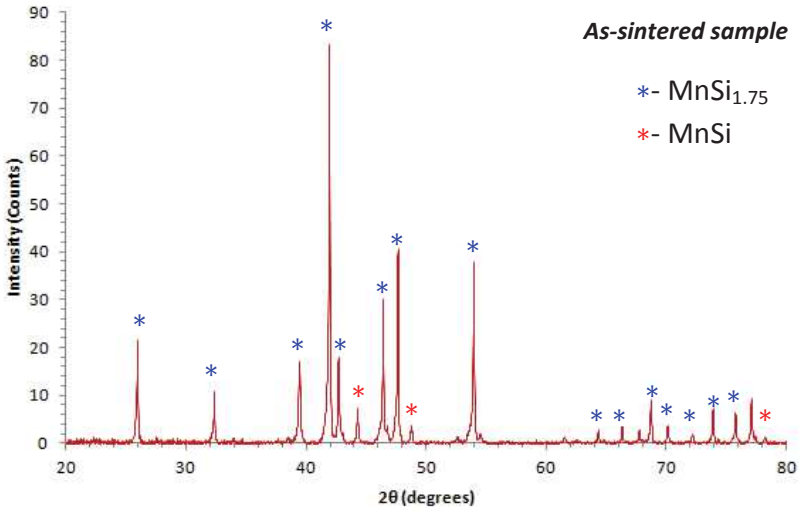

Figure 5.11: *XRD spectra on the as-sintered sample.*

5.3.3 Thermoelectric properties

Figure 5.12 shows the evolutions of the thermoelectrical properties in function of temperature for the as-sintered sample investigated. The electrical conductivity evolution is typically the one of a degenerated semiconductor and the values, whatever the temperature of interest, are not too far from the ones measured by Luo [51]. Luo obtained his samples by melt-spinning. For that, he pressed the powder mixture made of raw elements having the $MnSi_{1.75}$ composition to a disk and then induction melted the mix at 1450 °C. The obtained ingot was melted in a quartz tube and then ejected through a 0.5 mm diameter nozzle under pressure of 0.02 MPa obtaining ribbon-shaped samples that were pulverized to powder and then sintered by SPS (sintering temperature and time were 850 °C and 3-5 minutes, respectively). We compared our findings with the data published by Luo [51] that are also presented in the figure 5.12.

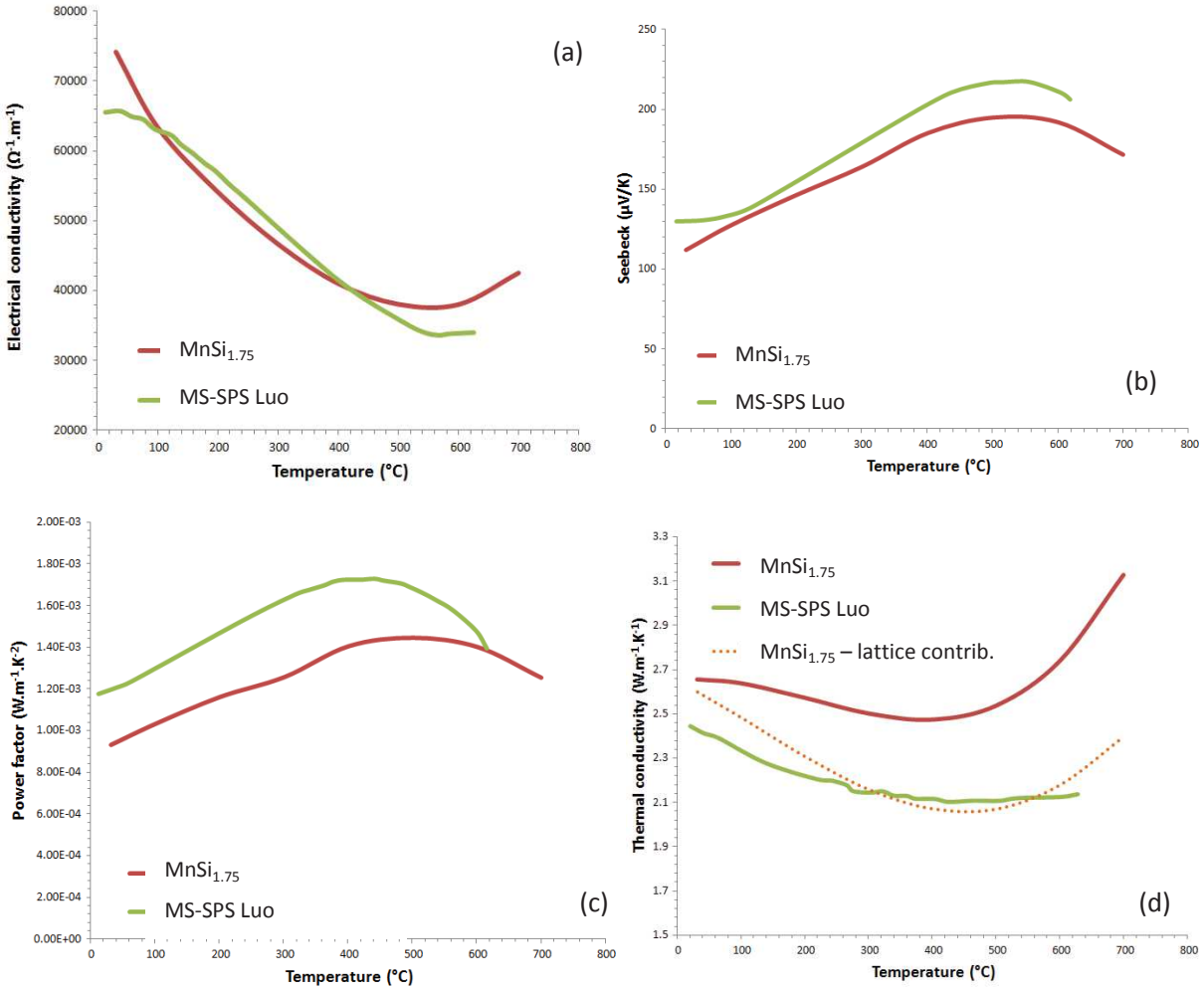

Figure 5.12: *Thermoelectrical properties in function of temperature measured on the as-sintered sample made from powder synthesized by MA: (a) electrical conductivity; (b) Seebeck coefficient; (c) power factor; (d) thermal conductivity.*

Carrier concentration measurement is considered to be problematic, due to the presence of MnSi phase which is ferromagnetic [127,128]. Thusly, the value may not be accurate. Despite of this problem, the carrier concentration of our as-sintered sample, with a composition of $MnSi_{1.75}$, was measured to be 8.3×10^{19} carriers/cm^3 at room temperature. For reference, Itoh [86] obtained a value of 3.5×10^{19} carriers/cm^3, while Luo [51] obtained a much higher value of 1.9×10^{21} carriers/cm^3.

The values of electrical conductivity and Seebeck coefficient are reported on figure 5.12a and b. The evolution of the electrical conductivity in function of temperature are similar for our material and the one developed by Luo [6]. The biggest difference between both materials lies the Seebeck coefficients in 500-600 °C temperature range (figure 5.12b). Luo obtained much

better values. Therefore, there the power factor of Luo's sample made by melt-spinning (figure 5.12c) is much better than the one measured on our sample, whatever the temperature.

Thermal conductivity presented in figure 5.12d shows also a strong difference between our results and the ones obtained by Luo [51]. According to the different steps needed to create his sample, Luo optimized the sintered microstructure for his material, thusly reducing the lattice contribution (lattice thermal conductivity – LTC) to thermal conductivity by promoting a nanometer-sized grain size. Even is the lattice thermal conductivity is also the major contributor to thermal conductivity in our sample, it is clear that the microstructure of our material is not optimized.

Finally, the dimensionless figure of merit is represented in Figure 5.13.

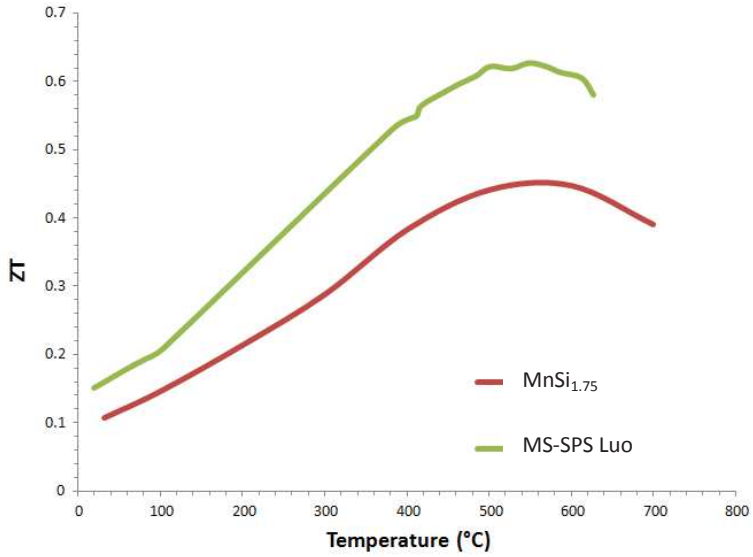

Figure 5.13: *Thermoelectric figure of merit (ZT) in function of temperature.*

Our as-sintered $MnSi_{1.75}$ alloys has the ZT value of 0.45 at 575 °C which is as high as it was reported Itoh [86] and higher than previously reported by Shin (ZT = 0.29) [129], Zhou (ZT = 0.3) [130] or Luo (0.4 for mechanically alloyed sample) [51] for the same temperature. Nonetheless it is still below the results obtained by Luo on is material prepared from a powder synthesized by melt-spinning [6].

5.3.4 Conclusion

In this chapter, we exposed the first results obtained regarding the development of a p-type Mg-Si-Sn material that could coexist with an n-type Mg-Si-Sn material in thermoelectrical modules able to work in the 300-600 °C temperature range.

It was shown that doping Mg-Si-Sn alloys with boron gives a material exhibiting p→n transitions when exposed to temperature. Consequently, we have gave up with such formulations and turned to the HMS alloys family for a p-type solution.

Preliminary results on HMS alloys are encouraging. Using only two manufacturing steps (mechanical-alloying followed by spark plasma sintering) it is possible to obtain an as-sintered $MnSi_{1.75}$ material having a peak ZT value of 0.45 at 575 °C. Nonetheless, a lot of complementary investigations have still to be completed. Optimization of the sintering cycle is required to minimize as much as possible the residual amount of the undesirable metallic MnSi phase. Optimizing the sintering parameter will also help to optimize the grain size of the sintered material, to keep the thermal conductivity to low values. Doping with aluminum, as done by Luo [131], is also an opportunity to increase as much as possible the electrical conductivity with a tailored Seebeck coefficient. Finally strong links with microstructure investigations (SEM and TEM) have to be established.

CHAPTER 6

GENERAL CONCLUSION

6. General conclusion

Thermoelectric materials have the ability to directly convert temperature differences to electric voltage, and vice versa. This is possible by three reversible effects named Seebeck, Peltier, and Thomson effects. Research on thermoelectric materials got a lot of attention in the late 20th century, due to energy crisis and environmental concerns. Since then, waste heat recovery systems with devices made with thermoelectric materials are planned to be used in vehicles, wireless sensor networks, space exploration etc… The performance of these materials relies on the dimensionless figure of merit ZT that depends on the electrical conductivity (σ), thermal conductivity (κ), and Seebeck coefficient (S). Improvement of ZT is not an easy task because σ, κ and S parameters are interrelated with each other.

In this thesis, we have decided to focus on Mg-Si-Sn alloys with the aim to develop n-type and p-type materials exhibiting a high ZT in the 400-500 °C temperature range. Because the development of a p-type Mg-Si-Sn alloys was thought to be a challenge we decided to choose also Mn-Si alloys as an alternative solution in case of failure.

The first part of this thesis was to elaborate the raw powders of interest. For that, we used mechanical-alloying. This method was shown effective for synthesizing Mg-Si-Sn and Mn-Si aggregated powders made of crystallites having a nanometer-size character. Then, spark plasma sintering (SPS) was chosen as a sintering technique and was shown also to be an effective way in obtaining dense compacts in a short time, whatever the material investigated. In the literature, the production of these kind of sintered alloys is mostly done by complicate methods (a lot of steps) that are time consuming (long annealing treatments are required). In comparison, our manufacturing method is definitively simpler and shorter.

We first focused on the n-type $Mg_2Si_{0.3875}Sn_{0.6}Sb_{0.0125}$ composition. During the preliminary results we observed a great number (1.9×10^9/mm^2) of nanometer-sized (13 nm in diameter) Sn-rich/Mg-poor precipitates/inclusions homogeneously dispersed in the sintered microstructure. They have formed in-situ during the sintering cycle and were effective in dispersing phonons thus keeping the thermal conductivity of the material to law values. Such a non-optimized material gave us a ZT value around 0.9 at 500 °C. In a second step, by optimization of the sintering conditions, we were able to tailor the carrier concentration (-60%) and the precipitates/inclusions concentration (3.7×10^9/mm^2)/size (12 nm), which resulted in a higher Seebeck coefficient and a lower thermal conductivity in all the temperature range of interest for the material investigated. Finally, we obtained an optimized material that exhibited a ZT parameter of 1.2 at 500 °C, thusly gaining an increase in ZT value of 33% in comparison to the non-optimized material.

Further on, we added 1.7 vol. % of MgCuSn (Half-Heusler – HH) nanoparticles (25 mm diameter) to our $Mg_2Si_{0.3875}Sn_{0.6}Sb_{0.0125}$ formulation. Using the same optimized sintering conditions than for the $Mg_2Si_{0.3875}Sn_{0.6}Sb_{0.0125}$ matrix alone, we were able to further increase the concentration ($5.2\times10^9/mm^2$) of the nanometer-sized (10-16 nm) precipitates / inclusions / nodules that form naturally during the manufacturing step. Accordingly, the obtained material exhibits a very low thermal conductivity in the 20-500 °C temperature range. In the time, the electrical conductivity is increased to high values for a reason that has still to be clarified. Finally, a value of ZT around 1.4 was obtained at 500 °C, which is one of the highest values ever recorded for the Mg-Si-Sn system.

Our attempts to create a p-type Mg-Si-Sn material, by doping with B, have failed. This alloy shows a p→n transitions when exposed to temperature and low ZT values. Because time was missing to go further, we have then decided to discontinue our investigations on this material. Thusly, we have chosen a new p-type material from the higher manganese silicide (HMS) group: $MnSi_{1.75}$. By optimizing the mechanical alloying and spark plasma sintering steps, we were able to obtain fully dense samples. The elemental grains have the $MnSi_{1.73}$ composition but the parasitic MnSi phase (metallic behavior instead of semiconducting one) is also detected in the sintered microstructure. Nevertheless, a ZT parameter of 0.45 was measured at 575 °C. As for the n-type Mg-Si-Sn alloy we developed, the manufacturing process used contains only two steps: mechanical-alloying followed by spark plasma sintering; This is always a strong advantage in comparison to what is reported in the literature, where a lot of steps that are complex and time consuming are used.

In the future, it should be interesting to continue the investigations on the n-type and p-type silicide materials we developed. For the n-type Mg-S-Sn material, it could be interesting to improve the capacity of the milling media to be able to manufacture few kilograms of powder per batch. Other methods, that are more compatible with mass production, should also be evaluated for synthesizing the raw powder. Regarding the p-type Mn-Si material, a lot of work is still needed to optimize the sintering cycle and to establish relationships between the processing parameters and the sintered microstructure. Adding Al as a dopant could be also an effective way to increase the ZT parameter in the 20-700 °C temperature range. For both materials, it will be also mandatory to increase the diameter of the sintered pellets. A target diameter of 60 mm would be great. Accordingly, investigating the microstructure / thermoelectrical properties homogeneity will be required. Finally, it will be also critical to evaluate how both kinds of materials resist (thermoelectrical properties and microstructure) to thermal ageing in different kinds of atmospheres.

References:

1 Kittel, C. *Introduction to Solid State Physics*. Wiley, 1996.

2 Yamashita, O. and Odahara, H. Enhancement of the thermoelectric figure of merit in p- and n-type Cu/Bi-Te/Cu composites. *J. Mater. Sci*, 41, 10 (2006), 2795.

3 Joshi, G. *PhD Thesis*. The Graduate School of art and Science, Department of Physics, Boston College, 2010.

4 Thomson, W. On the Dynamical Theory of Heat, with numerical results deduced from Mr Joule's equivalent of a Thermal Unit, and M. Regnault's Observations on Steam. *Proc. Roy. Soc. Edingburgh*, 91 (1851).

5 MacDonald, D. K. C. *Thermoelectricity: An Introduction to the Principles*. Dover Books, N.Y., 2006.

6 Moos, T. S. *Handbook of Semiconductors*. Elsevier Science Publishers, Amsterdam, 1992.

7 Heremans, J. P., Thrush, C. M., Morelli, D. T., and Wu, M. -C. Thermoelectric power of bismuth nanocomposites. *Phys. Rev. B*, 88 (2002), 216801.

8 Franz, R. and Wiedemann, G. Ueber die Wärme-Leitungsfähigkeit der Metalle. *Annalen der Physik*, 165, 8 (1853), 497-531.

9 Kittel, C. *Introduction to Solid State Physics*. John Wiley & Sons, Inc, 2005.

10 Ashcroft, N. W. and Mermin, D. N. *Solid State Physics*. Brooks/Cole, 1976.

11 Abeles, B., Beers, D. S., Cody, G. D., and Dimukes, J. D. Thermal Conductivity of Ge-Si Alloys at High Temperatures. *Phys. Rev.*, 125, 1 (1962), 44.

12 Iijima, S. Helical Microtubules of Graphitic carbon. *Nature*, 354 (1991), 56.

13 Hicks, L. D. and Dresselhaus, M. S. Effect of quantum-well structures on the thermoelectric figure of merit. *Phys Rev B Condens Mater*, 19, 47 (1993), 12727-12731.

14 Gothard, N. *The Effects of Nanoparticle Inclusions upon the Microstructure and Thermoelectric Transport Properties of Bismuth Telluride-Based Composites*. All Dissertations, 2008.

15 Hicks, L. D., Harman, T. C., and et al. Experimental study of the effect of quantum-well structures on the thermoelectric figure of merit. *Phys. Rev. B.*, 53 (1996), R10493.

16 Venkatasubramanian, R., Siivola, E., Colpitts, T., and O'Quinn, B. Thin-film thermoelectric devices with high room-temperature figures of merit. *Nature*, 4113, 6856 (2001), 597-602.

17 Koga, T., Cronin, S. B., and et al. Experimental proof-of-principle investigation of enhanced Z3dT in (001) oriented Si/Ge superlattices. *Appl. Phys. Lett*, 77 (2000), 1490.

18 Alleno, E., Chen, L., and et al. Thermal conductivity reduction in CosB3-Ceo2 nanocomposites. *J. Electr. Mater.*, 39, 9 (2010), 1966.

19 Chasmar, R. P. and Stratton, R. The Thermoelectric Figure of Merit and its Relation to Thermoelectric Generators. *J. Electronics and Control*, 7, 1 (1959), 52-72.

20 Godart, C. *Matériaux à effets thermoélectriques*. Techniques de l'ingénieur, 2009.

21 Sootsman, J. R., Chung, D. Y., and Kanatzidis, M. G. New and Old Concepts in Thermoelectric Materials. *Angew. Chem. Int. Ed.*, 48, 46 (2009), 8616-8639.

22 Bennet, G. L. Space nuclear power: opening the final frontier. (San Diego 2006), 4th International Energy Conversion Engineering Conference and Exhibit.

23 Fairbanks, J. W. *Overview of high efficiency thermoelectrics and potential applications*. High Efficiency Thermoelectric Workshop, San Diego, 2004.

24 Fairbanks, J. W. Vehicular thermoelectric applications. (Paris 2008), 6th European Conference on Thermoelectrics.

25 Wolfe, R. and Smith, G. E. Thermoelectric properties of bismuth-antimony alloys. *J. Appl. Phys.*, 33, 3 (1962), 841-846.

26 Fleural, J. P., Gailliard, L., Triboulet, R., Scherrer, H., and Scherrer, S. Thermal properties of high quality single crystals of bismuth telluride-Part I: experimental chracterization. *J. Phys. Chem. Solids*, 49, 10 (1988), 1237-1247.

27 Fleurial, J. P., Gailliard, L., Triboulet, R., Scherrer, H., and Scherrer, S. Thermal properties of high quality single crystals of bismuth telluride-Part II: Mixed-scattering model. *J. Phys. Chem. Solids*, 49, 10 (1988), 1249-1257.

28 Kajikawa, T. Status and future prospects on the development of thermoelectric power generation systems utilizing combustion heat from municipal solid waste. In *Proceedings of the 16th International Conference on Thermoelectrics* (Dresden, Germany 1997).

29 Ioffe, A. F. *Semiconductor Thermoelements and Thermoelectric Cooling*. Infosearch, London, 1957.

30 LaLonde, A. D., Pei, Y., and Snyder, J. G. Reevaluation of PbTe1-xIx as high perforamce n-type thermoelectric material. *Energy Environ Sci*, 4 (2011), 2090-2096.

31 Goldsmid, H. J. *Introduction to Thermoelectricity*. Springer Series in Materials Science, 2009.

32 Fleurial, J. P. Design and discovery of highly efficient thermoelectric materials. (Florence 1998), 9th CIMTECH-World ceramics congress and forum on new materials.

33 Jovovic, V. and al., et. Low temperature thermal, thermoelectric, and thermoemagnetic transport in indium rich Pb1-xSnxTe alloys. *J. Appl. Phys.*, 103 (2008), 053710.

34 Heremans, J. P., Jovovic, V., and al., et. Enhancement of thermoelectric efficiency in PbTe by distortion of the electronic density of states. *Science*, 321, 5888 (2008), 554-557.

35 Biswas, K., He, J., Blum, I. D., and al., et. High-performance bulk thermoelectrics with all-scale hieraarchical architectures. *Nature*, 489 (2012), 414-418.

36 Hoang, K., Desai, K., and Mahanti, S. D. Charge ordering and self-assembled nanostructures in a fcc Coulomb lattice gas. *Phys. Rev. B*, 72 (2005), 064102.

37 Sootsman, J. R., Pcionek, R. J., Kong, H., and al., et. Strong Reduction of Thermal Conductivity in Nanostructured PbTe Prepared by Matrix Encapsulation. *Chem. Mater.*, 18 (2006), 4993-4995.

38 Nolas, G. S., Cohn, J. L., and Schujman, S. B. Semiconducting Ge clathrates: Promising candidates for thermoelectric applications. *Appl. Phys Lett*, 73 (1998), 178.

39 Saramat, A., Svensson, G., Palmqvist, A. E.C., and al., et. Large thermoelectric figure of merit at high temperature in Czocharlski grown clathrate Ba8Ga16Ge30. *J. Appl. Phys*, 99, 2 (2006), 023708-023708-5.

40 Nolas, G. S., Morelli, D. T., and Tritt, T. M. Skutterduties: a phonon-glass-electron-crystal approach to advanced thermoelectric energy conversion applications. *Annu Rev Mater Sci*, 29 (1999), 89-116.

41 Shu, X., Yang, J., Salvador, J. R., and al., et. Multiple-Filled Skutterudites: High Thermoelectric Figure of Merit through Separately Optimizing Electrical and Thermal Transports. *J. amer. Chem. Soc.*, 133 (2011), 7837.

42 Liu, R., Yang, J., Chen, X., and al., et. p-Type skutterudites RxMyFe3CoSb12 (R,M =ba, ce, Nd, and Yb): Effectiveness of double-filling for the lattice thermal conductivity reduction. *Intermetallics*, 19, 11 (2011), 1747-1751.

43 Isoda, Y. and al., et. Thermoelectric properties of sintered Mg2Si(1-x)Snx. (Adelaide australia 2004), Proc. 23rd International conference on Thermoelectrics.

44 Liu, W., Zhang, Q., Tang, X., and al., et. Thermoelectric properties of Sb-doped Mg2Si0.3Sn0.7. *J Electron Mater*, 40, 5 (2011), 1062-6.

45 Zaitsev, V. K., Fedorov, M. I., Gurieva, E. A., and al., et. Highly effective Mg2Si1-xSnx thermoelectrics. *Phys. Rev. B*, 74 (2006), 045207.

46 Zaitsev, V. K., Fedorov, M. I., Gurieva, E. A., Eremin, I. S., Konstantinov, P. P., Samunin, A. Y., and Vedernikov, M. V. Proceedings of the 24th International Conference on Thermoelectrics IEEE Catalog Number 05TH8854. (2005), Clemson University, USA.

47 Zhang, Q., He, J., Zhu, T. J., and Zhang, X. B. High figures of merit and natural nanostructures in Mg2Si0.4Sn0.6 based thermoelectric materials. *Appl. Phys. Lett*, 93 (2008), 102109.

48 Zhu, T. J., Cao, Y. Q., Zhang, Q., and Zhao, X. B. Bulk Nanostructured Thermoelectric Materials: Preparation,

Structure and Properties. *J. Electron. Mater.*, 39 (2010), 1990.

49 Liu, W., Tan, X., Yin, K., Liu, H., and al., et. Convergence of Conduction Bands as a Means of Enhancing Thermoelectric Performance of n-Type Mg2Si1−xSnx Solid Solutions. *Phys. Rev. Lett.*, 108 (2012), 166601.

50 Liu, W., Tang, X., Li, H., and Yin, K. Enhanced thermoelectric properties of n-type Mg2.16(Si0.4Sn0.6)1−ySby due to nano-sized Sn-rich precipitates and an optimized electron concentration. *J. Mater. Chem.*, 22 (2012), 13653.

51 Liu, W., Tang, X., Li, H., and Sharp, J. Optimized thermoelectric properties of Sb-doped Mg2(1+ z)Si 0.5-ySn0.5Sby through adjustment of the Mg content. *Chem. Mater.*, 23 (2011), 5256.

52 Gao, P., Berkun, I., Schmidt, R. D., and al., et. Transport and Mechanical Properties of High-ZT Mg2.08Si0.4-xSn0.6Sbx Thermoelectric Materials. *Electron. Mater.*, 43, 6 (2013), 1790.

53 Isoda, Y., Tada, S., Nagai, T., and Fujiu, H. Thermoelectric Properties of p-Type Mg2Si0.25Sn0.75 with Li and Ag Double Doping. *Mater Trans*, 51 (2010), 868-871.

54 Mars, K., Ihou-Mouko, H., Pont, G., and al., et. Thermoelectric Properties and Electronic Structure of Bi- and Ag-Doped Mg2Si1-xGex Compounds. *J. Electron. Mater.*, 38 (2009), 1360.

55 Ihou-Mouko, H., Mercier, C., Tobola, J., and al, et. Thermoelectric properties and electronic structure of p-type Mg2Si and Mg2Si0.6Ge0.4 componds doped with Ga. *J. Alloy. Compd.*, 509 (2011), 6503-6508.

56 Zamanipour, Z., Shi, X., Mozafari, M., and al., et. Synthesis, characterization, and thermoelectric properties of nanostructured bulk p-type MnSi1.73, MnSi1.75, and MnSi1.77. *Ceram. Int.*, 39, 3 (2013), 2353-2358.

57 Aoyama, I., Kaibe, H., Rauscher, L., and al., et. Doping Effects on Thermoelectric properties of Higher Manganese Silicides (HMS, MnSi1.74) and Characterization of Thermoelectric Generating Module using p-Type (Al, Ge and Mo)-doped HMSs and n-Type Mg2Si0.4Sn0.6 Legs. *Jpn. J. Appl. Phys.*, 44 (2005), 4275-4281.

58 Luo, W., Li, H., Yan, Y., and al., et. Rapid synthesis of high thermoelectric performance higher manganese silicide with in-situ formed nano-phase of MnSi. *Intermetallics*, 19 (2011), 404-408.

59 Bathula, S., Jayyasimhadri, M., Singh, N., and al., et. Enhanced thermoelectric figure-of-merit in spark plasma sintered nanostructured n-type SiGe alloys. *App. Ceram. Tech.*, 3, 1 (2006), 32-40.

60 Joshi, G., Lee, H., Wang, X. W., and al., et. Enhanced Thermoelectric Figure-of-Merit in nanostructured p-type Silicon Germanium Bulk Alloys. *Nano Letters*, 8, 12 (2008), 4670-4674.

61 Mingo, N., Hauser, D., Kobayashi, N. P., and al., et. Nanoparticle-in-alloy approach to efficient thermoelectrics: Silicides in SiGe. *Nano Letters*, 9, 2 (2009), 711-715.

62 Wang, X. *PhD thesis*. The Graduate School of Art and Science, Department of Physics, Boston College, 2009.

63 Favier, K., Bernard-Granger, G., and al., et. Influence of in situ formed MoSi2 inclusions on the thermoelectrical properties of an N-type silicon-germanium alloy. *Acta Mater.*, 64 (2014), 429-442.

64 Snyder, G. J. and Toberer, E. S. Complex thermoelectric materials. *Nature Mater.*, 7 (2008), 105-114.

65 Dresselhaus, M. S., Chen, G., Tang, M. Y., and al., et. New Directions for low dimensional thermoelectric materials. *Adv. Mater.*, 19 (2007), 1043-1053.

66 Joshi, G. *Study of thermoelectric properties of nanostructured p-type Si-Ge, Bi-Te, Bi-Sb, and Half-Heusler bulk materials*. Doctoral Dissertation, Boston, US, 2010.

67 Nolas, G. S., Slack, G. A., and Morelli, D. T. The effect of rare-earth filling on the lattice thermal conductivity of skutterudites. *J. Appl. Phys.*, 79 (1996), 4002.

68 Fluerial, J. P., Caillat, T., and Borshchevsky, A. Proceedings of the 13th international conference on thermoelectric. (1994).

69 Heremans, J. P., Thrush, C. M., and Morelli, D. T. Thermopower enhancement in lead telluride nanostructures. *Phys. Rev. B*, 70 (2004), 115334.

70 Chevalier, P-Y, Fischer, E., and Rivet, A. A thermodynamic evaluation of the Mn-Si system. *Calphad*, 19 (1995), 57-68.

71 Ahmad, N. and Pratt, J. N. Thermodynamic Properties of Liquid Manganese-Silicon alloys. *Metall Trans A*, 9A (1978), 1857.

72 Tritt, T. M. Recend Trends in thermoelectric Materials Research III. *Semiconductors and Semimetals*, 71 (2001), ix-xiv.

73 Muntyanu, S. H., Sokolov, E. B., and Makarov, E. S. Study of the Mg2Sn-Mg2Si system. *J. Inorg. Mater.*, 2 (1966), 870-5.

74 Nikitin, E. N., Tkalenko, E. N., Zaitsev, V. K., and al., et. A study of the phase diagram for the Mg2Si - Mg2Sn system and the properties of certain of its solid solutions. *J. Inorg. Mater*, 4 (1968), 1656-9.

75 Jung, I-H., Kang, D-H, Park, W-J, and al, et. Thermodynamic modelling of the Mg-Si-Sn system. *CALPHAD*, 31 (2007), 192-200.

76 Kozlov, A., Gröbner, J., and Schmid-Fetzer, R. Phase formation in Mg-Sn-Si and Mg-Sn-Si-Ca alloys. *J. Alloy Compd*, 509 (2011), 3326-3337.

77 Rowe, D. M. *Thermoelectrics Handbook:Macro to Nano*. Taylor & Francis, 2006.

78 Gokhale, A. B. and Abbaschian, R. The Mn-Si (Manganese-Silicon) system. *Bulletin og alloy phase diagrams*, 11 (1990), 468-480.

79 Higgins, J. M., Schmitt, A. L., and al., et. Higher Manganese Silicide Nanowires of Nowotny Chimney Ladder Phase. *H. Am. Chem. Soc.*, 130 (2008), 16086-16094.

80 Shin, D. K., Jang, K. W., and al., et. Thermoelectric Properties of Higher Manganese Silicides Prepared by Mechanical Alloying and Hot Pressing. *J. Electron. Mater.*, 42 (2013), 1756.

81 SS, Li. *Semiconductor physical electronics*. Springer, New York, 2006.

82 Chen L, Jiang G, Chen Y, Du Z, Zhao X, Zhu T, et al. Miscibility gap and thermoelectric properties of ecofriendly Mg2Si1-xSnx (0.1>x>0.8). *J Mater Res*, 26 (2011), 3038-43.

83 Nishida, I. Semiconducting Properties of Nonstoichiometric Manganese Silicides. *J. Mater. Sci.*, 7 (1972), 435-440.

84 Migas, D. B., Shaposhnikov, V. L., Filonov, A. B., and Borisenko, V. E. Ab initio study of the band structures of different phases of higher manganese silicides. *Phys. Rev. B*, 77 (2008), 175205.

85 Teichert, S., Kilper, R., Erben, J., and al., et. Preparation and properties of thin polycrystalline MnSi1.73 films. *Appl. Surf. Sci.*, 104/105 (1996), 679.

86 Krontiras, C., Pomon, K., and Roilos, M. Resistivity and the Hall effect for thin MnSi1.73 films. *J. Phys. D: Appl. Phys.*, 21 (1988), 509-512.

87 GS Nolas, M Kaeser, RT Littleton, TM Tritt. High figure of merit in partially filled ytterbium skutterudite materials. *App Phys Lett*, 77, 12 (2000), 1855-1857.

88 Suryanarayana, C. Mechanical alloying and milling. Pergamon, Colorado, 2001.

89 Song, R. B., Aizawa, T., and Sun, J. Q. Synthesis of Mg2Si1-xSnx solid solutions as thermoelectric materials by bulk mechanical alloying and hot pressing. *Mat Sci Engi B*, 136 (2007), 111-117.

90 You, S. W., Kim, I. H., and Choi, S. M. Solid-State synthesis and Thermoelectric Properties of Mg2+xSi0.7Sn0.3Sbm. *J. Nanomater.*, 2013 (2013), 1-4.

91 Riffel, M. and Schilz, J. Mechanically alloyed Mg2Si1-xSnx solid solutions as thermoelectric materials. In *Fifteenth international Conference on Thermoelectrics* (Pasadena, CA, USA 1996).

92 Itoh, T. and Yamada, M. Synthesis of Thermoelectric Manganese Silicide by Mechanical Alloying and Pulse Discharge Sintering. *J. Elec. Mater.*, 38 (2009), 925.

93 Gottlieb, U., Sulpice, A., and al., et. Magnetic properties of single crystalline Mn4Si7. *J. Alloy. Compd.*

94 Umemoto, M., Liu, Z. G., and al., et. Production and Characterization of Mn-Si Thermoelectric Material. *Mater. Sci. Forum*, 343-346 (2000), 635-640.

95 Hu, J., Zhang, C., and al., et. Preparation and electrical properties of Mn silicides by reaction of MnCl2 and Si powder. *Phys. Procedia*, 11 (2011), 138-141.

96 Hou, Q. R., Wang, Z. M., and He, Y. J. Thermoelectric properties of manganese silicide films. *Appl. Phys. A*, 80 (2005), 1807-1811.

97 Lee, Y.- G., Choi, M.- K., and al., et. Thermoelectric properties of Nowotny phase, higher manganese silicides synthesized by mechanical alloying process. *J. Ceram. Process. Res.*, 13 (2012), 816-819.

98 Zhou, A., Zhao, X., and al., et. Grain size effect on the phase transformations of higher manganese silicide thermoelectric materials: An in-situ energy dispesive x-ray diffraction study. *J. Mater. Res.*, 26 (2011), 1900.

99 Bloxam, A. G. Improved manufacture of electric incandescent lamp filaments from tungsten or molybdenum or an alloy thereof. *GB Patent* (1906), 27002.

100 Duval D'Adrian, A. L. Article of fused metallic oxide and process of producing the same. *Patent USA* (1922), US1430724A.

101 Orru, R., Licheri, R., Locci, A. M., and al., et. Consolidation/synthesis of materials by electric current activated/assisted sintering. *Mater. Sci. Eng. R*, 63 (2009), 127-287.

102 Hoyt, S. L. Hard metal composition and method of making the same. *Patent USA* (1932), US1843768.

103 Xie, G., Ohashi, O., Chiba, K., and al., et. Frequency effect on pulse electric current sintering process of pure aluminum powder. *Mater Sci. Eng. A*, 359, 1-2 (2003), 384-390.

104 Srinivasarao, B., Oh-ishi, K., Ohkubo, T., and al., et. Synthesis of high-strength bimodally grained iron by mechanical alloying and spark plasma sintering. *Scripta Mater.*, 58, 9 (2008), 759-762.

105 Bernard-Granger, G. and Guizard, C. Spark plasma sintering of a commercially available granulated zirconia powder: I. Sintering path and hypotheses about the mechanism(s) controlling densification. *Acta Mater*, 55, 10 (2007), 3493-3504.

106 Bernard-Granger, G., Benameur, N., Addad, A., and al., et. Phenomenological analysis of densification mechanism during spark plasma sintering of MgAl2O4. *J. Mater. Res.*, 24, 06 (2009), 2011-2020.

107 Bernard-Granger, G., Addad, A., and al., et. Spark plasma sintering of a commectially available granulated zirconia powder: Comparison with hot-pressing. *Acta. Mater.*, 58, 9 (2010), 3390-3399.

108 Ramond, L., Bernard-Granger, G., and al., et. Sintering of a quasi-crystalline powder using spark plasma sintering and hot-pressing. *Acta Mater.*, 58, 15 (2010), 5120-5128.

109 Ramond, L., Bernard-Granger, G., Added, A., and Guizard, C. Sintering of Soda-Lime Glass Microspheres Using Spark Plasma Sintering. *J. Amer. Ceram. Soc.*, 94, 9 (2011), 2926-2932.

110 Khan, A. U., Vlachos, N., and Kyratsi, Th. High thermoelectric figure of merit of Mg2Si0.55Sn0.4Ge0.05 materials doped with Bi and Sb. *Scripta Mater.*, 69 (2013), 606-609.

111 Williamson, G. K. and Hall, W. H. X-ray line broadening from filed aluminium and wolfram. *Acta Metallurgica*, 1, 1 (1953), 22-31.

112 Bernard-Granger, G. and Guizard, C. Influence of co-doping on the sintering path and on the optical properties of a submicronic alumina material. *J. Am. Ceram. Soc.*, 91, 5 (2008), 1703-1706.

113 G Bernard-Granger, A Addad, et al. Influence of nanosized inclusions on the room tempeerature thermoelectrical properties of a p-type bismuth-tellurium-antimony alloy. *Acta Mater*, 60, 11 (2012), 4523-4530.

114 Delesse, A. *Cr Hebd Sci Acad Sci* (1847), 544.

115 Longo, D. M., Howe, J. M., and Johnson, W. C. Experimental method for detemining Cliff-Lorimer factors in transmission electron microscopy (TEM) utilizing stepped wedge-shaped specimens prepared by focused ion beam (FIB) thinning. *Ultramicroscopy*, 80 (1998), 85-97.

116 Joy, D. C., Romig, A. D., and Goldstein, J. *Principles of Analytical Electron Microscopy*. Springer Science & Business Media, 1986.

117 Harman, T. C. Special Techniques for Measurement of Thermoeelctric Properties. *J. Appl. Phys.*, 29 (1958), 1373.

118 Liu, W., Yin, K., Su, X., Li, H., Gao, Y., and Tang, X. Enhanced hole concentration through Ga doping and excess of Mg and thermoelectric properties of p-type Mg2(1+z)(Si0.3Sn0.7)1−yGay. *Intermetallics* , 32 (2013), 352.

119 Zhang, X., Liu, H., Lu, Q., and al., et. Enhanced thermoelectric performance of Mg2Si0.4Sn0.6 solid solutions by nanostructures and minute Bi-doping (2013), 063901-1.

120 Bernard-Granger, G., Guizard, C., and al., et. Spark plasma sintering of a commercially available granulated zirconia powder-II. Microstructure after sintering and ionic conductivity. *Acta. Mater.*, 56, 17 (2008), 4658-4672.

121 Bernard-Granger, G. and Guizard, C. Densification mechanism involved during spark plasma sintering of a codoped alpha-alumina material: Part I. Formal sintering analysis. *J. Mater. Res.*, 24, 01 (2009), 179-186.

122 Bernard-Granger, G., Neri, A., Navone, C., and al., et. Spark plasma sintering of a p-type Si1-xGex alloy: identification of the densification mechanism by isothermal and anisothermal methods. *J. Mater. Sci.*, 47, 10 (2012), 4313-4325.

123 Vracar, R., Bernard-Granger, G., Navone, C., and al., et. Microstructure and thermoelectrical investigations of an N-type magnesium-silicon-tin alloy. *J. Alloy. Compd.*, 598 (2014), 272-277.

124 Casper, F., Graf, T., Chadow, S., and al., et. Half-Heusler compounds: novel materials for energy and spintronic applications. *Semicond. Sci. Tech*, 27, 6 (2012), 063001.

125 Aliev, F. G., Kozyrkov, V. V., Moshchalkov, V. V., and al., et. Narrow band in the intermetallic compounds MNiSn (M=Ti, Zr, Hf). *Zeitschrift für Physik B Condensed Matter*, 80, 3 (1990), 353-357.

126 Galanakis, I., Dederichs, P. H., and Papanikolaou, N. Origin and properties of the gap in the half-ferromagneti Heusler alloys. *Phys. Rev. B*, 66 (2002), 134428.

127 Hohl, H., Ramirez, A. P., Goldmann, C., and al., et. Efficient dopants for ZtNiSn-based thermoelectric materials. *J. Phys.: Cond. Matter*, 11, 7 (1999), 1697.

128 Uher, C., Yang, J., Morelli, D. T., and Meisner, G. P. Transport properties of pure and doped MNiSn (M=Zr, Hf). *Phys. Rev. B*, 59 (1999), 8615.

129 Xia, Y., Bhattacharya, S., Ponnambalam, V., and al., et. Thermoelectric properties of semimetallic (Zr, Hf) CoSb half-Heusler phases. *J. Appl. Phys*, 88 (2000), 1952.

130 Sekimoto, T., Kurosaki, K., Muta, H., and Yamanaka, S. Thermoelec and Thermophysical Properties of TiCoSb-ZrCoSb-HfCoSb Pseudo Ternary System Prepared by Spark Plasma Sintering. *Mater. Trans.*, 47 (2006), 1445-1448.

131 Aizawa, T., Song, R., and Yamamoto, A. Solid State Synthesis of Ternary Thermoelectric Magnesium Alloy, Mg2Si1-xSnx. *Mater. Trans.* , 47, 4 (2006), 1058-1065.

132 Lee, M., Onose, Y., Tokura, Y., and Ong, N. P. Hidden constant in the anomalous Hall effect of high-purity magnet MnSi. *Phys. Rev. B* , 75 (2007), 172403.

133 Neubauer, A., Pfleiderer, C., Ritz, R., and al., et. Hall effect and magnetoresistance in MnSi. *Phys. B*, 404, 19 (2009), 3163-3166.

134 Shin, D.-K., Jang, K.-W., and Ur, S.-C. Thermoelectric Properties of Higher Manganese Silicides Prepared by Mechanical Alloying and Hot pressing. *J. Electron. Mater.*, 42 (2013), 1756.

135 Zhou, A. J., Zhao, X. B., Zhu, T. J., and al., et. Effect of ball milling on the phase constitution and microstructure of induction melted Higher Manganese Silicides and their thermoelectric properties. (Paris, France 2008), 6th European Conference on Thermoelectrics.

136 Luo, W., Li, H., Fu, F., and al., et. Improved Thermoelectric Properties of Al-Doped Higher Manganese Silicide Prepared by a Rapid Solidification Method. *J. Electr. Mater.*, 40, 5 (2011), 1233.

Abstract

N and P type Mg-Si-Sn and Mn-Si alloys have been investigated for thermoelectrical applications in the 20-600 °C temperature range. To manufacture dense sintered samples, only two steps have been used: mechanical-alloying followed by spark plasma sintering.

By optimizing the processing conditions it was possible to obtain an n-Type $Mg_2Si_{0.4}Sn_{0.6}$ material exhibiting a ZT parameter of 1.2 at 500 °C. By adding Half-Heusler nanoparticles to a $Mg_2Si_{0.4}Sn_{0.6}$ matrix, it was shown that the ZT parameter is increased to 1.4 at 500 °C. Then strong links have been established between the processing parameters, the thermoelectrical properties and the sintered microstructure (use of transmission electron microscopy).

The investigations performed on a p-type $MnSi_{1.75}$ material are only preliminary ones. Nonetheless, always by tailoring the processing conditions, it was possible to obtain a sintered material exhibiting a ZT parameter of 0.45 at 575 °C.

Keywords: thermoelectricity, Mg-Si-Sn alloys, HMS alloys, mechanical alloying, spark plasma sintering, transmission electron microscopy

Résumé

Des alliages Mg-Si-Sn et Mn-Si, de type n et p respectivement, ont été étudiés pour des applications thermoélectriques dans la gamme de température 20-600 °C. Afin de fabriquer des matériaux denses, un procédé en deux étapes a été développé. La première étape est la fabrication des poudres mères par mécano-synthèse. La deuxième étape consiste en la densification des diverses poudres par la méthode de frittage SPS.

En optimisant les conditions opératoires, un ZT de 1.2 a été obtenu à 500 °C pour un matériau de type n de composition $Mg_2Si_{0.4}Sn_{0.6}$. En incorporant de surcroit une faible fraction volumique de nanoparticules de la famille des composés Half-Heusler, il a été possible de fabriquer un matériau présentant au final un ZT de 1.4 à 500 °C. Des liens forts ont été établis entre les paramètres expérimentaux de fabrication, les propriétés thermoélectriques et la microstructure des matériaux frittés (utilisation de la microscopie électronique en transmission).

Concernant les études sur le matériau $MnSi_{1.75}$ de type p, les résultats obtenus ne sont que préliminaires. Néanmoins, en contrôlant là aussi les paramètres de fabrication, un ZT de 0.45 à 575 °C a été obtenu sur un matériau fritté.

Mots clés : Thermoélectricité, alliages Mg-Si-Sn, alliages HMS, mécano-synthèse, frittage SPS, microscopie électronique en transmission